UNIVERSITY OF CALIFORNIA, SAN DIEGO

Experiments on Nonlinear Wave-Particle Interactions

A dissertation submitted in partial satisfaction of the

requirements for the degree Doctor of Philosophy

in Physics

by

Dirk Albrecht Hartmann

Committee in charge:

Dr. C. Fred Driscoll, Chairman
Professor Thomas M. O'Neil, Co-Chairman
Professor Patrick H. Diamond
Professor Kevin B. Quest
Dr. Vitali D. Shapiro
Professor Charles W. Van Atta

1994

The dissertation of Dirk Albrecht Hartmann is approved, and it is acceptable in quality and form for publication on microfilm:

Kenneth Kreutz-Delgado

Vitali Shapiro

Charles W. Van Atta

Patrick H. Diamond

Charles F. Driscoll
Chairman

Thomas O'Neil
Co-Chairman

University of California, San Diego

1994

Für meine Eltern.

Contents

List of Figures

Acknowledgements

I am indebted to my advisors, the late Professor John Malmberg, Dr. Fred Driscoll and Professor Thomas O'Neil. Only their guidance, continued interest and encouragement, and their generosity with their time made the completion of this dissertation possible. With their example they taught me how to pose and answer scientific questions. The profundity of their different, but complementary approaches set standards that I will strive to meet. I thank Dr. Vitali Shapiro for his mode-coupling calculation and Professor Patrick Diamond for suggesting tri-spectral analysis as a means of investigating mode-coupling. The time that the other members of my committee, Professor Kevin Quest and Professor Charles Van Atta, spent reviewing my dissertation, is thankfully acknowledged.

I greatly appreciate the help of Dr. Stan Tsunoda who initially taught me how to operate the traveling wave tube and whose suggestions and detailed knowledge of the experiment continued to be very useful. Dr. Travis Mitchell, Dr. Xiao-Pei Huang and Mitch Brittnacher were supportive and good friends.

Even though the traveling wave tube always was the "other" experiment in the nonneutral plasma group at UCSD, I received much help from my co-workers. I owe special gratitude to Dr. Francois Anderegg, Dr. Bret Beck, Professor Dan Dubin, Dr. Kevin Fine, Dr. John Moody and Dr. Eli Sarid. JoAnn Christina and Robert Bongard provided secretarial and technical help with amiable reliability and promptness.

The friendship with many people outside the department has often sustained me over the years. In particular, I thank Heike Behl, Sarah Birdsall, Rocio Carrera, Rev. John Huber, Dr. Peter Leopold, Ken'ichi Miura, Dr. Hartmut Pleines, Dr. Manfred Schabes, Dr. Mia Unson and Juliana von Hacht.

Finally, my deepest thanks go to my parents who encouraged me throughout all these years, unfaltering in their support and unswerving in their faith.

Financial support was provided by NSF grants PHY83-06077, PHY87-06358 and PHY91-20240.

Vita, Publications and Fields of Study

Vita

16 March 1963	Born, Weinheim/Bergstraße, Germany
1982-1985	Universität Stuttgart
1985-1987	M.S., University of California, San Diego
1985-1994	Ph.D., University of California, San Diego

Publications

1. D. A. Hartmann, J. H. Malmberg. Phase Measurements of Sidebands. *Bull. Am. Phys. Soc.*, 35:1930 (1990).
2. D. A. Hartmann. Experiments in the Quasilinear Regime. *Bull. Am. Phys. Soc.*, 36:2271 (1991).
3. D. A. Hartmann, J. H. Malmberg. Messungen der Modenkopplung im quasilinearen Bereich. *Verhandl. DPG (VI)*, 27:1376 (1992).
4. D. A. Hartmann, J. H. Malmberg. Measurement of Sideband Phase Relationship. *Bull. Am. Phys. Soc.*, 37:1360 (1992).
5. D. A. Hartmann, J. H. Malmberg. Messung der Phasenbeziehung zwischen Seitenbändern. *Verhandl. DPG (VI)*, 28:120 (1993).
6. D. A. Hartmann, T. M. O'Neil, V. D. Shapiro. Detailed Measurements of the Bump-On-Tail Instability. *Bull. Am. Phys. Soc.*, 38:1909 (1993).

Fields of Study

Major Field: Physics

Studies in Plasma Physics
Professors John H. Malmberg, Thomas M. O'Neil, Ron E. Waltz,
Marshall N. Rosenbluth, Patrick H. Diamond, and Daniel H. E. Dubin

Studies in Mechanics
Professor Thomas M. O'Neil

Studies in Electromagnetism
Professor Donald R. Fredkin

Studies in Quantum Mechanics
Professors Julius Kuti

Studies in Statistical Mechanics
Professor Andrei E. Ruckenstein

Studies in Mathematical Physics
Professor Frank B. Thiess

Studies in Differential Geometry and Exterior Calculus
Professor Theodore T. Frankel

Abstract of the Dissertation

Experiments on Nonlinear Wave-Particle Interactions

by

Dirk Albrecht Hartmann

Doctor of Philosophy in Physics

University of California, San Diego, 1994

Dr. C. Fred Driscoll, Chairman

Professor Thomas M. O'Neil, Co-Chairman

Experiments on nonlinear wave-particle interactions using a traveling wave tube (TWT) are described. There, one or more waves modify the motions of energetic beam particles, and these beam perturbations affect the wave evolution. At large amplitudes, mode-coupling is observed and forms the focus of this study. The wave-particle interactions are very similar to those in beam-plasma systems. However, the slow wave structure of the TWT stays linear for all wave amplitudes reached and does not introduce noise. The precise wave evolution can thus be obtained by launching a specified waveform, allowing it to interact with the beam, and analyzing the received waveform. Two cases are considered.

To study the "weak warm beam instability", a broad spectrum of waves on a warm beam is launched. At saturation, significant mode-coupling results in wave correlations smaller than 0.5 with their launch values. Experimentally each wave is separated into two components: one component proportional to the launch amplitude and the other due to mode-coupling. The mode-coupling component growth rate is

about three times larger than the ensemble-averaged wave growth rate, which is in agreement with a four-wave coupling model. Strongest coupling occurs between waves whose wavelengths match within about a turbulent trapping length. In the linear regime, the measured ensemble-averaged wave growth rates and beam velocity diffusion rates agree reasonably with quasilinear and resonance-broadening theory; in the nonlinear regime up to saturation, the discrepancies are larger.

To study the "sideband instability", both a large amplitude wave that traps a cold electron beam and two small amplitude sidebands are launched. For a range of sideband frequencies, mode-coupling results in phase-locking between the sidebands, characterized by the "modulational phase". These two growing sidebands can be interpreted as a single normal mode of the Kruer, Dawson, Sudan macroparticle model. The measured sideband growth rates, wavenumber shifts, modulational phase and amplitude ratio qualitatively agree with the model. However, quantitative agreement is found only with computer simulations that follow the full phase-space distribution of the particles. Therefore the discrepancies are due to the simplicity of the model.

Chapter 1

Overview and Summary

This dissertation describes experiments on nonlinear wave-particle interactions on a traveling wave tube (TWT). In these interactions, one or more waves modify the motions of energetic beam particles, and these perturbations in the beam then affect the evolution of the waves. At large amplitudes, the waves become coupled through the nonlinear motion of the beam particles. These wave-particle interactions are very similar to those that occur in beam-plasma systems. The TWT experiments focus on the characteristics and effects of these mode-couplings for two cases: the "weak warm beam instability" and the "sideband instability".

Traveling Wave Tube

A traveling wave tube (TWT) [48] is a device where waves propagate along a helical slow wave structure and interact with an electron beam streaming along the axis. For small beam currents, the equations describing the dynamics are identical to the equations of a one-dimensional beam interacting with waves on a plasma, where the plasma is approximated as a dielectric [16, 62]. For larger beam currents, expressions for the beam space-charge need to be included [62].

The TWT offers advantages over beam-plasma experiments for studying wave-beam interactions and comparing them to theory. Since the slow wave structure

is inherently linear, wave-beam interactions are the only sources of nonlinearities in a TWT. In beam-plasma experiments, there may be additional nonlinearities that complicate the interpretation of the results. In our TWT the background noise level is smaller than the wave saturation level by about 55 dB. Therefore we can launch waves at larger than noise level, so that their known amplitudes and phases completely determine the initial condition and the subsequent evolution of the wave-beam interaction. We study the spatial evolution of the instability for this particular initial condition by detecting the wave signal at different positions in the interaction region. By launching different waveforms in successive experiments we may perform controlled ensemble-averages.

We launch these waves as a waveform of period T generated with an arbitrary waveform generator. Amplitudes and phases of the Fourier modes of this waveform can be chosen arbitrarily. For example, we can choose the amplitudes to be a smooth function of frequency and the phases to be random between 0 and 2π in order to create broadband "noise"; or we can choose the spectrum to consist of a carrier and two sidebands to create a frequency or amplitude modulated wave. In chapter 2 we describe the TWT and the experimental setup in detail.

Wave-Particle Interaction

When an electron beam is injected into a plasma, electrostatic waves can grow at the expense of the kinetic energy of the beam. Strong interaction between a beam electron and a wave occurs if both travel at the same speed, i.e. if $\omega = k_\omega v$, where v is the velocity of the electron and ω is the angular frequency and k_ω the wavenumber of the wave. Depending on the phase of the wave electric field in the electron frame, the beam electron is accelerated or decelerated. The resonant exchange of energy leads to exponential wave growth (at a rate k_ω^i) until the electric field amplitude is large

enough to react back on the beam, turning the instability off within approximately another growth length, $k_\omega^{i\,-1}$. Depending on the width of the spectrum at the onset of the nonlinear region, two different saturation mechanisms are possible.

Weak Warm Beam Instability

If the electron beam is warm [46], a wide range of waves with phase velocities on the positive slope of the beam distribution becomes unstable and grows at the expense of the beam kinetic energy. Then at the onset of the nonlinear region, the beam electrons interact with waves over a wide range of phase velocities and any given beam electron sees the phase of the electric field change sign many times within one growth length. One expects and finds velocity diffusion of the beam. The diffusion decreases the slope of the velocity distribution, thereby turning the instability off. The condition that the electric field changes sign many times within one growth length is given by the requirement that the autocorrelation length[1], l_{ac}, is much shorter than the growth length,

$$l_{ac} \ll k_i^{-1}. \tag{1.1}$$

In the TWT experiment we observe strong mode-coupling, to the extent that adjacent modes can evolve very differently from one another. We describe the properties of the mode-coupling statistically and find that at saturation the waves have a correlation of less than 0.5 with their launch values. Further, the kurtosis of the waveform changes from near zero (corresponding to a Gaussian distribution) to about -0.6 at saturation, which can be interpreted as developing a frequency-modulated waveform. We also investigate the mode-coupling with "test-modes". A Fourier mode is considered a test-mode if changing its initial amplitude by 100% has

[1]The autocorrelation length is approximately the distance over which the phases of two waves of the spectrum seen in the frame of a beam electron change by π relative to one another.

negligible effect on the evolution of all the other modes. We decompose the received test-mode into a component T that depends linearly on the launched (*transmitted*) test mode and a second component S that accounts for the power *scattered* from all other modes. The properties of the scattered and the transmitted component agree with the predictions of a a four-wave coupling model [53] until close to saturation: the scatter components have growth rates about three times larger than the average wave growth rates and the strongest coupling between waves occurs if their wave numbers match within the inverse turbulent trapping length.

We measure the ensemble-averaged growth rates of the waves and compare them to "quasilinear" (QL) theory [18, 67] and Dupree's "resonance-broadened" (RB) version [20]. In the linear regime, we find good agreement with the predictions of quasilinear theory and resonance-broadening theory. In the nonlinear regime the velocity distribution changes. For low phase velocities the measured growth rates approximately agree with both theoretical predictions; at phase velocities corresponding to the center of the beam, the measured growth rates agree better with RB theory, but are still larger. The growth rate measurements have large errors due to incomplete phase-mixing and space-charge effects at high phase velocities and inhomogeneities of the slow wave structure at low phase velocities.

We also measure the diffusion of the beam. For cold test beams, we find good agreement between the measured and calculated diffusion rates. For the self-consistent evolution of the warm beam, the agreement is only qualitative, with increased diffusion at both velocity ends of the beam distribution. We describe all measurements in chapter 3.

Sideband Instability

If the electron beam is cold [46], the bandwidth of unstable waves is small and the spectrum of growing waves narrows over a few growth lengths. Then at the onset of the nonlinear regime, the beam electrons interact with an essentially monochromatic wave. This wave saturates by trapping a fraction of the beam electrons, and further net energy transfer from the beam to the wave is impossible. Some energy, however, can be traded back and forth between the wave and the trapped electrons bouncing in the potential of the wave. In order to observe such trapping oscillations it is necessary that the autocorrelation length, l_{ac}, is much longer than the growth length, k_i^{-1},

$$l_{ac} \ll k_i^{-1}. \tag{1.2}$$

In chapter 3 we investigate the "sideband instability" [69] that can result from such a trapped electron state. In this instability nearby waves can become unstable if their frequencies, ω, Doppler-shifted into the frame of the trapped electrons, approximately equal the bounce frequency, ω_B, of the electrons:

$$\omega - \frac{k}{k_T}\omega_T \approx \pm\omega_B \tag{1.3}$$

Here k is the wavenumber of a sideband, and k_T and w_T are the wavenumber and frequency of the trapping wave. Two sidebands, one with higher, the other with lower phase velocity than the trapping wave can become unstable.

Our study focuses on the sideband instability in the limit of small sideband amplitudes. We consider two cases: with and without residual trapping oscillations of the trapping wave amplitude. We find that the initial evolution of these sidebands depends on their initial phases and amplitudes relative to one another. However, a particular phase and amplitude relationship between the sidebands arises that is independent of their initial values. This occurs after some transition period of about

one trapping length, v/ω_B, but only for a range of sideband frequencies. We measure the sideband growth rates, wavenumber shifts, amplitude ratio and phase relationship for different amplitudes of the trapping wave and in different regimes of the helix dispersion. We compare our results with predictions of the macro-particle model by Kruer, Dawson and Sudan [37], modified by Morales [43]. This theory approximates the trapped particle distribution with a macro-particle and predicts unstable "normal modes" formed by a linear combination of upper and lower sideband. Even in regions where the group velocity of the helix dispersion is approximately constant, agreement between the sideband measurements and the model predictions is only qualitative. In regions where the group velocity changes significantly, no coupling is found, in contrast to the macro-particle model. We find agreement between our measurements and computer simulations that follow the full motions of beam electrons. Therefore we conclude that the discrepancies are due to the simplicity of the macro-particle model.

Chapter 2

The Traveling Wave Tube

This chapter describes the experimental apparatus and reviews the linear theories for cold and warm electron beams interacting with the waves on the slow wave structure. It then describes the measurements of the linear parameters used for characterizing the waves on the slow wave structure, the electron beam and the interaction between the waves and electron beam. In the last section we show that the measured wavenumbers and growth rates of the growing waves agree well with the calculated values for both the cold and the warm beam. More details of the apparatus and its parameters can be found in [16] and [62] and in appendix A.

2.1 Apparatus

Figure 2.1 shows a schematic diagram of the apparatus: a custom-made traveling wave tube (TWT) [48]. It consists of three main elements: a slow wave structure formed by a helix with axially movable antennae, an electron gun with a velocity spreader, and an electron beam analyzer. The electron gun emits a beam with a variable spread of axial velocities along the axis of the slow wave structure. Waves are launched with an antenna at the end of the slow wave structure closest to the electron gun, travel along the slow wave structure, and continuously interact with the electron beam. They are detected with a movable probe and the changes

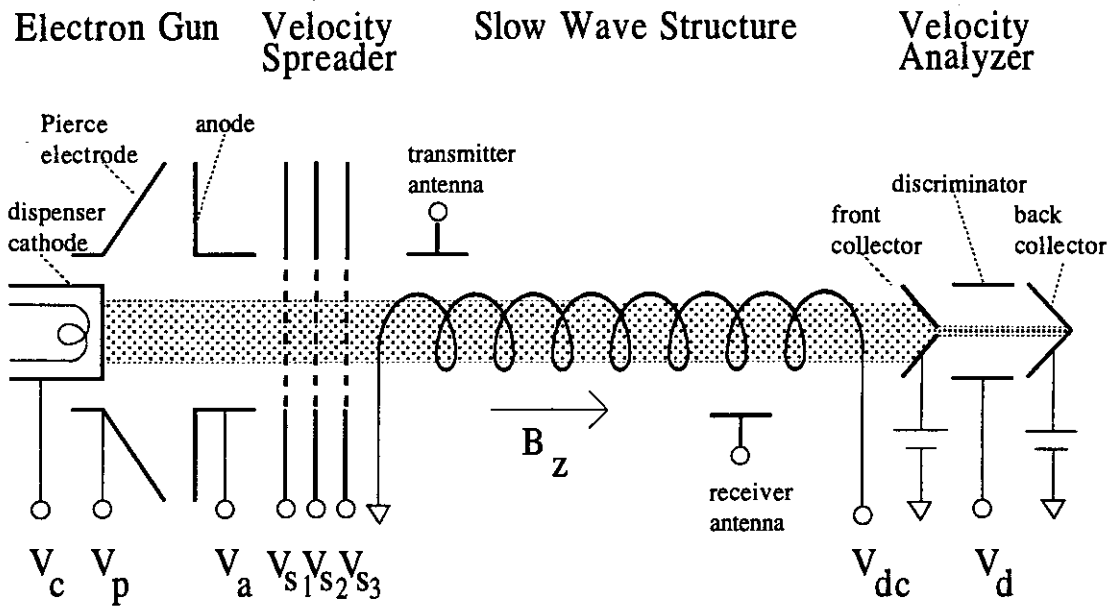

Figure 2.1: Schematic of the traveling wave tube.

of the electron beam distribution are measured with the velocity analyzer.

The slow wave structure consists of a 2.7 m long wire helix composed of 0.51 mm diameter Beryllium-Copper wire glued to four supporting alumina rods outside the helix. The pitch of the helix is 0.79 mm and its outside diameter is 22.1 mm. The launched waves travel along the helix wire with the speed of light; their phase velocities along the axis of the helix are smaller by approximately the ratio of the pitch to the helix circumference of 0.011 and between 3.5×10^6 m/s and 5.5×10^6 m/s. At both ends of the helix, resistive terminations reduce the reflections of the waves. The maximal VSWR is 1.26 due to residual end reflections and irregularities of the helix. Since the backward-traveling waves are far from resonance with the electrons, their effect on the instabilities is neglected. The usable length of the helix is 2.35 m. The whole assembly is fitted in a glass vacuum tube which in turn is placed along the axis of a lengthwise slotted cylindrical waveguide of 76 mm inner diameter. In the cylinder but outside the glass tube, four axially movable capacitative antennae

can excite or detect helix modes in the frequency range from 5 to 95 MHz. Only the helix modes are launched, since waveguide modes can only propagate above 3.0 GHz. These helix modes have electric field components along the axis of the helix. Their radial structure is shown by Dimonte and Malmberg [16]. The helix is with about 20 e-folding lengths of linear wave growth much longer than commercially available TWTs, thus allowing measurements of the evolution of launched waves well into the nonlinear regime.

A Pierce-type electron gun is mounted on the front end of the helix. The indirectly heated dispenser cathode is biased at the cathode potential V_c. The Pierce electrode is biased at a slightly more negative potential, V_p, to obtain an electron beam with constant density across its radius. Once every 60th of a second an 80 μs beam is obtained by pulsing the anode from a retarding voltage more negative then V_c to a voltage less negative. The voltage difference between the cathode and the anode regulates the beam current. The beam is pulsed so that ions created from the residual background gas do not accumulate and eventually neutralize the beam. Beam currents, I_b, up to 250 μA and maximal cathode voltages, V_c, up to 300 V can be set independently. The resulting beam velocities cover the range of phase velocities of the helix modes.

A velocity spreader between the electron gun and the helix can widen the axial velocity distribution of the beam. It consists of three wire grids that are biased independently to the voltages V_{s1}, V_{s2} and V_{s3}. Typically the center grid V_{s2} is biased to +1800 V and the neighboring grids are grounded, i.e. $V_{s1} = V_{s3} = 0$ V. The electrons non-adiabatically scatter some of their axial velocity into perpendicular velocity due to the strong electric field close to the wires of the central grid. Only the axial velocity distribution is relevant for the ensuing wave-particle interaction since the cyclotron frequency of the electrons is with 1.18 GHz much higher than

other frequencies pertaining to the experiment. Thus a one-dimensional description of the wave-beam interaction is sufficient.

At the back end of the helix, most of the electrons are collected on the biased (+230V) front collector of a velocity analyzer. A small fraction (0.5%) of the electrons passes through a hole in the center of the front collector, passes through a discriminator ring, and is collected at the biased (+230V) back collector. By applying a negative voltage to the discriminator and measuring the back collector current versus the discriminator voltage, V_d, the integrated time-averaged axial velocity distribution is measured, from which the velocity distribution function can be determined by analog or computational differentiation. The rf part of the velocity distribution function cannot be measured, because the electrons loose their phase relationship with the waves in the drift region between the end of the helix and the analyzer.

The electron gun, velocity spreader, helix and velocity analyzer are under vacuum. The pump pressure at the ion-pump is $7. \times 10^{-8}$ torr; the pressure at the center of the tube is approximately 10^{-6} torr. The whole apparatus is immersed in a strong axial magnetic field of B_z=0.042 T. This field confines the electrons radially to the center of the tube. Two correction coils provide perpendicular magnetic fields B_x and B_y to control the tilt of the electron beam with respect to the axis of the helix.

2.2 Operation and Measurements

Waves of various frequencies are launched at the end of the wave-beam interaction region closest to the electron gun and their spatial evolution is measured as they propagate along the helix and interact with the electron beam. In a TWT the background noise level is much smaller than the wave saturation level ($\approx$ 55

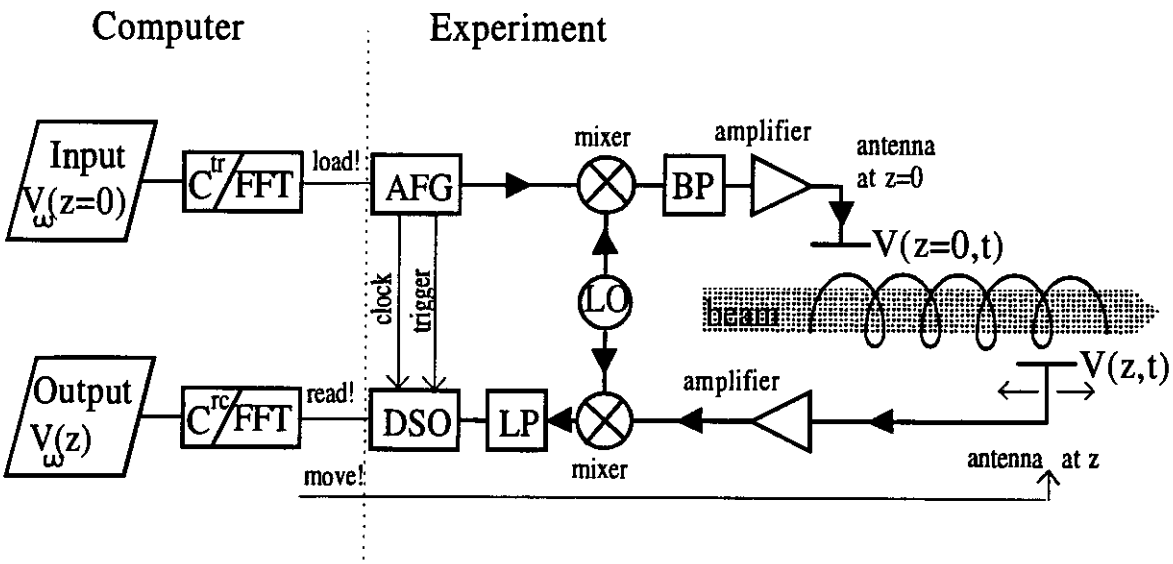

Figure 2.2: Schematic of the experimental setup.

dB). Therefore we can launch waves at larger than noise levels and completely determine the initial condition of the wave-beam interaction and are still left with a large dynamic range extending from the linear into the strongly nonlinear regime. This is in contrast to typical beam plasma experiments where the noise level (due to ions, for example) is large and not much smaller than the saturation level. We create and repeatedly transmit the launched waveform with an arbitrary function generator. This allows us to study the spatial wave-beam interaction for precisely and completely defined initial conditions, in analogy to the temporal evolution of the interaction often investigated in computer simulations and theories.

Figure 2.2 shows the schematic diagram of the experimental setup to measure the spatial evolution of the waves. It has three main components: a transmitter section consisting of an arbitrary function generator (AFG) and transmitter circuit, a receiver section consisting of the receiver circuit and a digital sampling oscilloscope (DSO), and a computer where the launched waveform is defined and the received waveform is analyzed and stored.

The launched waveforms are designed in the computer. The number of wave-

points, N, that constitute the waveform is a power of 2 to be able to use most effective Fast Fourier Transform (FFT) techniques. For sideband experiments $N = 256$, i.e. the waveform has $N/2 = 128$ possible Fourier modes; for most weak warm beam experiments $N = 4096$, i.e. the waveform has 2048 Fourier modes. In order to create a waveform $V(z = 0, t)$ that is to be launched at position $z = 0$, we specify the values of the complex amplitudes (amplitudes and phases) $V_\omega(z = 0)$ of all the Fourier modes. In the following we will use the convention that $\mid V_\omega(z = 0) \mid$ is the amplitude of the wave potential at frequency $\omega/2\pi$.

The spectrum is modified for the combined frequency-dependent coupling coefficients, C_ω^{tr}, of the transmitter circuit and the transmitter antenna. We determine the coupling coefficients of the transmitter circuit by measuring the response of the circuit to a short δ-function pulse at its input. These coefficients are complex because of the phase shifts caused by the rf-filters in the transmitter circuit. The coupling coefficients of the transmitter antenna are determined from a standard three-probe measurement [40]. The combined accuracy of this calibration is about $\pi/16$ in phase and 3 dB in amplitude. The waveform created by the FFT of the modified spectrum is then scaled and discretized to fully utilize the 8 bit vertical resolution of the AFG.

The discretized version of the waveform is loaded into the memory of the AFG, then sent to an internal digital-to-analog converter at a rate of $f_{\text{clock}} = 120$ MHz. Thus for sideband experiments the waveform is $N/f_{\text{clock}} = 2.1\mu$s long and for weak warm-beam experiments the waveform is 34.1μs long. The finite bit resolution and nonlinearities associated with slew-rates create unwanted Fourier modes in the spectrum. They are approximately 45 dB below the amplitude of the largest mode. The highest frequency that can be generated is 60 MHz. In order to launch waves with frequencies in the 30 - 80 MHz region of interest, the output signal of the AFG is homodyned in a rf mixer with the $f_{\text{hom}} = 86$ MHz signal of a local oscillator (LO).

A bandpass filter (BP) is used to selects the frequencies lower than the homodyne frequency. The signal is then amplified and launched from the transmitter antenna at the beginning of the interaction region at $z = 0$.

The wave signal is detected with a computer-positioned receiver antenna, amplified and again homodyned with the same LO. The signal is lowpass-limited (LP) to frequencies smaller than the Nyquist frequency, $f_{\text{clock}}/2$, then sampled by the DSO. The DSO has a vertical resolution of 8 bits, its sampling clock is locked to the clock of the AFG. The detected waveform is read and stored by the computer.

A FFT of the waveform yields the complex amplitudes of the spectrum. Because the clocks of the AFG and the DSO are phase-locked and the same LO is used for the transmitter and the receiver circuit, the Fourier modes of the received waveform are directly related to the corresponding Fourier modes of the transmitted waveform. The received spectrum is modified for the measured combined coupling coefficients, C_ω^{rc}, of the receiver circuit and the receiver antenna. The output of the computer, $V_\omega(z)$, are the measured complex Fourier amplitudes of the wave potentials in the traveling wave tube at position z, with an accuracy of about 3 dB in amplitude and $\pi/16$ in phase.

The timing sequence of the experiments is such that the output of the waveform is started 10 μs before the beam pulse, and then repeated continuously throughout the duration of the beam. This is necessary because the measurement of the velocity distribution capacitively averages over $20\mu s$. About $20\mu s$ into the beam pulse, the beam has stabilized and wave transients have died away. $40\mu s$ into the beam pulse, the DSO starts reading in the number of wavepoints of the waveform transmitted by the AFG. We increase the signal-to-noise ratio in the receiver circuit to about 55 dB by averaging the detected waveform over 100 beam pulses. This also increases the bit resolution of the DSO by about 1 bit due to dithering.

In our experiments on the sideband instability we apply an additional dc electric field to the beam electrons. This is done by grounding the helix on the gun side and applying a voltage to it on the velocity analyzer end. Since the heat dissipation in the helix can lead to deterioration, the voltage is pulsed on only for the duration of the beam.

The whole process is repeated at different positions of the receiver antenna. The spatial localability of the antenna is 2 mm over the length of the helix. The digitized waveform and the antenna position are stored in the computer. By measuring the spectrum densely in space (every 5 mm) we can obtain a complete picture of the evolution of all the mode amplitudes $V_\omega(z)$ for the chosen initial waveform.

In most experiments, we simulate the effects of a directional coupler in order to remove the backward wave component (which causes spatial oscillations of the modes at half their wavelengths) from the obtained data. This is done by replacing the complex Fourier amplitude of each mode $V_\omega(z)$ at each position by a weighted average of its Fourier amplitudes at a quarter wavelength (about 15 mm) to both sides of the antenna position. In simulations with fake data we find that for typically encountered growth rates the calculated amplitude agrees with the actual amplitude within .5 dB if the spectrum has been measured at at least 12 positions per wavelength. This requirement is fulfilled for all the wave frequencies of interest by measuring the waveforms every 5 mm.

We calculate the local real and imaginary part of the wavenumber $k_\omega(z) \equiv k_\omega^r(z) - ik_\omega^i(z)$ of each mode from the spatial evolution of its complex wave potential $V_\omega(z)$. As was mentioned above, the waveform is read in at the same time with respect to the launching of the waveform at all probe positions z. Therefore the measured complex amplitude of one Fourier mode $V_\omega(z)$ has a spatial dependence

given by:

$$V_\omega(z) \equiv \mid V_\omega(z) \mid e^{i\phi_\omega(z)}, \tag{2.1}$$

$$\text{with} \mid V_\omega(z) \mid = \mid V_\omega(z=0) \mid e^{\int_0^z dz' k_\omega^i(z')}, \tag{2.2}$$

$$\phi_\omega(z) = \int_0^z dz' k_\omega^r(z') + \phi_\omega^0. \tag{2.3}$$

ϕ_ω^0 is the phase at $z = 0$. We measure the "local" growth rate $k_\omega^i(z)$ by fitting a straight line to the spatial evolution of the logarithm of the magnitude $\mid V_\omega(z) \mid$ of the wave potential in some region around z. We measure the "local" wavenumber $k_\omega^r(z)$ by fitting a straight line to the phase of the Fourier mode, $\phi_\omega(z)$, in some region around z. In both cases, the fit region is typically 0.25 m long, which corresponds to 2-5 wavelengths. Often we will be interested in the "phase shift", $\delta\phi_\omega(z)$. This is the phase change of the Fourier mode amplitude that is caused by the interaction of the wave with the electron beam. We define it as:

$$\delta\phi_\omega(z) \equiv \phi_\omega(z) - \int_0^z dz' k_\omega^{0r}(z') \tag{2.4}$$

$k_\omega^{0r}(z)$ is the local wavenumber of the beamless helix. We will also be interested in the "wavenumber shift", $\delta k_\omega^r(z)$, which is obtained by taken the slope of a straight line fit to the phase shift. It is defined as

$$\delta k_\omega^r(z) \equiv k_\omega^r(z) - k_\omega^{0r}(z) \tag{2.5}$$

Equation (2.5) anticipates that the wavenumber of waves on the helix can be dependent on z. As shown in appendix A we indeed find this to be the case for our helix. There we show that in the second half of the helix, the wavenumber decreases by about 1% and the damping rate increases by about 50% compared to the first half.

2.3 Linear Theory

The linear theory of the TWT is given for the two cases of a weak monoenergetic electron beam and a weak warm electron beam interacting with a single

wave on the slow wave structure. We follow Pierce [48] and Tsunoda [62] in their treatment of the cold beam and Tsunoda [64] in his treatment of the warm beam.

2.3.1 Cold Electron Beam

The linear theory of the interaction of a mono-energetic electron beam with a wave on the slow wave structure assumes that the changes in electron velocity $v(z,t) - u_0$ and in beam charge density $\rho(z,t) - \rho_0$ are small compared to the initial velocity $u_0 = \sqrt{2eV_0/m}$ and initial charge density ρ_0.

An electron experiences the electric field $E^h(z,t)$ of the helix waves and the smaller space-charge ("Coulomb") field $E^{sc}(z,t)$ created by all the other electrons of the beam. Because of the strong guiding magnetic field, the axial motion is decoupled from the perpendicular motion and a one-dimensional description is possible. Newton's equation for the acceleration along the axis of the slow wave structure gives

$$\frac{dv}{dt} = -\frac{e}{m}(E^h(z,t) + E^{sc}(z,t)), \tag{2.6}$$

where $-e$ is the electron charge and m is the electron mass. Here we have assumed azimuthal symmetry. We neglect the radial dependence because both fields are constant to within 15% across the beam radius (see [16] for plots of the electric fields of the helix modes).

The evolution of the helix waves, $V^h(z,t) = \frac{1}{2}\{V^h_\omega e^{ik_\omega z - i\omega t} + c.c.\}$, is found by representing the slow wave structure with a one-dimensional transmission line [7]:

$$\frac{d^2V^h_\omega}{dz^2} + (k^0_\omega)^2 V_\omega = \omega Z_\omega k^0_\omega A_b \rho_\omega(r=0,z) \tag{2.7}$$

With the helix electric field given by

$$E^h(z,t) = -\frac{\partial V^h(z,t)}{\partial z} \tag{2.8}$$

we obtain

$$-k^2_\omega\ \epsilon_0\ \epsilon^h(\omega,k_\omega)V^h_\omega = -\rho_\omega(r=0), \tag{2.9}$$

where we have lumped all quantities pertaining to the helix into a "helix dielectric" defined by:

$$\epsilon^h(\omega, k_\omega) \equiv \frac{k_\omega^{0\,2} - k_\omega^2}{\epsilon_0 \omega k_\omega^0 k_\omega^2 Z_\omega A_b}. \tag{2.10}$$

Z_ω is the interaction impedance that describes the coupling of the beam modes to the space-charge modes. In lossy structures it has a small imaginary component, which can be neglected [48]. Its real part is given by

$$R_\omega = Real\{Z_\omega\} \equiv \frac{\langle \mid E_\omega^h \mid^2 \rangle_{A_b}}{2 k_\omega^{0r\,2} P_\omega}, \tag{2.11}$$

where $\langle \mid E_\omega^h \mid^2 \rangle_{A_b}$ is the square of the axial electric field averaged over the area of the beam, $A_b = \pi r_b^2$; P_ω is the total wave power, both in the absence of the beam. R_ω decreases with frequency because the helix modes become increasingly peaked at the helix [16].

The space-charge electric field can be calculated from Poisson's equation. With $E^{sc}(r,z,t) = -\frac{\partial V^{sc}(r,z,t)}{\partial z} = -\frac{\partial}{\partial z}\frac{1}{2}\{V_\omega^{sc}(r)e^{ik_\omega z - i\omega t} + c.c.\}$ we obtain

$$\epsilon_0 \left(\frac{\partial^2 V^{sc}(r)_\omega}{\partial r^2} + \frac{1}{r}\frac{\partial V_\omega^{sc}(r)}{\partial r} - k_\omega^2 V_\omega^{sc}(r)\right) = -\rho_\omega(r) \tag{2.12}$$

Following [6] we model the slow wave structure as a conducting cylinder of the same radius a as the helix. Since both the space-charge field and the helix field are almost constant over the beam cross-section, also the charge density ρ_w is approximately independent of radius and we find:

$$-k_\omega^2 \epsilon_0 V_\omega^{sc}(r=0) = -P_q(k_\omega r_b)\rho_\omega(r=0) \tag{2.13}$$

$$\text{with } P_q(k_w r_b) = 1 - k_\omega r_b K_1(k_\omega r_b)[1 - \frac{K_0(k_\omega a)I_1(k_\omega r_b)}{I_0(k_\omega a)K_1(k_\omega r_b)}]. \tag{2.14}$$

P_q is called the "plasma frequency reduction factor"; in our experiments it is smaller than 0.1. The expression for P_q is approximate because of our neglect of the radial dependence of the beam charge density, but is independent from the beam dynamics and is therefore applicable to cold and warm beams.

For the linear theory of the cold beam we obtain the beam dynamics from linearizing the continuity equation for the charge density $\rho(r = 0, z, t)$.

$$-i\omega\rho_\omega + ik_\omega u_0\rho_\omega + ik_\omega(v - u_0)\rho_0 = 0 \tag{2.15}$$

Combining equations (2.6) to (2.15) we then obtain the dispersion relation for waves on the helix for a cold beam.

$$(\omega - k_\omega u_0)^2\epsilon^h(w, k_\omega) = \omega_p^2[1 + P_q(k_\omega^r r_b)\epsilon^h(\omega, k_\omega)] \tag{2.16}$$

where ω_p is the beam plasma frequency, given by:

$$w_p^2 = \frac{-e\rho_0}{\epsilon_0 m} \tag{2.17}$$

2.3.2 Warm Electron Beam

The linear theory of the interaction of a monochromatic wave with a warm electron beam on a slow wave structure is obtained by linearizing the Vlasov equation for the perturbations of the axial velocity distribution function rather than the continuity equation as in the cold beam case.

The evolution of the electron beam is given by the one-dimensional Vlasov equation for the electron velocity distribution function, $f(v, z, t)$, where the electric field is again the sum of the helix wave field $E^h(z, t)$ and the space-charge field $E^{sc}(z, t)$:

$$\frac{\partial f}{\partial t} + v\frac{\partial f}{\partial z} + \frac{-e}{m}(E^h(z, t) + E^{sc}(z, t))\frac{\partial f}{\partial v} = 0. \tag{2.18}$$

With the convention $f(v, z, t) = f_0(v) + \frac{1}{2}(f_\omega(v)e^{ik_\omega z - i\omega t} + c.c)$ we obtain for the linearized version:

$$(-i\omega + ivk_\omega)f_\omega + \frac{-e}{m}(E_\omega^h + E_\omega^{sc})\frac{\partial f_0}{\partial v} = 0. \tag{2.19}$$

We can still use equation (2.9) for the generation of the helix electric field and equation (2.13) for the generation of the space-charge field with the charge density

given by

$$\rho_\omega = \frac{-en_0}{A_b}\int_0^\infty dv f_\omega(v), \tag{2.20}$$

where n_0 is the axial electron density.

Combining equations (2.9), (2.13) and (2.19) we find for the dispersion relation for a warm beam:

$$\epsilon^h(\omega,k_\omega) = \omega_p^2[1+H_q(\omega)]\frac{-1}{k^2}\int_{0\mathcal{L}}^\infty dv\frac{\partial f_0(v)/\partial v}{v-\omega/k_\omega} \tag{2.21}$$

$$\text{where} H_q(\omega) \equiv \epsilon^h(\omega,k_\omega)P_q(k_\omega r_b) \tag{2.22}$$

The term $H_q(\omega)$ is the space-charge contribution. Except near regions where $\partial f_0/\partial v$ is large this term can be neglected as will be shown in section 2.5.2. The velocity integration is done along the Landau-contour $\mathcal{L}$. For a cold beam this expression reduces to the linear dispersion relation (2.16).

Neglecting space-charge and assuming a very weak warm beam, i.e. for almost vanishing growth rates $k_\omega^i/k_\omega^r \ll 1$, one finds the familiar Landau solutions:

$$k_\omega^r = k_\omega^{0r} \tag{2.23}$$

$$k_\omega^i = -\pi\frac{\omega_p^2}{k_\omega^{0r2}}\frac{1}{\frac{\partial\epsilon^{h\prime}}{\partial k}|_{k_\omega^{0r}}}\frac{\partial f_0(v)}{\partial v}|_{v=\frac{\omega}{k_\omega^{0r}}} + \frac{\epsilon^{h\prime\prime}(\omega,k_\omega^{0r})}{\frac{\partial\epsilon^{h\prime}}{\partial k}|_{k_\omega^{0r}}} \tag{2.24}$$

$$= \frac{\pi}{2}\omega_p^2\epsilon_0\omega R_\omega A_b\frac{\partial f_0(v)}{\partial v}|_{v=\frac{\omega}{k_\omega^{0r}}} + k_\omega^{0i} \tag{2.25}$$

2.4 Linear Properties

In this section we describe the measurements of the parameters that characterize the helix waves and the electron beam. This is a review of the techniques presented in detail in [16] and [62].

Figure 2.3 shows a plot of the measured and theoretical helix dispersion. It has a shape similar to Gould-Trivelpiece modes of electrostatic plasma waves confined in a conducting cylinder [61]. The measured wavenumbers are determined

as described in section 2.2. They are the average values over the first half of the helix. Appendix A discusses the local wavenumbers and damping rates. The theoretical dispersion is calculated assuming the Pierce sheath helix model [48] and assuming that the shell-like region of the alumina rods can be modeled by an effective dielectric constant [62]. The measurements are within 0.25% of the corresponding theoretical values. In addition, the dashed line in figure 2.3 shows the calculated phase velocity $v_\omega^{ph} \equiv \omega/k_\omega^{0r}$ of a wave of frequency $\omega/2\pi$ in the absence of the beam; the dotted line shows the calculated group velocity $v_\omega^{gr} \equiv d\omega/dk_\omega^{0r}$. In chapter 4 the measured growth rates and wavenumber shifts will often be shown versus phase velocity rather than versus frequency or wavenumber.

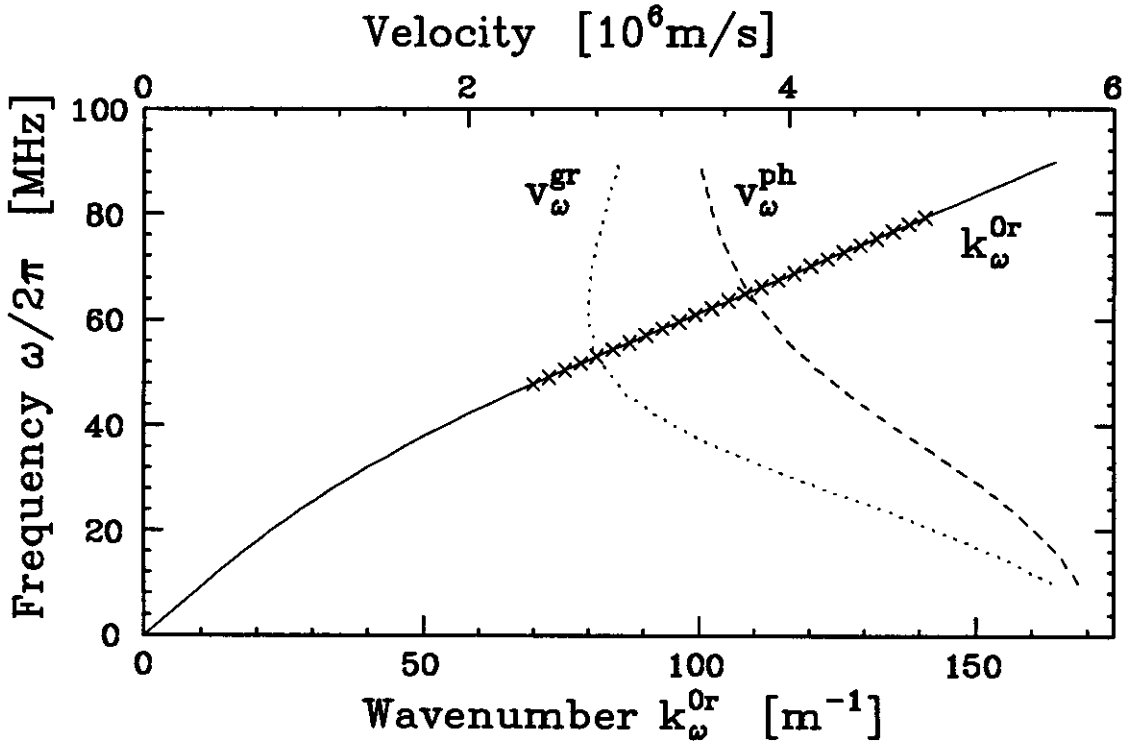

Figure 2.3: Helix dispersion without a beam. The solid line is the theoretical calculation and the crosses are the measured average wavenumbers, k_ω^{0r}, in the first half of the helix. The dashed line is the calculated phase velocity, v_ω^{ph}, the dotted line is the calculated group velocity, v_ω^{gr}.

The waves on the beamless helix are damped, possibly due to dissipation

from the glue that connects the helix to the alumina rods. The damping rate, $-k_\omega^{0i}$, is determined by measuring the wave power versus distance. It is shown in appendix A in figure A.2. At 40 MHz, the attenuation over the entire length of the interaction region is 4.0 dB; at 60 MHz, it is 9.2 dB.

There are several methods to measure the beam velocity. First, for sufficiently weak cold beams of high enough velocity u_0 so that there is no beam-helix interaction (i.e. for $u_0 \geq 5.5 \times 10^6$ m/s), one can measure the beam dispersion and infer the beam velocity. Second, for interacting beams, one can measure the beam velocity using the Kompfner dip technique [34, 29]. Both measurements agree with one another within the experimental uncertainties of 4.0%. The results are used for calibrating the cathode: the actual beam voltage is found to be about 1.6 V smaller than the applied voltage V_c.

The measured beam velocity distribution function of the cold beam (i.e. when the velocity spreader grids are grounded) has a half-width of about 0.4 V. This spread is probably due to the inhomogeneous electric and magnetic fields in the region of the cathode.

The interaction impedance is measured using the Kompfner dip technique [34, 29]. Its theoretical values are calculated using equation (2.11) and the normal helix modes calculated in [16]. Figure 2.4 shows a plot of the measured and the theoretical impedance. The measurements are within 4.0% of the theoretical values. The interaction impedance decreases with decreasing phase velocity (increasing frequency) because the helix normal modes become increasingly peaked near the helix wires.

We determine the space-charge factor P_q from the measured dispersion of small cold beams of high enough velocity u_0, so that they are not interacting with the helix normal modes. Then $\mid \epsilon^h(\omega, k_\omega) \mid \gg 1$ and the cold beam dispersion relation

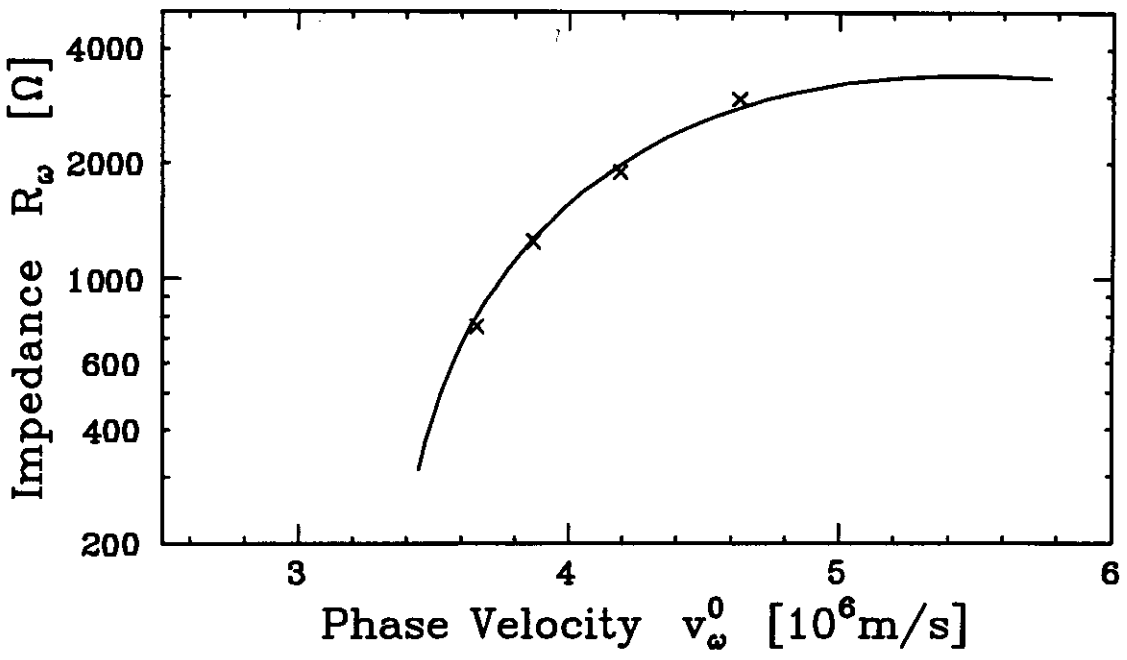

Figure 2.4: Interaction impedance versus phase velocity. The line is the theoretical calculation and the crosses are the measured values.

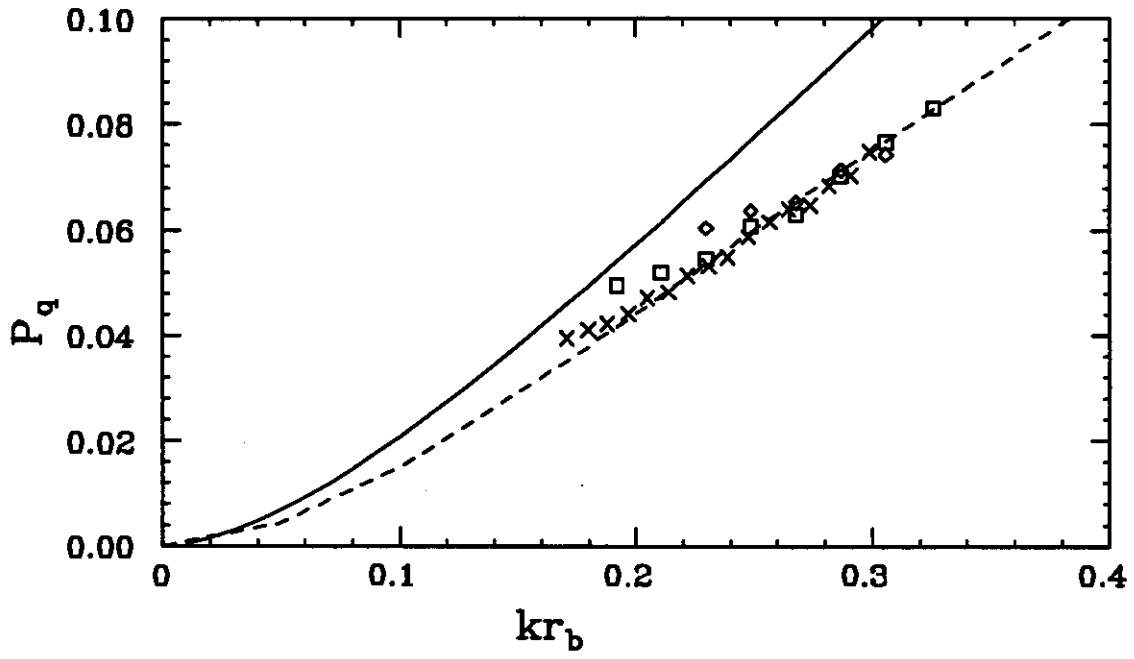

Figure 2.5: Plasma frequency reduction factor. The solid line is given by equation (2.14), the symbols are experimental data points (V_c = 78.4V, I_b = 16.2μA ($\diamond$); V_c = 78.4V, I_b = 32.4μA ($\times$); V_c = 98.4V, I_b = 22.5μA ($\square$), the dashed line is our fit to the experimental data, given by equations (2.27) and (2.28). k is the average wavenumber of the slower and the faster space-charge mode.

(2.16) simplifies to:

$$(\omega - k_\omega u_0)^2 = P_q(k_\omega r_b)\omega_p^2, \tag{2.26}$$

where the origin of the name of P_q becomes obvious. One can extract P_q from the beat pattern of the observed slow and fast space-charge mode. In figure 2.5 its values are shown for a few beams with different velocities and densities and compared with the predictions based on (2.14). The observed discrepancy is probably due to the assumptions of a flat density profile. In all following calculations of this dissertation we approximate the space-charge parameter P_q by the following expression:

$$P_q(kr_b) = \frac{1}{\sqrt{1 + (\frac{\gamma(kr_b)}{kr_b})^2}} \tag{2.27}$$

$$\gamma(kr_b) = 1.2\,kr_b + 0.69 \tag{2.28}$$

This fit is shown as a dashed line in figure 2.5.

2.5 Linear Dispersion

In this section the measured linear dispersion of the growing mode of a cold beam and a warm beam are compared with the values calculated from the measured beam properties. Good agreement is found in both cases, justifying the approximations made in treating the wave-beam interaction on a traveling wave tube as a coupled transmission line problem.

2.5.1 Cold Beam Dispersion

Figure 2.6 compares the measured dispersion of a single wave on a cold beam with the solutions of the cold beam dispersion relation (2.16) and with the solutions of the warm beam dispersion relation (2.21) for the measured velocity distribution of the cold beam. For wave phase velocities where we observe wave growth, we find good agreement of the measured growth rate and wavenumber shift with the

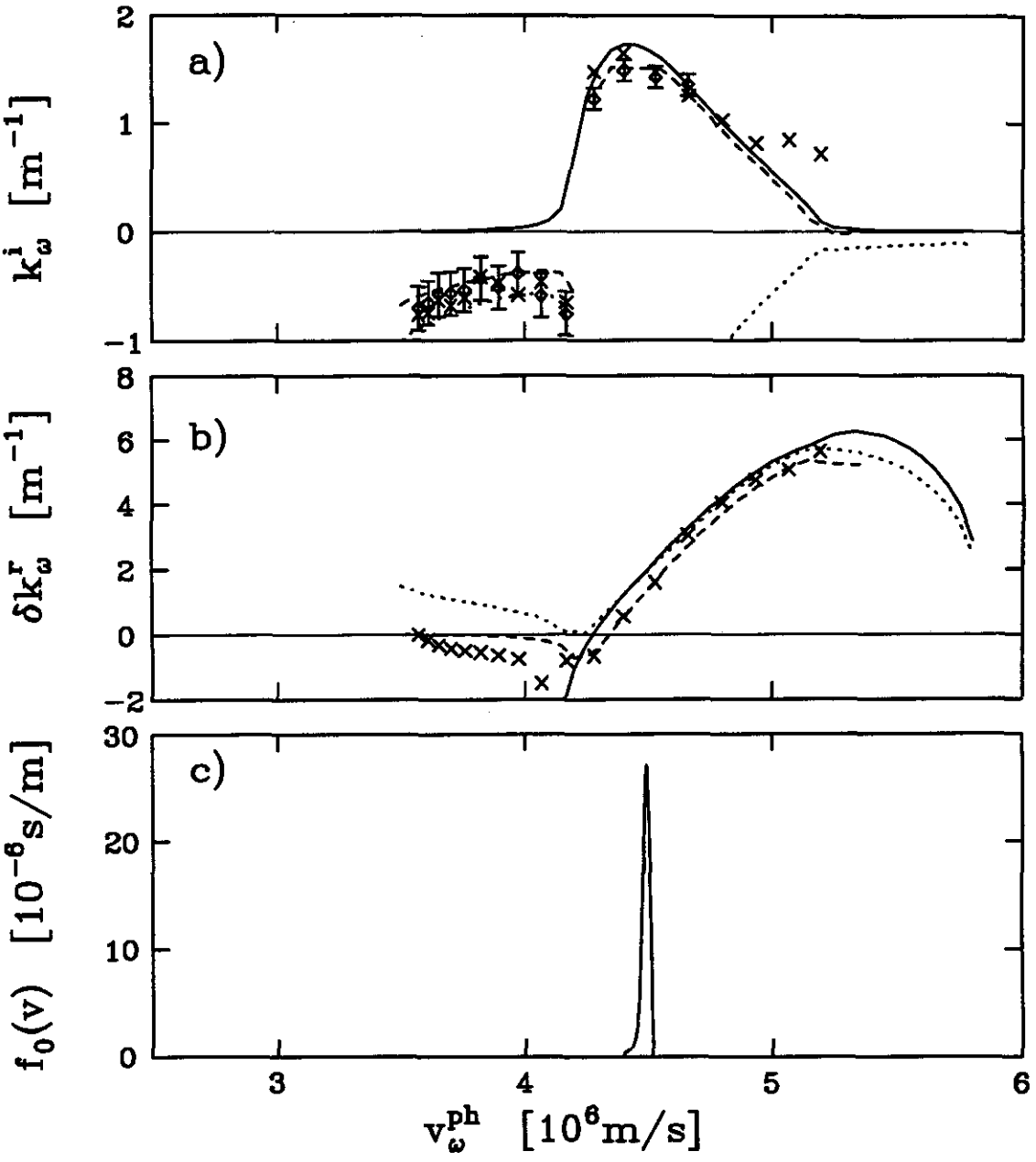

Figure 2.6: Cold beam dispersion: a) growth rate, b) wavenumber shifts, c) beam velocity distribution for $V_0 = 57.1$V and $I_b = 4.7\mu$A. The solid line is the growing, the dotted line is the damped root of the cold beam dispersion relation (2.16). The dashed line is the found root of the warm beam dispersion relation (2.21) for the measured velocity distribution. The crosses are obtained from fitting a superposition of two waves to the experimental data; the diamonds are straight line fits to the measured amplitude evolution.

growing solution of the dispersion relation. For wave phase velocities where we observe damping, we find good agreement with the damped solution of the dispersion relation. The roots of both dispersion relations, cold and warm, agree well with one another.

We measure the growth rate of a wave - as described before - by fitting a straight line to the logarithm of the wave amplitude near the end of the interaction region between $z = 1.5$ m and $z = 2.3$ m. The thus obtained growth rates for different phase velocities are shown as diamonds in figure 2.6a. For phase velocities larger than the velocity of the beam, this method is not useful since two normal modes of the cold-beam-helix system of comparable amplitude are being excited that result in a spatial beat pattern. In this case we fit the spatial evolution of the complex amplitude to the superposition of two exponentially growing waves of different amplitudes, growth rates, wavenumbers and initial phases. The growth rates of the waves with the larger amplitude (as a result of the fit) are shown as crosses in figure 2.6. This fit procedure yields the wavenumber shift of the growing normal mode, in addition to the growth rate. It is shown in figure 2.6b. In both cases the fits are done in the second half of the interaction region where the wavenumbers and damping rates of the beamless helix are approximately spatially constant (appendix A).

We numerically find the roots of the cold beam dispersion relation (2.16) for the measured beam velocity u_0, the measured beam plasma frequency ω_b and the plasma frequency reduction factor, P_q. For each frequency ω, it has three forward-propagating roots, that are characterized by a certain growth rate and wavenumber shift. In general we find a growing root, a non-growing root and a damped root. In figure 2.6 we only plot the two roots that we experimentally observe, the growing root and the damped root. For phase velocities for which the wave grows ($v_\omega^{ph} > 4.15 \times$

10^6m/s), we find good agreement between our experimentally measured growth rates and wavenumber shifts and the growing root of the cold beam dispersion relation (shown as a solid line). For phase velocities for which the wave damps ($v_\omega^{ph} < 4.15 \times 10^6$m/s), we find good agreement with the damped root (shown as a dotted line). We probably observe the damped root rather than the non-growing root, because the non-growing root would require larger values of the wavenumber shift and is therefore not excited as strongly as the damped root.

We can also find the roots of the warm beam dispersion relation (2.21) for the measured velocity distribution of the cold beam by numerical integration. The found root can be easily identified and agrees well with a root of the cold beam dispersion relation. The measured distribution is shown in figure 2.6c. In general our numerical scheme for finding the roots of the warm beam dispersion (2.21) finds only one forward propagating root. The roots of adjacent frequencies (corresponding phase velocities are plotted) do not necessarily correspond to the same branch of the dispersion relation. In figure 2.6a,b we connect the found roots with a dashed line. At about $v_\omega^{ph} \approx 4.15 \times 10^6$m/s a branch jump occurs. For higher phase velocities the growing root of the cold beam dispersion is found, for smaller phase velocities the damped root is found. In both cases we find good agreement between the values of the roots of the cold beam dispersion and the warm beam dispersion, thereby confirming that a δ-function is a good approximation of the experimental cold beam.

2.5.2 Warm Beam Dispersion

Figure 2.7 compares the measured dispersion of a single wave on a warm beam with the solutions of the warm beam dispersion relation (2.21) for the measured velocity distribution. We observe good agreement between the experimentally observed growth rates and wavenumber shifts and the found root of the dispersion relation. At lower phase velocities the Landau-approximation and the neglect of the

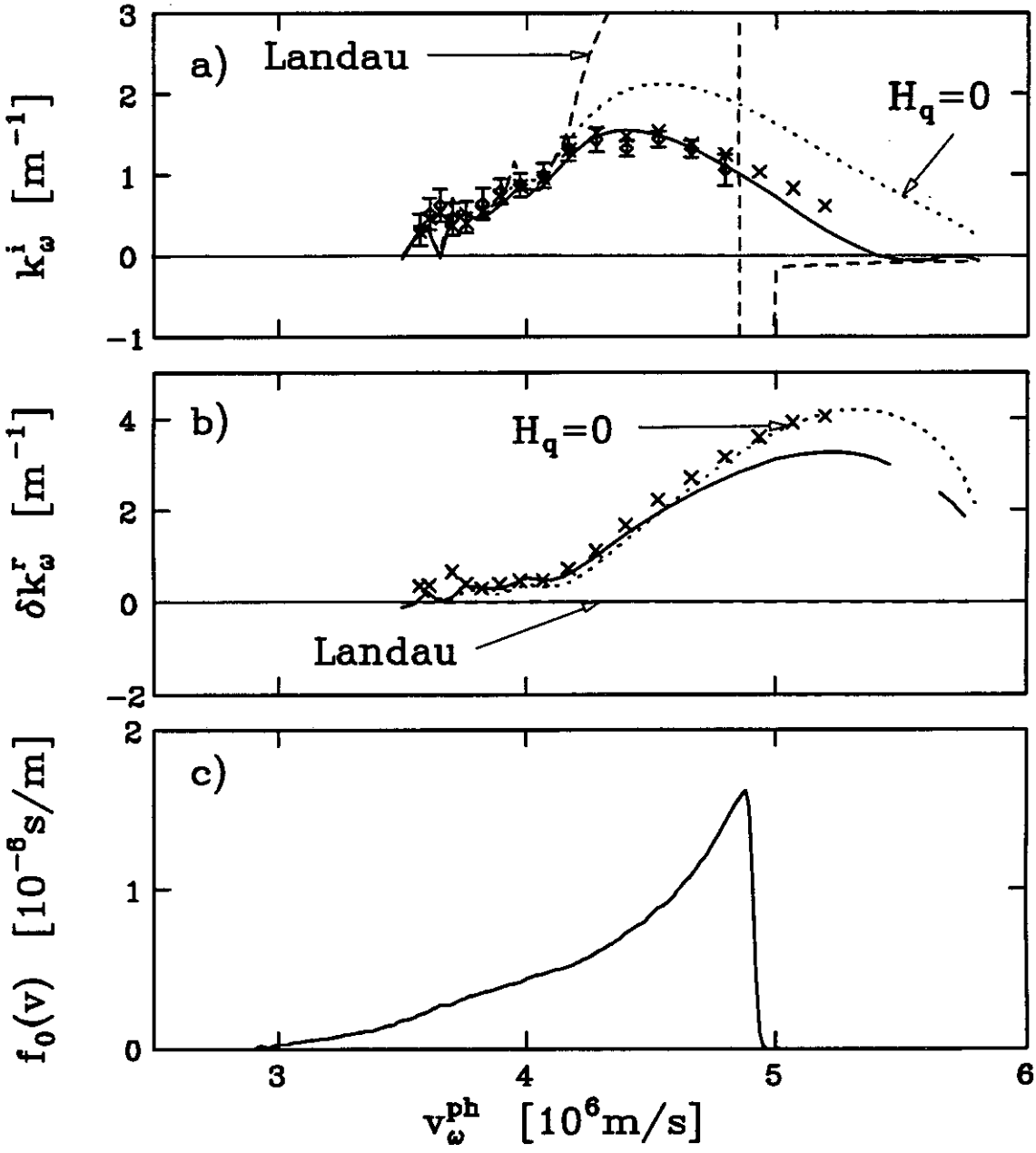

Figure 2.7: Warm beam dispersion: a) growth rate, b) wavenumber shifts, c) beam velocity distribution for V_c = 65.V, I_b = 80μA, V_{s1} = 40V, V_{s2} = 1800V and V_{s3} = 0V. The solid line is the solution of equation (2.21), the dashed line is the Landau approximation (2.23), the dotted line is the solution of equation (2.21) neglecting H_q. The crosses are the results of a two-wave-fit to the data and the diamonds are the results of fitting a straight line to the wave amplitude.

space-charge contribution are good approximations.

Figure 2.7a and b show the measured and the calculated growth rates and wavenumber shifts of the growing wave on a warm beam. The measured growth rates are obtained by fitting a straight line to the measured amplitude evolution (shown as diamonds) and by fitting a superposition of two waves to the evolution of the complex amplitudes (shown as crosses) between $z = 1.5$ m and $z = 2.3$ m. For phase velocities larger than the largest velocity of the beam (4.9×10^6m/s) a beat pattern is observed and a straight line fit to the amplitude is not possible.

We find the roots of the warm beam dispersion relation (2.21) by numerical integration over the measured velocity distribution, shown in figure 2.7c. For all phase velocities we find only one root which are connected by a solid line in figure 2.7a and b. They agree well with the measured growth rates and wavenumber shifts. For comparison the growth rates and wavenumber shifts of the Landau approximation (equations (2.23)) are shown as a dashed line. Its predictions approximately agree with the roots of the dispersion relation at phase velocities smaller than 4.2×10^6m/s.

The dotted line in figure 2.7a,b shows the roots of the warm beam dispersion when we neglect the space-charge contribution H_q. The obtained roots disagree with the previously obtained roots for phase velocities larger than 4.2×10^6m/s. This is further elucidated in figure 2.8. There the calculated space-charge term is shown for different phase velocities. It can be seen that the approximation that H_q be much smaller than unity breaks down near the edge of the velocity distribution function, i.e. for $v_\omega^{ph} > 4.5 \times 10^6$m/s. So we conclude that neglecting space-charge contributions and using the Landau approximation are only justified at low phase velocities ($v_\omega^{ph} < 4.2 \times 10^6$m/s for this case) far from the edge of the velocity distribution function.

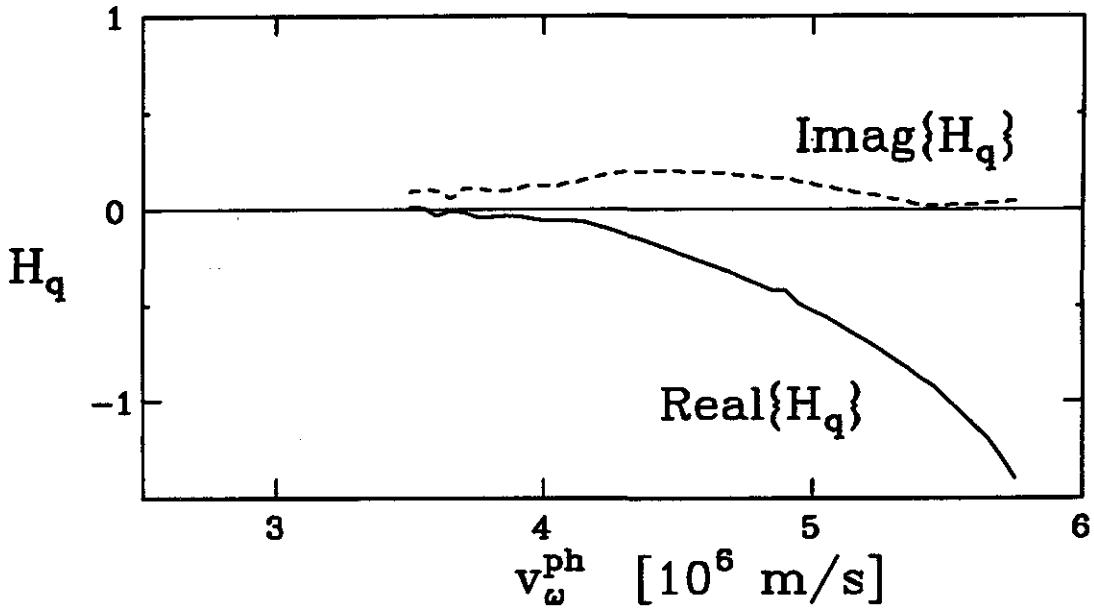

Figure 2.8: Space-charge contribution H_q for the solutions of the warm beam dispersion shown in figure 2.7, calculated from equation (2.22).

Chapter 3

Weak Warm Beam Instability

3.1 Introduction

This chapter describes the nonlinear saturation of a broad spectrum of waves excited by a warm electron beam on a traveling wave tube. We observe significant mode-coupling between the Fourier modes of the spectrum well before saturation, and we find that the properties of this mode-coupling are consistent with a four-wave coupling model. We also investigate ensemble-averaged quantities, such as the growth rates of the waves and the beam diffusion coefficient, and we find reasonable agreement with quasilinear theory for most of the evolution.

The one-dimensional interaction of a weak electron beam and a plasma is one of the most extensively studied problems in plasma physics. It has been treated analytically [2, 20, 21, 45, 1, 23, 38, 39], computationally [4, 59, 19, 44, 11] and experimentally [50, 35, 63] and is a simple prototype for a wide class of physical systems. Because of the beam, the overall electron velocity distribution has a region of positive slope, and plasma waves with phase velocity in this region can grow at the expense of beam kinetic energy. Eventually these unstable waves reach a large enough amplitude to couple nonlinearly with each other and to react back on the electron beam, decreasing the slope of the distribution function. The interesting question is: How does this nonlinear saturation occur?

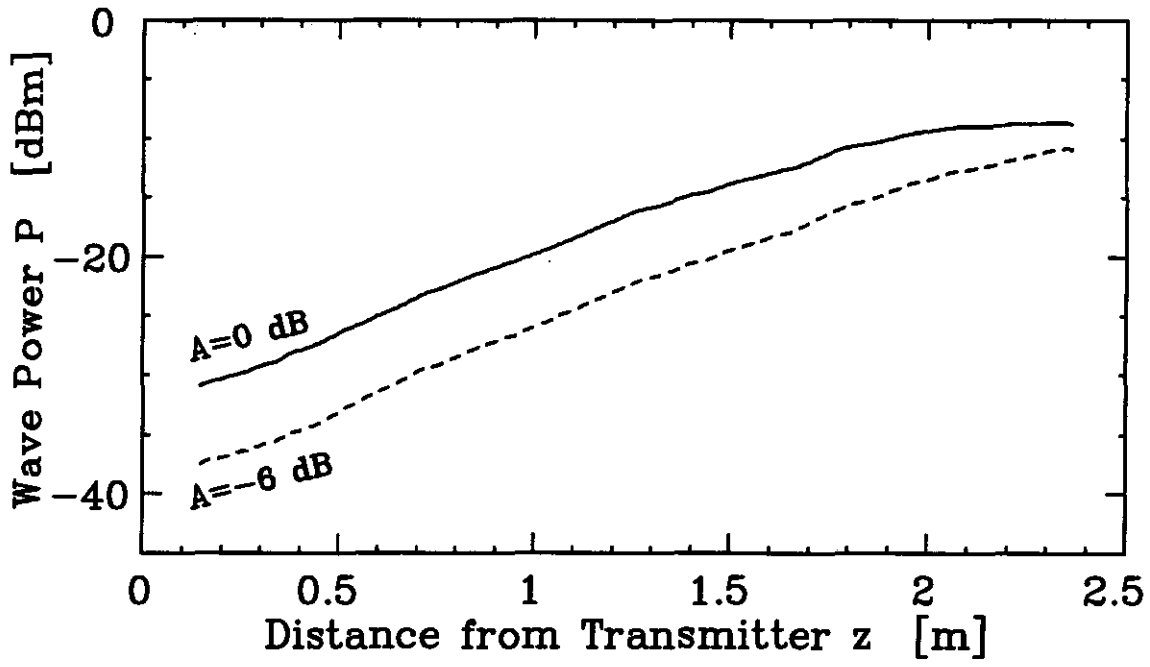

Figure 3.1: Evolution of the total wave power of all launched waves. The beam parameters are: $V_c = 70$ V, $I_b = 120\mu$A, $V_{s1} = 0$ V, $V_{s2} = 1750$ V, $V_{s3} = 48$ V, $V_p = 2$ V

The TWT experiment is similar to these beam-plasma experiments, since we believe from theory that the main role of the plasma is to support the waves as a linear dielectric. The TWT is well suited to study the instability because the background noise is low and the initial conditions can be completely defined. In the following three figures we show some of the generic instability properties in our experiment. This chapter will then quantify the observations.

The total wave power grows exponentially for some distance, then fully saturates near the end of the interaction region, as shown by the solid line in figure 3.1. The total gain in wave power is about 25 dB, i.e. an increase of about 300. If the initial spectrum is launched at a lower level, saturation will not be complete at the end of the interaction region, as shown by the dashed line. We characterize the launch level by A, which is the number of dB below the launch level that gives saturation at $z = 2.3$ m.

Even though the launched wave spectrum was a smooth function of velocity (but random in its phases), the spectrum becomes jagged with distance. Near saturation adjacent modes may differ in amplitude by 100%, and low phase velocity modes become 50% decorrelated from their launch values. This is shown in figure 3.2. This jaggedness is the result of mode-coupling due to the nonlinear motions of the beam electrons. This coupling has been previously observed in computer simulations and in experiments, but has not been studied quantitatively. We study the mode-coupling by typically launching and receiving 450 modes with 8 bits of amplitude accuracy. In addition close to saturation we do observe wave growth also at frequencies outside of the launched spectrum. They are nonlinear coupling products and not easily measured with our setup. Since the total power of these waves is small compared to the total power (less than 1 %) we have neglected them is this investigation. This means that the displayed spectra are artifically truncated below $v_\omega^{ph} = 3.55 \times 10^6$ m/s and above $v_\omega^{ph} = 5.15 \times 10^6$m/s.

The beam velocity distribution becomes flattened and spreads as the beam diffuses due to the wave field. Figure 3.3 shows the measured final electron beam velocity distribution at the end of the machine when no waves are launched (dashed curve) and when the broad spectrum of figure 3.2 has been launched (solid). The velocity distribution at saturation has flattened out in the range of the phase velocities of the unstable waves.

We are interested in the regime where at the onset of nonlinearities the spectrum of waves is very broad. In this regime the wave autocorrelation length is smaller than both the growth length and the turbulent trapping length, and these lengths are smaller than the TWT interaction length. This can be expressed as

$$l_{ac} \ll k_i^{-1}, 3l_{tt} \lesssim L \ll l_p \tag{3.1}$$

Here l_{ac} is the autocorrelation length of the spectrum as seen by a beam electron

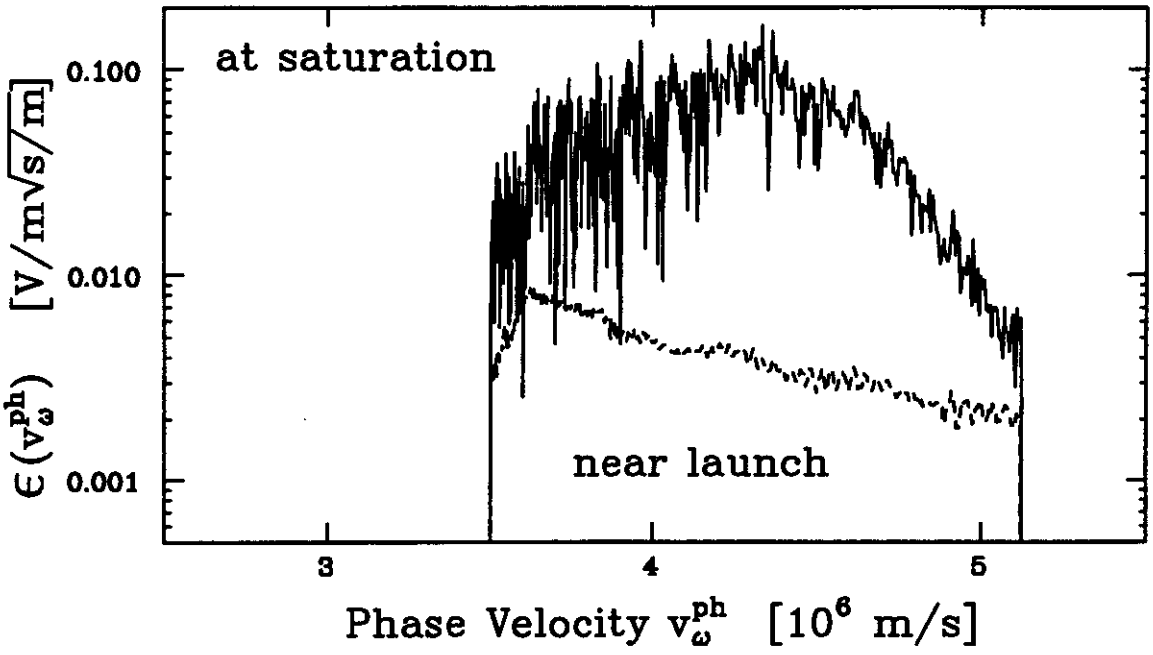

Figure 3.2: Electric field density $\epsilon(v_{ph})$, (defined in (3.11)), near launch (dashed) and saturation (solid). Beam parameters as in figure 3.1 and $A = 0$ dB, N=1024.

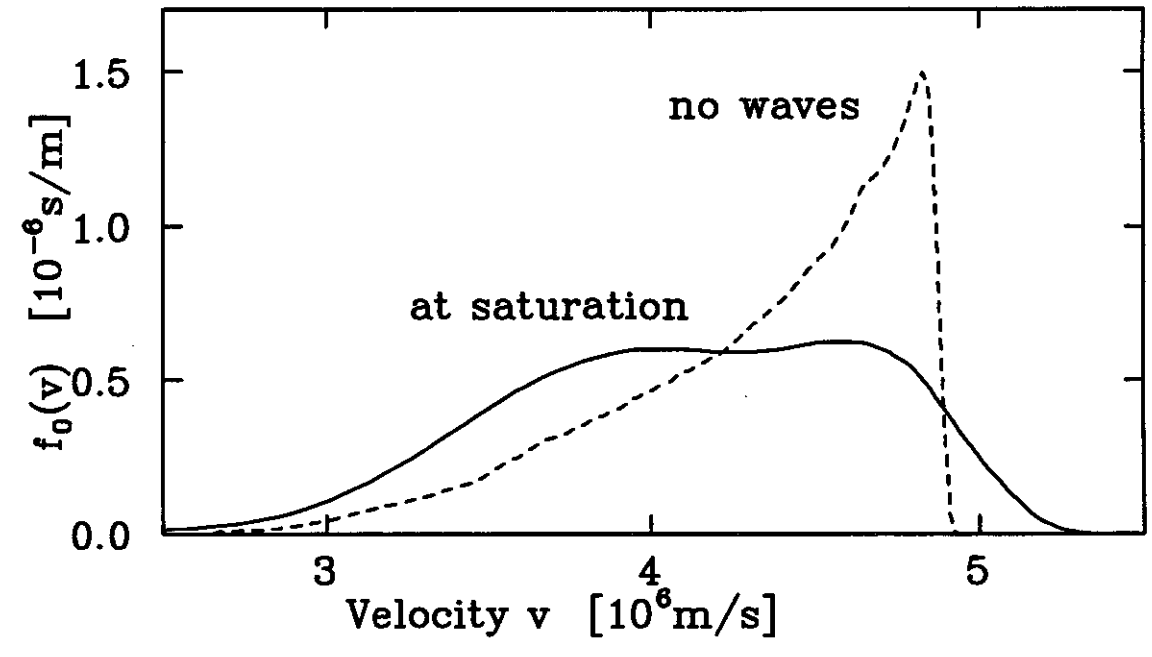

Figure 3.3: Beam time-averaged velocity distribution near launch of the waves (dashed) and at saturation (solid). Beam parameters as in figure 3.1.

of velocity v; it is the approximate distance over which a resonant electron looses phase coherence with the waves of the spectrum. k_i is an average growth rate of an unstable wave, so k_i^{-1} is a typical length scale for the evolution of the spectrum. l_{tt} is the turbulent trapping length of the spectrum; it is the approximate distance over which an electron moves by a wavelength relative to its resonant wave because of nonlinear wave-particle interactions. L is the length of the interaction region in the TWT. l_p is the approximate distance an electron would have to travel until it notices that the launched waveform repeats itself. Approximate expressions for these length scales will be given in section 3.2.1.

This inequalities are a refined version of the one given in chapter 1. The first inequality ensures that a resonant beam electron receives *many small* random "kicks" over the distance of a growth length of the spectrum. The requirement $l_{ac} \ll k_i^{-1}$ ensures that the phase of the electric field seen by an electron changes sign *many* times over a growth length. The requirement $l_{ac} \ll 3l_{tt}$ is equivalent to stating that the phase changes of the electric field occur many times over the distances that it would take an electron to complete one trapped particle orbit in a resonant wave with the rms electric field of the spectrum. Then the random acceleration of the electron can be considered *small.*

The second inequality implies that growth and diffusion can be observed within the length of the apparatus. Finally, the third inequality requires that many wave-particle resonances overlap, and that the interaction region is not so long that the electrons can resolve the periodicity of the launched waveform.

Part of the fascination with this problem derives from the simple and physically compelling set of "quasilinear" (QL) equations, originally proposed [18, 67] to describe the nonlinear saturation of the weak warm beam instability. These equations are the centerpiece of weak turbulence theory [52]. They are generally thought

to be applicable if the inequalities of equation (3.1) are fulfilled and if $k^i/k^r \ll 1$. In appendix B we derive them for the TWT.

Quasilinear theory predicts that the local growth of the electric field is given by the linear dispersion relation with the full beam velocity distribution function replaced by the **local, time-averaged** distribution. Further, QL theory predicts that the beam velocity distribution diffuses with a diffusion coefficient proportional to the square of the electric field at each phase velocity. This is described algebraically as:

$$\frac{dE_\omega(z)}{dz} = -ik_\omega(z)E_\omega(z) \tag{3.2}$$

$$\text{and } v\frac{\partial f_0(v,z)}{\partial z} = \frac{\partial}{\partial v}D(v,z)\frac{\partial f_0}{\partial v}. \tag{3.3}$$

The complex wavenumber $k_\omega(z) = k^r_\omega(z) - ik^i_\omega(z)$ and the diffusion coefficient $D(v,z)$ are given in equations (B.16) and (B.19), respectively.

It would be wrong to think that the quasilinear equations are derived rigorously from the Vlasov-Poisson equations. A set of terms in the Vlasov equation, the so called "mode-coupling terms", are dropped even though they are not small. The presumption is that the coupling is random and averages out. The resulting simplified equations still conserve particle number, momentum and energy, and provide a simple and physically reasonable description of the saturation process. It is important to check those equations experimentally. To what extend do these simplified equations provide an accurate and complete description of the nonlinear saturation and what are the properties of the neglected mode-coupling?

We observe mode-coupling between the Fourier modes of the launched waveforms and investigate it with "test-modes". A Fourier mode is considered a test-mode if changing its initial amplitude by 100% has negligible effect on the evolution of all the other modes. We decompose the received test-mode into a component T that depends linearly on the launched (*transmitted*) test mode and a second component

S that accounts for the power *scattered* from all other modes. The properties of the scattered and the transmitted component can be described with a four-wave coupling model [53]: the scatter components have growth rates about three times larger than the general wave growth rates; the scatter components of adjacent modes evolve very differently; the transmitted components of adjacent modes evolve similar. In addition, we find that the growth rate of the transmitted component is smaller than the average wave growth rate. It has not yet been checked whether this last property is also in agreement with the model.

Close to saturation, the field amplitude probability distribution is found to deviate from a Gaussian distribution. The kurtosis decreases to -0.6 indicating that high fields occur less frequently, which can be interpretated as a transition to a frequency-modulated waveform.

We have measured the growth rates of the ensemble-averaged waves at different stages of the evolution. When $k_i^{-1} \lesssim l_{tt}$ the beam velocity distribution has changed little, and we find good agreement between the measured rates and the calculated QL rates (RB theory yields the same values). When $k_i^{-1} \approx l_{tt}$, the beam velocity distribution has changed noticeably and mode coupling is observed. The measured ensemble-averaged growth rates approximately agree with QL theory or are larger. For waves with phase velocities in the center of the spectrum, where the beam flattens first, the measured rates are always larger than the calculated rates. Here agreement with RB theory is better, but still not satisfactory. Limitations of the experiment that could contribute to this discrepancy will be discussed.

For a given (prescribed) electric field spectrum, we measure the diffusion of a small cold test beam. The measured diffusion coefficients generally agree with the predictions of QL and RB theory. In the case of the self-consistent evolution the observed diffusion is larger than the predicted diffusion. RB theory and QL theory

yield approximately the same results in the considered case.

Roberson and Gentle [50] measured the final state of the beam-plasma instability and found good agreement with QL theory for the final spectrum and velocity distribution function. In a similar experiment, Krivoruchko *et al.* [35] found enhanced growth rates and diffusion rates that they attributed to correlation phenomena. Their investigation was qualitative, and it is doubtful that QL theory was applicable to all their cases.

Tsunoda *et al.* [65] performed experiments on the TWT, and found saturation in qualitative agreement with QL theory. At the onset of nonlinearities, they found that the ensemble-averaged growth rate was not enhanced above the measured linear rate, which they assumed to also be the quasilinear growth rate.

Computer simulations are difficult because of the separation of time-scales required to meet the quasilinear conditions. A number of authors [4, 59, 19, 44, 11] have found enhanced ensemble-averaged growth rates or diffusion coefficients. It is, however, still questionable whether their calculations met all requirements.

Using simple arguments QL theory appears invalid when the turbulent trapping length is comparable to the growth length, i.e. when

$$k_i^{-1} \approx l_{tt} \tag{3.4}$$

where

$$l_{tt} \approx (\frac{v^5}{\omega^2 D})^{1/3} \tag{3.5}$$

The turbulent trapping length, l_{tt},is the distance over which an electron should diffuse by a full wavelength relative to its resonant wave of frequency $\omega/2\pi$. Even though the waveform structures seen by an electron are ephemeral because $l_{ac} \ll k_i^{-1}$, it is now possible for them to exist long enough to cause changes in the phase-space of the electrons that are not satisfactorily described as a diffusive process. This occurs well before saturation.

Dupree [20] was the first of many authors to attempt to improve on quasilinear theory by retaining *some* of the mode-coupling terms. His approach leads to a diffusive broadening of the wave-particle resonance, and became known as "Resonance Broadening" (RB) theory. This broadening becomes appreciable when the electric field is strong enough so that $l_{tt} \approx k_i^{-1}$. However, as shown in [51], the mode-coupling terms *discarded* by Dupree also become important when $l_{tt} \approx k_i^{-1}$. Other attempts [1] to include some of the mode-coupling terms fail at the same threshold.

Recently Liang and Diamond [39] have argued, using more sophisticated closure schemes, that deviations of the growth rates from the quasilinear predictions are small in all ranges of the instability.

The reminder of this chapter is organized as follows: In section 3.2 we discuss the length scaling in the experiment and how we calculate ensemble averages. In section 3.3 we present our mode-coupling experiments. In section 3.4 we show statistical properties of the waveform. In section 3.5 we compare the measured ensemble-averaged growth rates and in section 3.6 we compare the measured diffusion rates with the predictions of QL and RB theory. In section 3.7 we compare the power loss in the beam with the power gain of the wave spectrum.

3.2 Quasilinear Regime

In this section we investigate the quasilinear requirements given by equation (3.1) and show that we can choose the electric field spectrum and the beam to satisfy the requirements. This will lead us to discuss the requirements for ensemble averages.

3.2.1 Length Scales

Autocorrelation Length l_{ac}

We define the spectral autocorrelation function $G_s(z, \Delta z, v)$ of the electric field as seen by an electron moving with velocity v acoording to:

$$G_s(z, \Delta z, v) \equiv \frac{< E(z,t)E(z+\Delta z, t+\Delta z/v) >}{< E^2(z,t) >^{0.5} < E^2(z+\Delta z, t+\Delta z/v) >^{0.5}} \tag{3.6}$$

where the poined brackets average over the waveform. the autocorrelation length l_{ac} is the shortest distance Δz for which the magnitude of the autocorrelation function never exceeds e^{-1}. For a waveform with an electric field given by

$$\mid E_\omega(z) \mid^2 = \mid E_{\omega_0}(z) \mid e_{(\omega-\omega_0)^2/\Delta\omega_{tot}^2} \tag{3.7}$$

we obtain for the autocorrelation length:

$$l_{ac} = \frac{2v}{\Delta\omega_{tot}(1 - \frac{v}{v_{\omega_0}^{gr}})}, \tag{3.8}$$

where $v_{\omega_0}^{gr}$ is the group velocity of the wave at frequency ω_0. This length has an easy physical interpretation: it is the distance over which the phases of two waves near the edges of a spectrum change by π with respect to one another as seen in the frame of a resonant electron.

Growth Length $(k_\omega^i)^{-1}$

In order to obtain growth rates for spectra that are jagged in the nonlinear regime, it is necessary to smooth the spectrum by ensemble-averaging. In the

following section we will show that averaging the square of the electric field over a number of nearby Fourier-modes is a suitable and convenient way of calculating an ensemble-average. If the total spectrum consists of about 500 modes it suffices to average over about 20 nearby modes in order to obtain growth rates that are a smooth function of phase velocity. An example of the ensemble-averaged growth rates is shown in figure 3.22. The growth rates are determined by fitting a straight line to the logarithm of the ensemble-averaged electric field Fourier component E_n, over 0.25 m centered at the point of interest.

Turbulent Trapping Length l_{tt}

The turbulent trapping length is the approximate distance over which an electron moves by one wavelength with respect to its resonant wave because of nonlinear wave-particle interactions. We calculate it self-consistently from equation (B.28) where we use the helix wavenumbers k_n^{0r} and the measured ensemble-averaged growth rates k_n^i. Because of the weak dependence on the diffusion coefficient, it can be estimated from

$$l_{tt}(v) \approx \left(\frac{3v_b^5}{\omega^2 D^{ql}(v)}\right)^{\frac{1}{3}} \tag{3.9}$$

where ω is the frequency of the wave with phase velocity $v_n^{ph} = v$ and v_b is the mean velocity of the beam.

"Periodicity Length" l_p

The spectral autocorrelation function $G_s(z, \Delta z, v)$ is periodic in Δz because the launched waveform $E(z,t)$ is periodic in time with period T. The periodicity length l_p is the distance l_p that an electron with velocity v would have to travel until it detects this periodicity:

$$l_p \equiv \frac{v}{\delta\omega(1 - \frac{v}{v_{gr}})} \tag{3.10}$$

where $\delta\omega = 1/T$ is the frequency difference between neighboring Fourier components of the spectrum.

Length Scale Ordering

Figure 3.4 shows the product of the autocorrelation length and the ensemble-averaged growth rates, $l_{ac} * < k_\omega^i >$, at launch and near saturation. The growth rate was taken at the phase velocities that correspond to the beam velocities. Except for very low phase velocities, the requirement that $l_{ac} * k_\omega^i \ll 1$ is reasonably well fulfilled even at saturation.

Figure 3.5 shows the ratio of autocorrelation length to turbulent trapping length at launch and at saturation. Near saturation the requirement $l_{ac} \ll 3l_{tt}$ is not well fulfilled: the turbulent trapping length has become small due to the large electric fields, while the autocorrelation length has become large because the spectrum has become less broad.

We typically launch waveforms with about 500 modes that have a period of $T \approx 8.5\mu$s. Then the last inequality of equation (3.1) is well fulfilled with $k^{i-1}/l_p \approx 0.02$ and $l_{tt}/l_p \approx 0.03$.

3.2.2 Ensemble-Averages

In this subsection we describe how we calculate ensemble-averages of the electric field spectrum. In order to compare ensemble-averages of waveforms of different length it is convenient to calculate an electric field density that is independent of the number of modes $N/2$ that constitute the spectrum. We visualize the strong coupling between waves and beam electrons of equal velocity by calculating this electric field density in phase velocity rathern than in frequency as it is often done. The

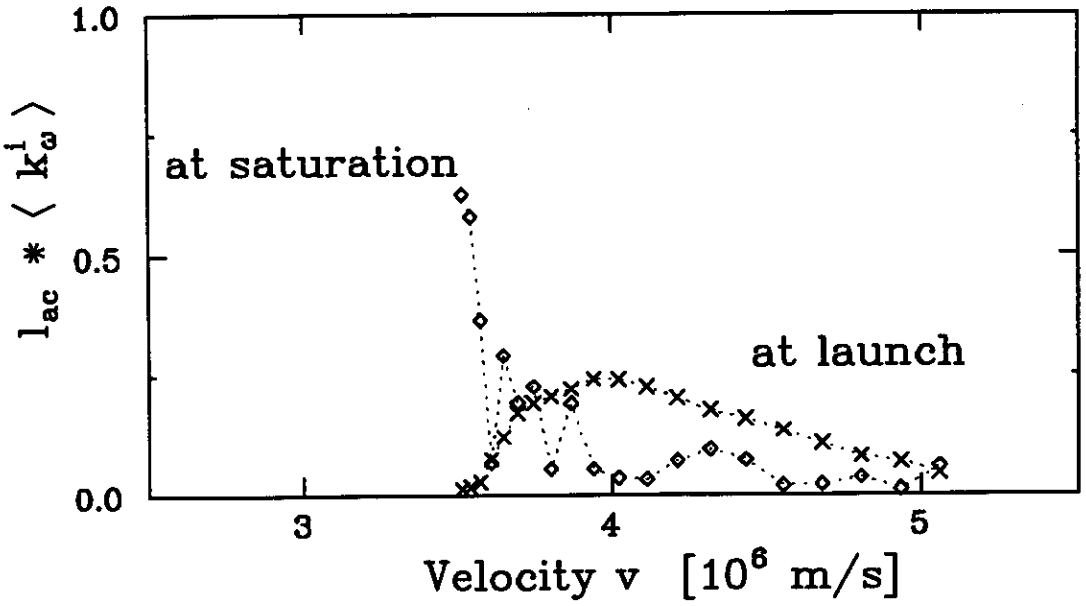

Figure 3.4: Weak warm beam requirement: $k^i * l_{ac} \ll 1$. Beam parameters as in figure 3.1.

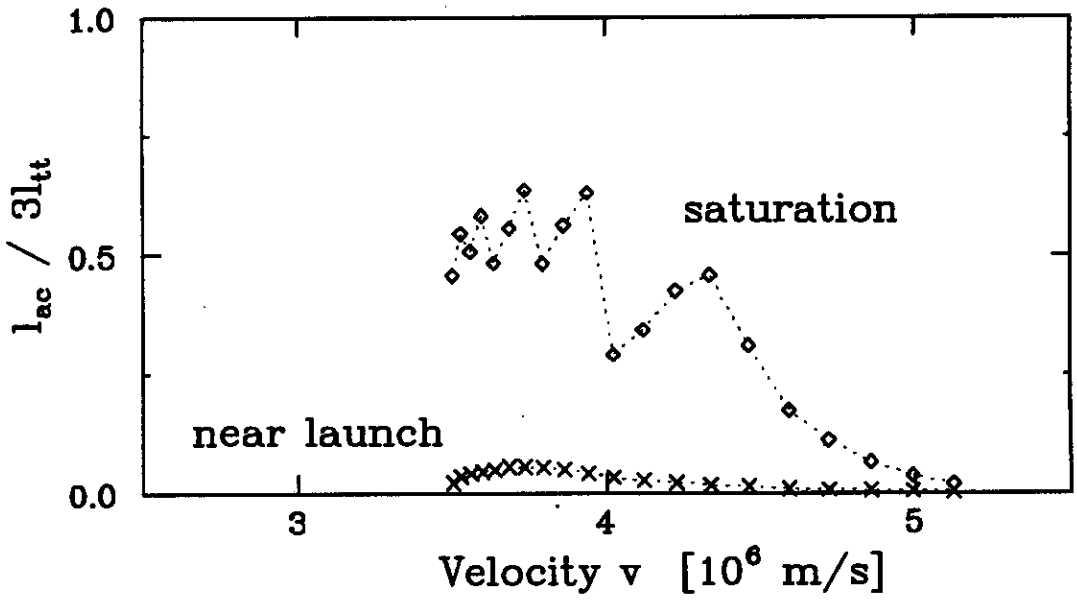

Figure 3.5: Weak warm beam requirement: $l_{ac}/3l_{tt} \ll 1$. Beam parameters as in figure 3.1.

electric field density is defined as follows:

$$\mathcal{E}(v_{ph}, z) \equiv \sqrt{\frac{\overline{|\ E_n(z)\ |^2}}{\delta v_n^{ph}}}, \tag{3.11}$$

where δv_n^{ph} is the difference in phase velocity of two adjacent modes of the spectrum, i.e.

$$\delta v_n^{ph} = \frac{\omega_n}{k_n^{0r}} - \frac{\omega_{n+1}}{k_{n+1}^{0r}}. \tag{3.12}$$

In our experiments we launch a periodic waveform with a large number of modes. Its period T is much longer than any physically relevant time of the experiment, e.g. the transit time of an electron through the interaction region. Therefore doing an experiment with a long waveform constitutes doing a number of independent "trials" in one sweep, one immediately following the other, where the duration of each of these independent trials is approximately given by the electron transit time. Since the waves are almost completely absorbed at the ends, these trials are independent.

In most of our experiments, the mode amplitudes of the launched waveform are a smooth function of frequency, as can be seen in figure 3.2. In contrast, the mode phases are jagged, i.e. randomly chosen between 0 and 2π. Such waveforms are launched in order to visualize the strength of the mode-coupling. We calculate an ensemble-average of the measured spectrum in the nonlinear regime by replacing the electric field of each mode with the rms-value of the nearby modes:

$$\langle |\ E_n\ |^2 \rangle_{\Delta\omega} \equiv \frac{1}{\Delta N + 1} \sum_{m=n-\Delta N/2}^{n+\Delta N/2} |\ E_m\ |^2 \tag{3.13}$$

where $\Delta\omega$ is a label indicating the frequency width of the ensemble-averaging, i.e. $\Delta\omega = |\ \omega_{n+\Delta N/2} - \omega_{n-\Delta N/2}\ |$. ω_n is defined by equation (B.7). We call this ensemble-average a "nearby mode average".

A physically reasonable bandwidth for the ensemble-average is the minimal frequency separation $\Delta\omega$ between two waves that can be resolved by the electrons

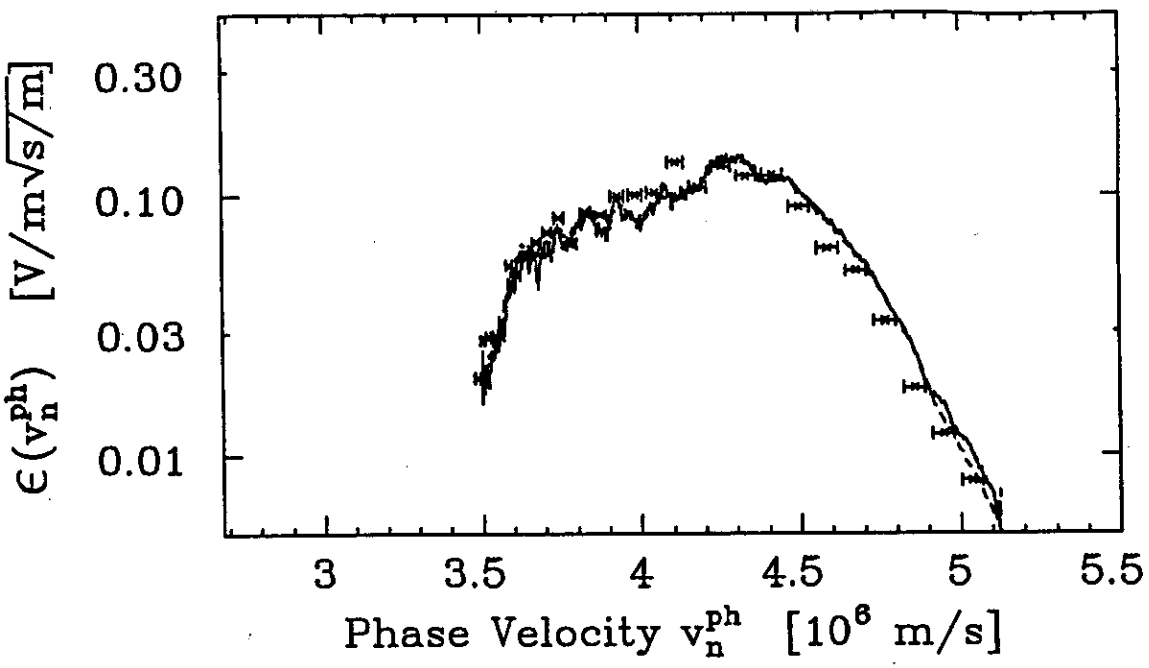

Figure 3.6: Comparison of ensemble-averages at saturation: frequency-average for spectrum with smooth launched spectrum (solid); frequency-average for spectrum with jagged launched spectrum (dashed); many waveform-average (crosses). The beam parameters are as in figure 3.2.

during their transit time through the interaction region. We estimate $\Delta\omega$ as:

$$\frac{\Delta\omega}{2\pi} \approx \frac{v}{2L(1-\frac{v}{v_{gr}})} \approx 2.5\text{MHz} \approx \frac{1}{20}\frac{\Delta\omega_{tot}}{2\pi} \approx 25\frac{\delta\omega}{2\pi} \qquad (3.14)$$

Thus our spectrum of $\Delta\omega_{tot}/2\pi \approx 50$ MHz bandwidth has about 20 "physical modes"[1] and the bandwidth of each physical mode corresponds to about 25 Fourier modes for a typical waveform of about 500 modes.

Figure 3.6 shows the ensemble-average for the spectrum shown in figure 3.2 as a solid line. We also show the received ensemble-averaged spectrum for a launched waveform with jagged mode amplitudes. In that case the launched amplitudes are Gaussianly distributed about the amplitudes of the smooth spectrum and the phases are chosen randomly. At satuation, both nearby-mode-averaged spectra are essentially the same. The measured time-averaged velocity distributions are indistin-

[1]This is probably a high estimate since mode-coupling between physical modes happens on a length scale given by $l_{tt} \leq L$.

guishable. We therefore conclude that waveforms with smooth spectra are suitable for obtaining ensemble-averaged growth rates, spectra or diffusion coefficients.

Alternatively, if we successively launch M very short waveforms, where each contains only about 20 modes, we can define an ensemble-average in the more traditional sense:

$$\langle \mid E_n \mid^2 \rangle_M \equiv \frac{1}{M} \sum_{m=1}^{M} \mid E_n^{(m)} \mid^2 \tag{3.15}$$

where $\mid E_n^{(m)} \mid$ is the the received mode amplitude at frequency ω_n when the mth waveform was launched. We call this ensemble-average an "initial phase average". At launch the modes of each member of the ensemble have the same amplitudes but randomly chosen phases. The crosses in figure 3.6 show the received initial-phase-averaged amplitudes for launched waveforms with about 20 modes. Their horizontal bars mark their width δv_n^{ph}. The initial-phase-averaged amplitudes agree with the nearby-mode-averaged amplitudes. This states that 20 modes are sufficiently many modes for calculating the initial phase ensemble averages. For waveforms with fewer than 7 modes the initial phase average deviates from the nearby mode average. Then the periodicity length is no longer much longer than the other length scales and we find that the time-average velocity distribution function becomes very dependent on the initial phases of the waveform.

3.3 Mode-Coupling

In this section we describe the properties of the mode-coupling that we observe in the nonlinear region of the weak warm beam instability. As an example, figure 3.7 shows the evolution of 5 adjacent Fourier modes for the case depicted in figure 3.2, where saturation is reached by the end of the apparatus. We see that nearby modes evolve very differently from one another and that at saturation the jaggedness of the spectrum has become strong. This jaggedness arises through mode-coupling caused by the nonlinear motion of the beam electrons.

We investigate this mode-coupling by different means. Measuring the probability distribution of the electric field modes within the bandwidth of a physical mode we can quantify the "jaggedness" of the spectrum and find that for low phase velocities and at saturation the mean of the distribution equals the standard deviation. Calculating the two-point correlation function of the electric field amplitudes we determine likewise that for low phase velocities at saturation the spectrum is completely decorrelated from the launched spectrum. By singling out a Fourier mode as a test mode, we can decompose its Fourier amplitude E_n into a component T_n that is linear in the launch amplitude of the mode and a scatter component S_n that is independent of it. We find that the ensemble-average growth rate of the scatter component is about three times larger than the ensemble-averaged growth rate of the spectrum. The growth rate of the transmitted component is smaller than the ensemble-averaged growth rate of the spectrum. Using "in-between test modes" we find that the frequency range of scattering out of one mode is approximately given by Dupree's trapping length. Using a hybrid of tri-spectral analysis and test mode analysis we find the same locality for scattering into one mode.

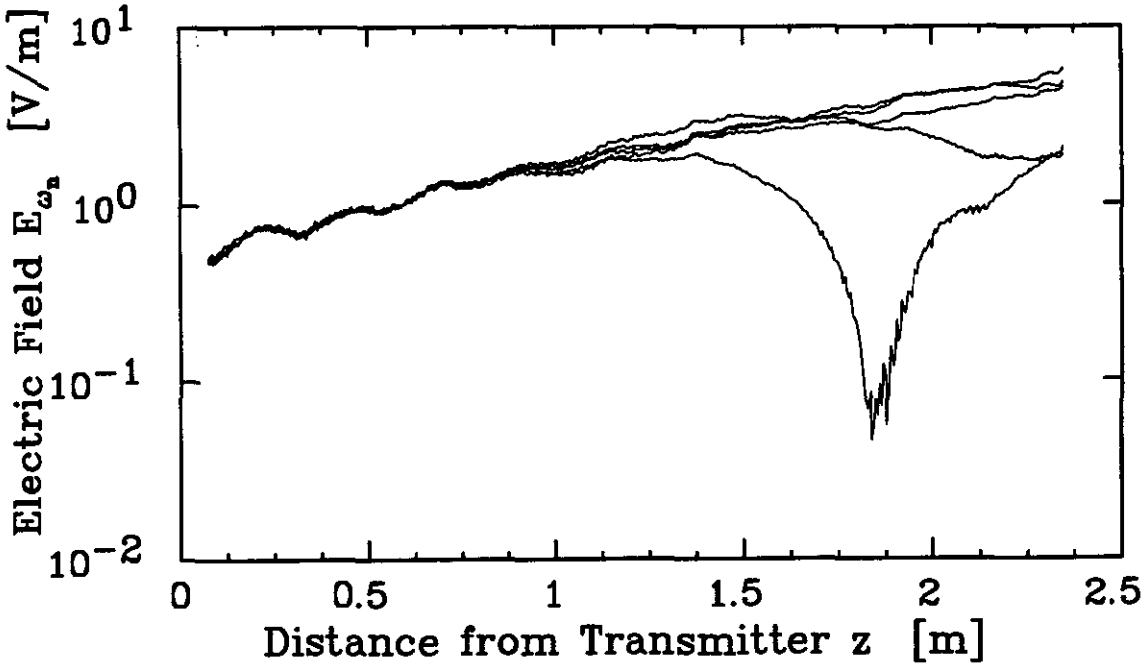

Figure 3.7: Evolution of 5 nearby Fourier modes 200-204 of the case shown in figure 3.2 from the linear regime into saturation, $A = 0$ dB, $N = 1024$.

3.3.1 Fourier Amplitude Probability Distribution

Figure 3.8 shows the distribution of the measured $N/2/25 \approx 80$ Fourier mode amplitudes around a single "physical mode" at low phase velocity $v^{ph} = 3.65 \times 10^6$ m/s. In the launched spectrum, corresponding to figure 3.2, all the about 80 Fourier modes have approximately the same amplitude. At positions further away from the transmitter, the mean of this distribution grows because of the growth of the electric field modes. In the nonlinear regime the width of the distribution grows faster because of mode-coupling: nearby modes no longer grow at the same rate. At saturation, the width of the distribution has become comparable to its mean, indicating that the mode-coupling effects are of the same order as the linear growth contributions.

Figure 3.9 shows the mean $\overline{E_\omega}$ and the standard deviation σ_ω of the Fourier amplitude probability distribution, shown in figure 3.8 at different positions and for

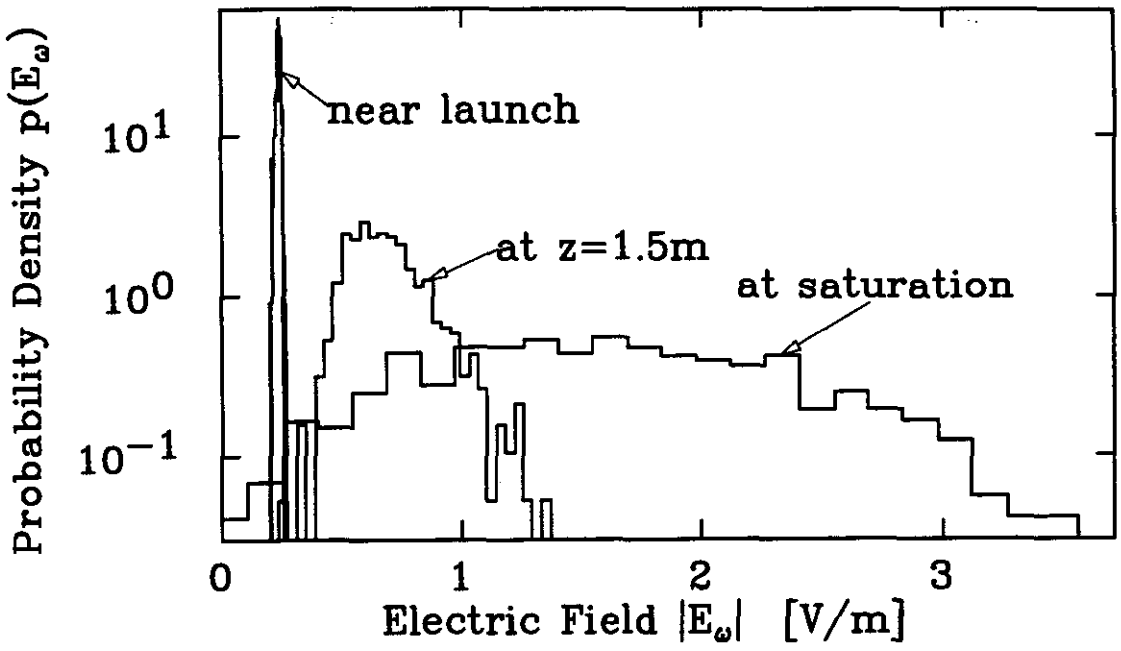

Figure 3.8: Probability distribution of Fourier amplitudes at different positions of the evolution from the linear regime to saturation. Distribution of the modes 764 to 836 for five waveforms, each with $N = 4096$ modes, corresponding to figure 3.2.

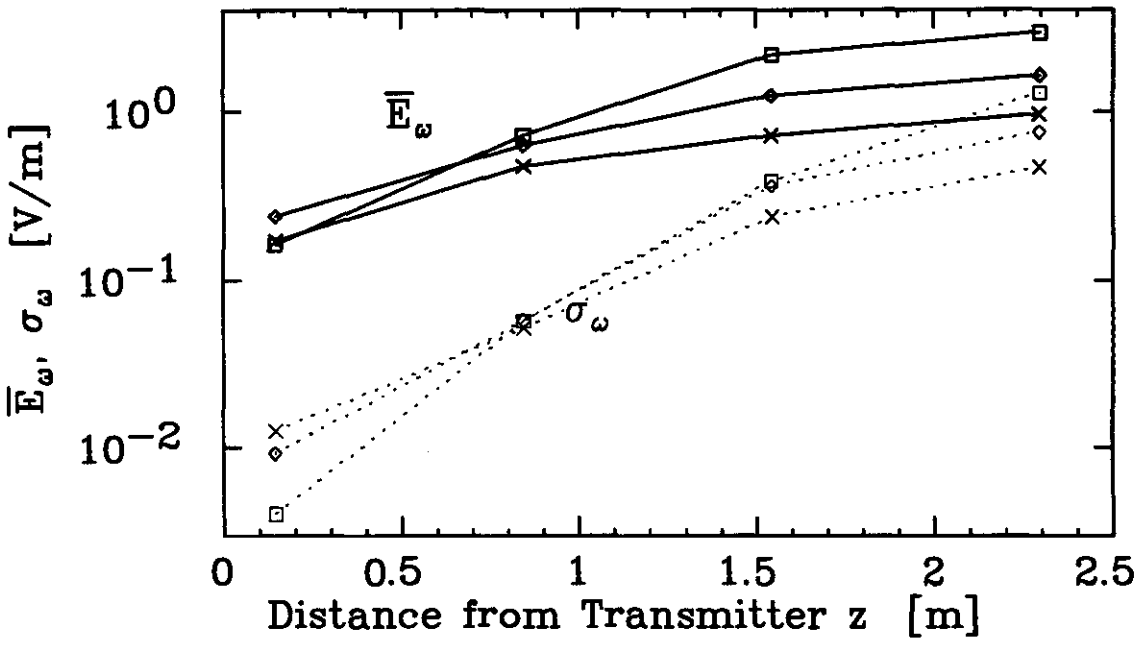

Figure 3.9: Mean $\overline{E_\omega}$ (thick solid line) and standard deviation σ_ω (thin dotted line) of the amplitude probability distribution versus distance from the transmitter for phase velocities $v_\omega^{ph} = 3.6 \times 10^6$ m/s (×), $v_\omega^{ph} = 3.8 \times 10^6$ m/s (◇) $v_\omega^{ph} = 4.15 \times 10^6$ m/s (□). Parameters as in figure 3.2, $A = 0$ dB, $N = 4096$

different phase velocities. In all the shown cases the ratio of the mean to the standard deviation decreases by about a factor of 5 from the linear region to saturation. Only low phase velocities are shown because reflections of the waves widen the probability distribution function at high phase velocities. The two-point correlation function, calculated in the following section is not hampered by these reflections.

3.3.2 Two-Point Correlation

The two-point correlation function of the electric field complex amplitudes shows that the mode-coupling is stronger at low than at high phase velocities. At low phase velocities, we find that the electric field at saturation is unrelated to the launched electric field.

The two-point correlation function of the complex electric field amplitudes statistically describes the degree of correlation between the complex amplitudes E_n of one mode measured at two positions z_1 and z_2. We say that perfect correlation exists if one complex number α can be found such that for **all** members m of the ensemble we have:

$$E_n^{(m)}(z_2) - \alpha E_n^{(m)}(z_1) = 0 \tag{3.16}$$

Notice that according to quasilinear theory perfect correlation exists for all regions of the instability.

We now use equation (3.16) to derive an expression for the two-point correlation function. In general it is true that

$$\langle \mid E_n(z_2) - \alpha E_n(z_1) \mid^2 \rangle \geq 0 \tag{3.17}$$

$$\Leftrightarrow \quad \langle \mid E_n(z_2) \mid^2 \rangle + \mid \alpha \mid^2 \langle \mid E_n(z_1) \mid^2 \rangle - 2Real\langle \alpha E_n(z_2) E_n^*(z_1) \rangle \geq 0 \tag{3.18}$$

From section 3.2.2 we know that we can calculate the ensemble average in two ways: by averaging over nearby modes for long waveforms (N¿500) and by averaging over

initial phases for short waveforms ($N \approx 20$). Approximating the last summand using Schwartz's Theorem we obtain:

$$\langle \mid E_n(z_2) \mid^2 \rangle + \mid \alpha \mid^2 \langle \mid E_n(z_1) \mid^2 \rangle - 2 \mid \alpha \mid \mid \langle E_n(z_2) E_n^*(z_1) \rangle \mid \geq 0 \tag{3.19}$$

This equation has solutions for $\mid \alpha \mid$ only if:

$$\mid \langle E_n(z_2) E_n^*(z_1) \rangle \mid^2 - \langle \mid E_n(z_2) \mid^2 \rangle \langle \mid E_n(z_1) \mid^2 \rangle \geq 0 \tag{3.20}$$

From this expression we define our two-point correlation function $C_n^2(z_1, z_2\rangle$ to be:

$$C_n^2(z_1, z_2\rangle \equiv \frac{\mid \langle E_n(z_2) E_n^*(z_1) \rangle \mid^2}{\langle \mid E_n(z_2) \mid^2 \rangle \langle \mid E_n(z_1) \mid^2 \rangle} \tag{3.21}$$

$C_n^2(z_1, z_2)$ is bound between 0 and 1. If the electric field amplitudes at two positions of all the members of the ensemble are correlated by a unique complex factor α then $C_n^2(z_1, z_2) = 1$; if they are statistically uncorrelated, i.e. if different members of the ensemble have different values of α, then $C_n^2(z_1, z_2) = 0$.

In figure 3.10 we show the correlation between the electric field amplitudes at fixed position (z_1) near the launch and varying position $\langle z_2)$. This is shown for different frequencies, i.e. phase velocities. At each frequency the ensemble average is calculated by averaging over ΔN nearby modes within the bandwidth of a physical mode. We find that at low phase velocities the saturation spectrum has less than 0.5 correlation with the launch spectrum, whereas at high phase velocities the correlation is larger, typically 0.8. Therefore mode-coupling is stronger at lower than at higher phase velocities.

3.3.3 Experimental Definition of a Test Mode

Typically we launch a waveform (m) whose spectrum consists of about 500 electric field Fourier modes $E_n^{(m)}(z)$ $(N = 1024)$ of comparable amplitude. Any mode can be considered a test mode if changing its initial amplitude $E_n^{(m)}(z = 0)$ has a

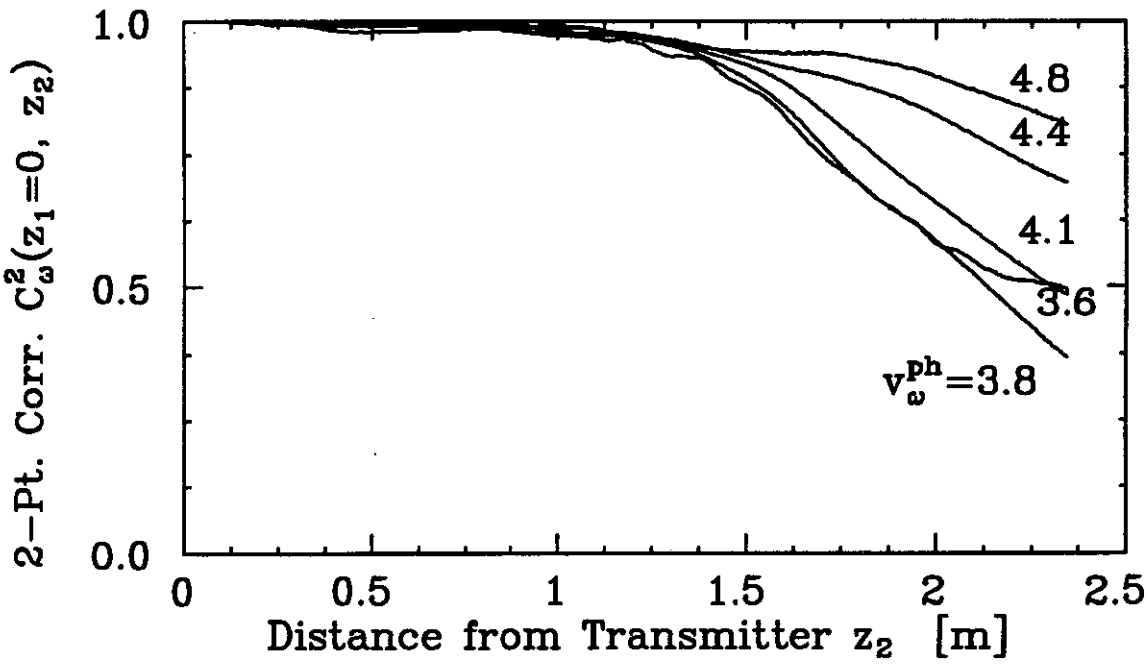

Figure 3.10: Electric field amplitude two-point correlation between a point at $z_1 = 0.1$ m (close to the launch probe) and a point at z_2 for different phase velocities v_ω^{ph} (in units of 10^6 m/s). $N = 4096, \Delta N = 80$, A=0 dB.

negligible effect on the spatial evolution of the other "main" modes. We use the superscript (m) to denote spectra which differ only in the launch amplitude of the single test mode.

The effect on the other modes can be quantified by comparing the measured spectrum $E_n^{(m)}(z)$ with $E_n^{(m')}(z)$ obtained by deleting the test mode from the launch spectrum. The quantity $\mid E_n^{(m)} - E_n^{(m')} \mid$ measures the change in the amplitudes of all the main modes between the two spectra. The first waveform (m) launches the test mode at an amplitude comparable to the adjacent main modes, whereas the second waveform (m') has the test mode set to zero. The measured difference is shown in figure 3.11 near saturation.

We observe that on average the electric field amplitude of the difference of the two spectra is about 20-35 dB below the main modes. Therefore one Fourier mode can be considered a test mode. Increasing the total number of Fourier modes

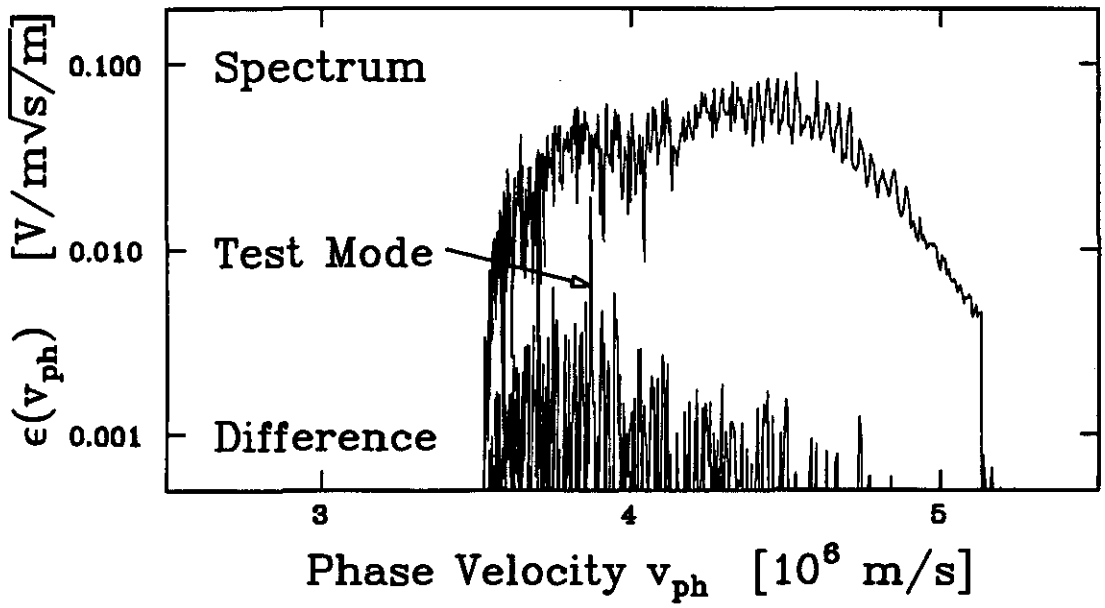

Figure 3.11: Spectral changes at saturation due to a test mode at n=200 where N/2=512. The upper curve shows the spectrum $E_n^{(m)}$, the lower curve shows the difference $\mid E_n^{(m)} - E_n^{(m')} \mid$. $N = 1024$, A =-3dB.

in the spectrum obviously increases the signal-to-noise ratio for this procedure. The observed difference is not only due to differences in the growth of the two slightly different waveforms but also differences in the launch levels of the main modes themselves that are caused by the finite bit-resolution of the arbitrary waveform generator.

We decompose the received test mode $E_n^{(m)}(z)$ into a "transmitted" component $T_n^{(m)}(z)$ which is proportional to the launch amplitude $E_n^{(m)}(0)$, and a "scattered" component $S_n^{(m)}(z)$ which is received when $E_n^{(m)}(0) = 0$. This process is illustrated in figure 3.12, where the measured complex amplitude of the test mode at saturation is shown for different initial launch waveforms. If we launch a waveform where the initial amplitude of the test mode is set to zero, we find that mode-coupling of the main modes leads to growth of the test mode. This S-component of the test mode is shown as a diamond in figure 3.12. We call this component the "scatter"

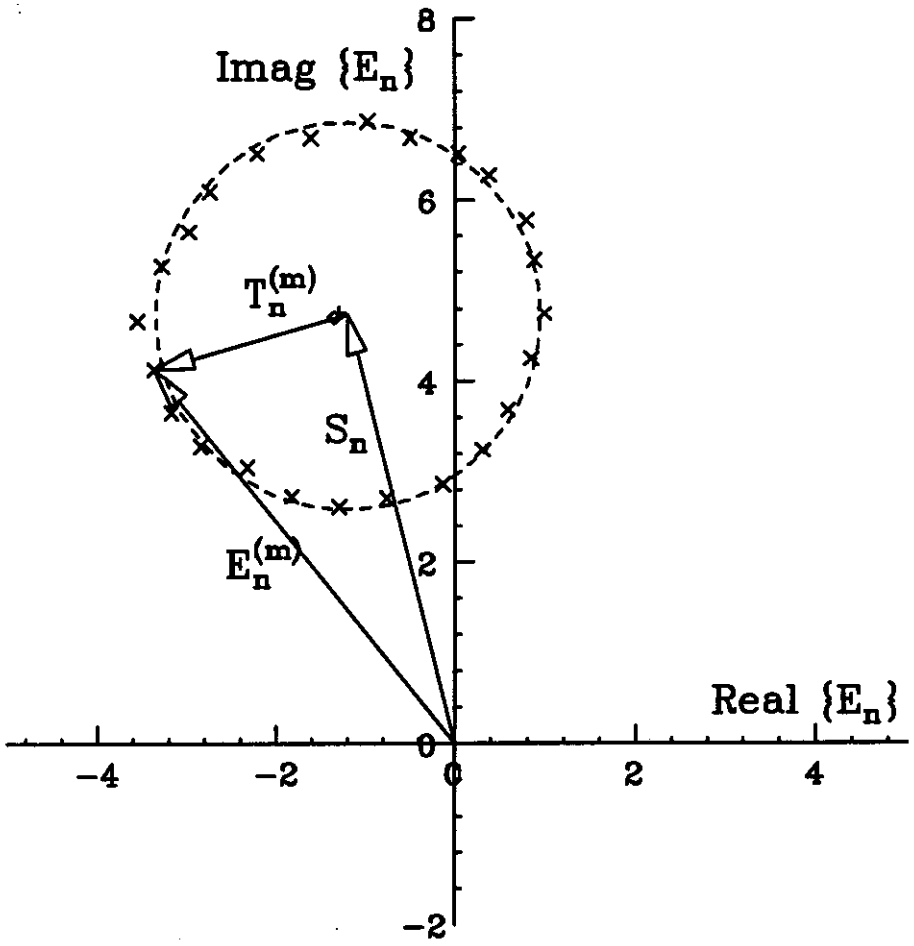

Figure 3.12: Definition of the components of a test mode at saturation. The (×) are the measured test mode phasors for varying phases of $E_n^{(m)}(0)$, the diamond (◇) is the measured phasor if $E_n^{(m)}(0) = 0$ and the cross (+) is the center of the fitted circle. The beam parameters are similar to 3.2, $n = 200$, $A = 0$ dB, $N = 1024$.

component, because it appears as if some of the power of the main modes is being scattered into the test mode. If we launch several waveforms with identical spectra except that the test mode phase is changed by $2\pi/24$ from one waveform to the next, we find that the phasor of the test mode traces out a circle in the complex plane. The center of a fitted circle (+) approximately coincides with the phasor S. Therefore at any position we can decompose the complex amplitude of the test mode, $E_n^{(m)}$, into two components: the scatter component S_n that is independent from the launch amplitude of the test mode, and a transmitted component $T_n^{(m)}$ that depends on the

launch amplitude of the test mode such that:

$$E_n^{(m)} = S_n + T_n^{(m)} \tag{3.22}$$

3.3.4 Four-Wave Coupling Model

Before we continue our discussion with the properties of the components of a test mode, we introduce a four-wave coupling model [53] in this subsection as an aid in understanding some of the experimental results. At the onset of the nonlinearities this model provides a good description; near saturation, however it breaks down because higher order terms – in our case the third order terms – become comparable to the first order terms.

The electric field amplitude E_n of a Fourier mode n can be written in form of an expansion in powers of $E_n^{(1)}$

$$E_n(z) = E_n(z)^{(1)} + E_n^{(2)}(z) + E_n^{(3)}(z) + \ldots$$

where the first order approximation $E_n^{(1)}$ is the quasilinear solution (or the RB solution)

$$E_n^{(1)}(z) = E_n(0)e^{i\int_0^z dz' k_n(z')}. \tag{3.23}$$

In this expansion the second order contribution is negligible because the beat waves have neither a helix mode nor beam electrons to resonante with [53]. The third order term is given by the following expression (for the algebra see appendix C):

$$\frac{dE_n(z)}{dz} = ik_n(z)E_n(z) + \sum_{n_1,n_2,n_3} \Gamma_{n,n_1,n_2,n_3} E_{n_1}^{(1)*}(z)E_{n_2}^{(1)}(z)E_{n_3}^{(1)}(z)\delta_{n_3,n+n_1-n_2} + O(E_n^{(4)}) \tag{3.24}$$

where the coupling term Γ is an integral of the time-averaged velocity distribution function over the occurring wave-particle resonances. $k_n(z)$ is the solution of the quasilinear dispersion relation. Reordering the expression on the r.h.s. of (3.24) by

collecting all the terms that are linear in $E_n(z)^{(1)}$ one obtains:

$$\frac{dE_n}{dz} = ik_n(1+\sum_{n_1}\Gamma_{n,n_1,n_1,n}\mid E_{n_1}^{(1)}\mid^2)E_n^{(1)} \tag{3.25}$$

$$+ ik_n \sum_{n_1,n_2,n_3}{}' \Gamma_{n,n_1,n_2,n_3}E_{n_1}^{(1)*}E_{n_2}^{(1)}E_{n_3}^{(1)}\delta_{n_3,n+n_1-n_2} + O(E_n^{(4)}) \tag{3.26}$$

$$= \frac{dT_n}{dz} + \frac{dS_n}{dz} \tag{3.27}$$

where the prime indicates that the terms with $n_1 = n$ or $n_2 = n$ are omitted and $\delta_{n,m}$ is the Kronecker symbol (requiring the frequency match of the participating modes). The mode number conventions are given in appendix B. The first summand describes the spatial change of the T_n-component of the electric field amplitude, because it is linear in $E_n(0)$. Therefore the second term describes the spatial change of the S_n-component of the electric field amplitude. When we compare our experiments with this model in the following, we approximate the primed electric fields on the r.h.s. with the actual measured fields. This approximation is probably valid until near saturation $A \approx -4$ dB.

3.3.5 Properties of the Transmitted Component

In this subsection we show that T-components of adjacent modes evolve similarly, and that their growth rates are smaller than the ensemble-averaged growth rates.

Figure 3.13a shows the evolution of the transmitted component T_n of 5 adjacent Fourier modes from the linear regime into saturation. Because the launch spectrum (shown in figure 3.2) has a smooth amplitude spectrum and the S-component vanishes in the linear regime, all the T-components initially evolve with the same amplitude. According to the four-wave coupling model, the T-components grow unaffected by the phases of the other modes, because the mode-coupling contribution to their growth as seen in equation (3.25) is not phase dependent and the coupling

coefficient T_{n,n_1,n_2} is a smooth function of the mode-numbers.

Figure 3.13b compares the growth rates at $z = 2.3$ m of the T-components with the ensemble-averaged growth rates of the entire modes E_n at different phase velocities v_ω^{ph}. We find that the growth rates of the T-component in all cases are smaller than the ensemble-averaged growth rates of the entire Fourier modes. We have not yet checked whether this agrees with the four-wave coupling model.

3.3.6 Properties of the Scatter Component

The scatter components S_n of adjacent modes evolve differently from one another, and their ensemble-averaged growth rates are approximately three times larger than the nearby-mode-averaged growth rates of the entire field E_n. This is consistent with S_n growing due to coupling with 3 other modes.

Figure 3.14a shows the evolution of the scatter component S_n of 5 adjacent Fourier modes from the linear regime into saturation. These S_n-components correspond to the T_n-components shown in figure 3.13,but have a strikingly different spatial dependence. The S_n-components are very sensitive to the phases of the amplitudes of the launched spectrum. The four-wave coupling model predicts that the scatter components are Gaussianly distributed, since each is the sum of many randomly phased contributions. We have checked the distribution of the S_n-components of nearby modes within the frequency band of a physical mode, and we find it to be Gaussianly distributed.

Figure 3.14b shows the ratio of the nearby-mode-averaged growth rate of the scatter components $\langle k_n^{iS} \rangle_{\Delta\omega}$ to the nearby-mode-averaged growth rate of the Fourier modes $\langle k_n^{iE} \rangle_{\Delta\omega}$ for two different phase velocities, as a function of the attenuation level of A of the launched spectrum. We find that the ratio of the growth rates is approximately three for launch levels smaller than $A = -4$ dB and all phase velocities. This is in agreement with the four-wave coupling model, since the growth

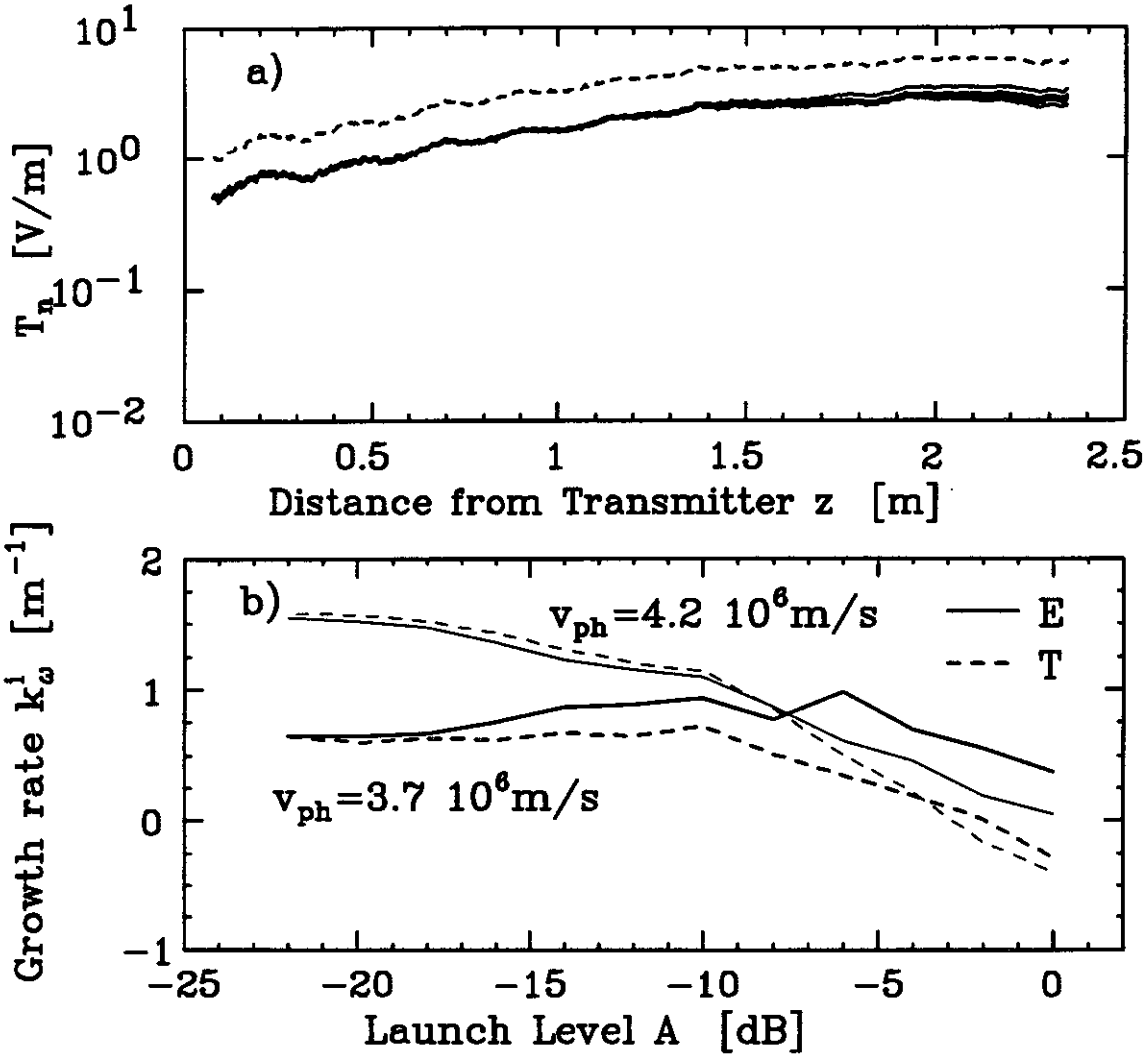

Figure 3.13: a) Spatial evolution of the T-components of modes 200-204, $A = 0$ dB, N=1024.; the spatial evolution of inbetween mode n=403 (N=2048) for case $A = 0$ dB is shown as a dashed line. b) Growth rates of the T-component (dashed) and nearby-mode-averaged E (solid) versus launch level at $z = 2.3$ m. Modes at two phase velocities are shown. The initial spectrum corresponds to figure 3.2, $\Delta N = 20, N = 1024$.

rate of the scatter component is proportional to the product of three Fourier amplitudes. We will show below that the coupling coefficient Γ_{n,n_1,n_2} insures that the largest contributions come from those products where the participating modes have approximately the same frequency. The ratio becomes greater than 3 near saturation, when $\langle k_n^{iE} \rangle$ goes to 0. This probably indicates that the 4-wave-coupling model breaks down and higher order terms need to be included.

3.3.7 Correlation Between Scatter and Transmitted Component

Close to saturation the scatter and the transmitted component are only weakly correlated within the frequency width of a physical mode, in agreement with the four-wave coupling model.

We want to correlate the ensemble-average of the Fourier mode E_n with the ensemble-averages of its scatter-component and its transmitted component. Since $E_n = T_n + S_n$ we obtain:

$$\langle \mid E_n \mid^2 \rangle_{\Delta\omega} = \langle \mid T_n \mid^2 \rangle_{\Delta\omega} + \langle \mid S_n \mid^2 \rangle_{\Delta\omega} + 2\langle Real\{S_n^* T_n\} \rangle_{\Delta\omega} \qquad (3.28)$$

Our four-wave coupling model predicts that the last term vanishes, because for each mode the scatter component and the transmitted component are uncorrelated. We measure the different terms by decomposing all the modes of the spectrum into their transmitted and their scatter component. Figure 3.15a shows $\langle \mid E_n \mid^2 \rangle_{\Delta\omega}$, $\langle \mid T_n \mid^2 \rangle_{\Delta\omega}$, $\langle \mid S_n \mid^2 \rangle_{\Delta\omega}$ and $(\langle \mid T_n \mid^2 \rangle_{\Delta\omega} + \langle \mid S_n \mid^2 \rangle_{\Delta\omega})^{1/2}$ versus phase velocity for a launch level $A = 0$ dB. We see that

$$\langle \mid E_n \mid^2 \rangle_{\Delta\omega} \approx (\langle \mid T_n \mid^2 \rangle_{\Delta\omega} + \langle \mid S_n \mid^2 \rangle_{\Delta\omega})^{1/2} \qquad (3.29)$$

and therefore concludethat the cross-term can be neglected.

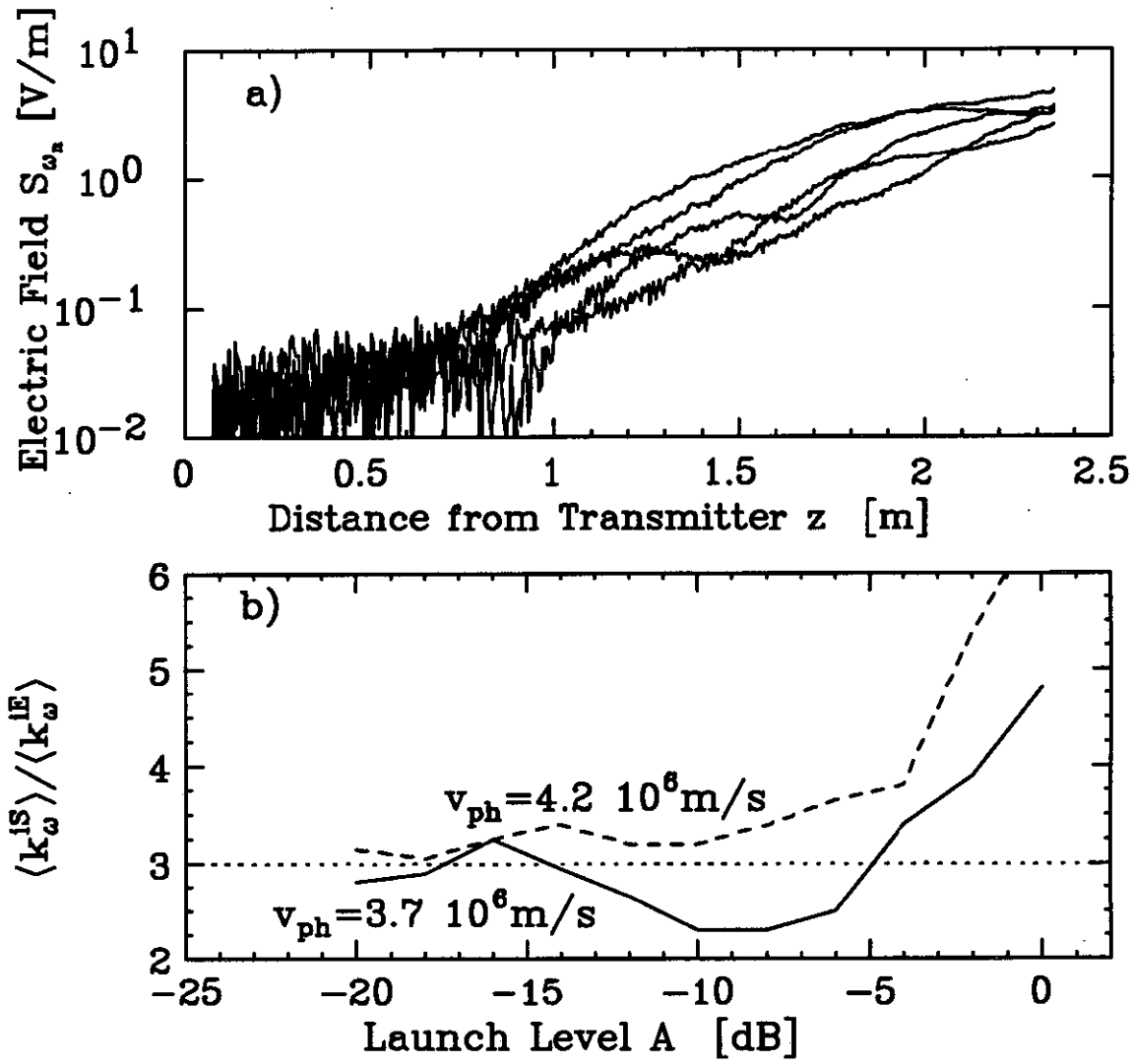

Figure 3.14: a) Spatial evolution of the S-components of modes 200-204, A =0 dB, N = 1024 (solid). b) Ratio of the ensemble-averaged growth rates of the S-component to the ensemble-averaged growth rates of the full field versus launch level A. Growth rates at two phase velocities are shown, the launched spectrum is the same as in figure 3.2.

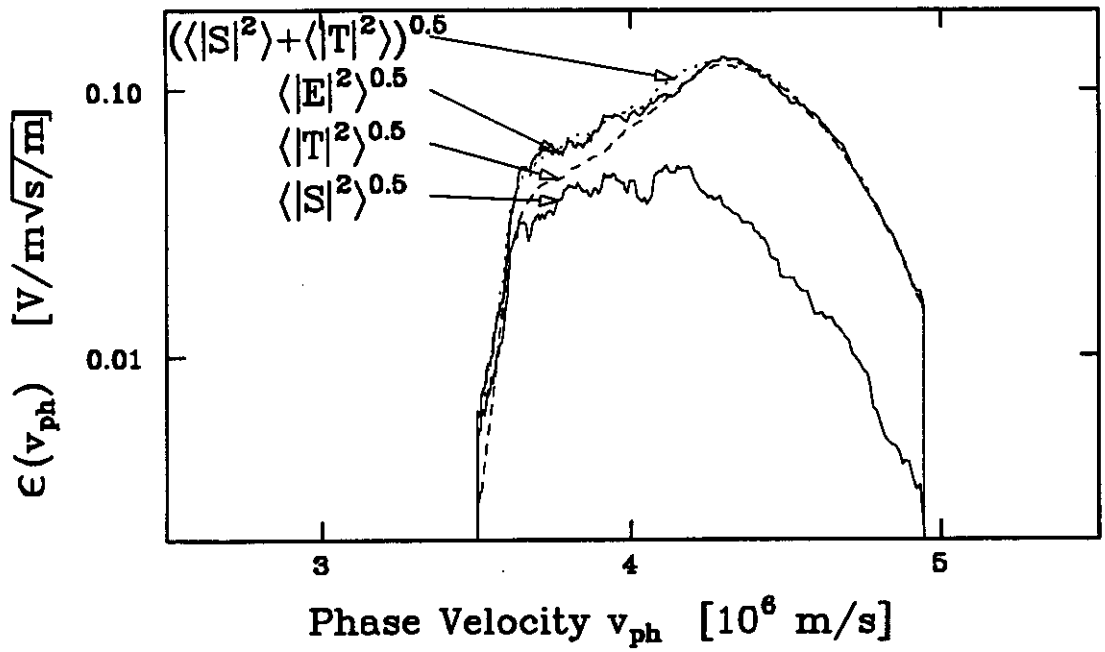

Figure 3.15: Correlation between S and T component: ensemble averaged quantities at saturation, $A = 0$ dB, $N = 1024$.

3.3.8 Frequency Range of Mode-Coupling: Scattering Out

The test mode experiments described in the previous section distinguished S from T, i.e. distinguished the power coupled **into** the test mode from the power that depended linearly on the the initial amplitude of the test mode. This section describes test mode experiments that measure the power scattered **out** of the test mode. By this technique, it is possible to measure the frequency range of the waves that participate in the mode-coupling. We find strong coupling between four waves only if their frequencies match and their wavenumbers match within an interval given by the inverse turbulent trapping length. This is in agreement with the four-wave coupling model.

In this section the launched main modes all have even mode numbers. This means that the launched waveform consists of two identical segments. The test mode that is added to the spectrum has an odd mode number. It therefore breaks the time-

translational symmetry of the waveform. Compared to the first section, the test mode is π out of phase in the second section. Again the test mode power compared to the power in the main modes is chosen small so as not to cause significant changes in the evolution of the main modes.

Mode coupling that couples two modes of the launched spectrum creates waves at their sum and difference frequencies. For most possible combinations, these frequencies lie outside of the initial spectrum and outside of the range of resonant beam electrons. Close to saturation we do observe wave growth outside of the launched spectrum. We estimate the total power of these waves to be much smaller than the power in the launched spectrum. Therefore two wave coupling can probably be neglected.

Mode coupling that couples three modes of the launched spectrum can create waves that are within the unstable spectrum, and can therefore modify the further evolution of the instability. If one of the three participating modes is the odd-numbered test mode, then also the resulting non-linear product will have an odd mode number. However, since only the test mode has an odd mode number in the launched spectrum, these nonlinear product waves occur in the spectrum as growing odd-numbered modes.

Scattering into the test mode is not possible from the main modes alone, but needs to involve one of the odd-numbered modes that were created in the nonlinear region. This is a small second-order effect. We find that the spatial evolution of the launched inbetween test mode is identical to the evolution of the T-components of an adjacent main mode. The dashed line in figure 3.13 shows the evolution of an inbetween test mode in comparison with the evolution of the T-components. The inbetween test mode was launched at twice the amplitude of the main modes. This is in agreement with the four wave coupling model that predicts the scatter term to

be zero for the inbetween test mode.

The measured spectrum at the end of the interaction region is shown in figure 3.16a. There the spectral density is displayed separately for the main modes (even-numbered) and the nonlinear product modes (odd-numbered). It is apparent that the product modes at mode-numbers closest to the inbetween test mode have grown more than the product modes of the rest of the spectrum. Because of the finite bit resolution of the waveform generator and nonlinearities in the launch circuit not only the inbetween test mode, but all odd-number modes are launched. All of them are growing similar to the main modes. This growth is superposed with the growth of the nonlinear product modes, generated by the coupling of the test inbetween mode with the main modes. We separate the two contributions by comparing the ensemble-averaged growth rates of the even-numbered modes and the odd-numbered modes. These ensemble-averaged growth rates are shown in figure 3.16b. For phase velocities larger than 4.2×10^6 m/s the ensemble-averaged growth rates of the even and the odd modes are approximately the same; for phase velocities smaller than 4.2×10^6 m/s the odd-numbered modes grow faster than the even-numbered modes by about a factor of 3. In this range the coupling between the test inbetween mode and the main modes is especially strong. We define a resonance range with the lower and upper limit, v_l^{res}, v_u^{res} respectively, as the range where the ensemble-averaged growth rate of the odd-number modes is at least 2 times larger than the ensemble-averaged growth rate of the even-numbered modes. In the following we show the measured ranges for inbetween test modes at different frequencies and different launch levels of the spectrum.

In theoretical investigations of weak turbulence, it typically is assumed that modes couple to one another effectively only if the frequencies of the participating waves match exactly and the wavenumbers are matched within an uncertainty given

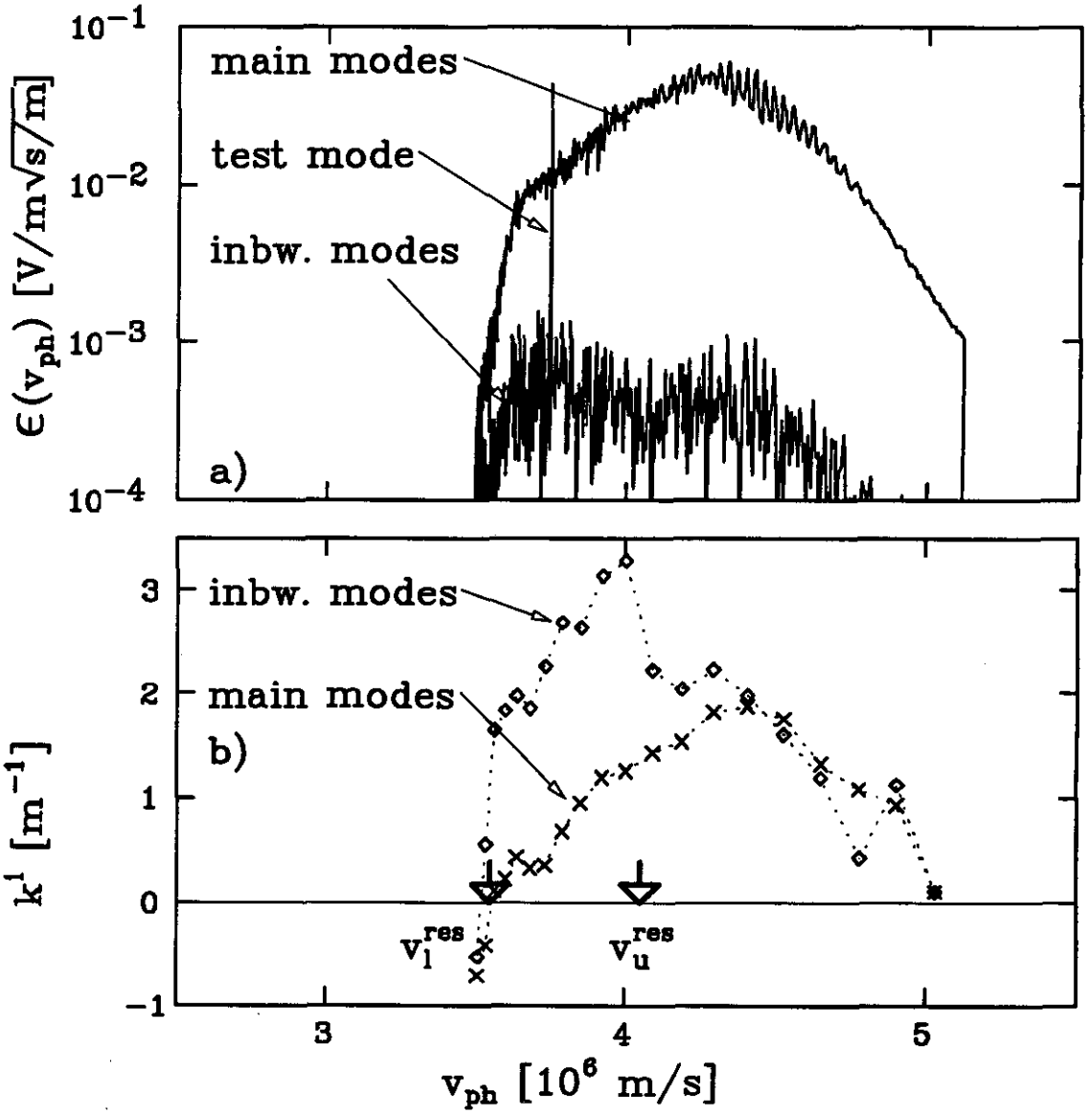

Figure 3.16: a) Spectrum at the end of the machine if an inbetween test mode was added to the spectrum. The shape of the spectral density of the launch spectrum is the same as in figure 3.2, $A = -18$ dB, $N = 2048, n_{inbw} = 353$. b)Ensemble-averaged growth rates of the main modes and the nonlinear product modes ("inbw."). The arrows mark the experimental limits of the resonance region v_l^{res}, v_u^{res}

by the maximum of the inverse turbulent trapping length and the growth rate [52, 53]. For launch amplitudes where we observe strong mode coupling at the end of the interaction region, the inverse trapping length is larger than the growth rate. For the TWT these requirements become[2]:

$$\omega_{n_1} + \omega_{n_2} - \omega_{n_3} - \omega_{n_4} = 0, \tag{3.30}$$

$$\mid k^r_{n_1} + k^r_{n_2} - k^r_{n_3} - k^r_{n_4} \mid \lesssim \mathrm{Max}\{l^{-1}_{tt}, k^i_n\}. \tag{3.31}$$

Physically these requirements state the following. The nonlinear product of three waves with frequencies $\omega_{n_1}, \omega_{n_2}$ and ω_{n_3} travels at a phase velocity given by $(\omega_{n_1} + \omega_{n_2} - \omega_{n_3})/(k_{n_1} + k_{n_2} - k_{n_3})$. It couples most strongly to electrons resonant within the wave-particle resonance whose width is given by the maximum of wave growth rate and inverse turbulent trapping length. Waves resonant with the electrons will "notice" the changes in the electron orbits caused by the nonlinear product and therefore become coupled to the three waves.

In order to compare this model with our experiment we make the following additional assumptions. We assume that the mode n_1 is the test inbetween mode and n_2 is the nonlinear product mode. In addition, we assume that the two main modes have approximately the same frequency $\omega_{n_3} \approx \omega_{n_4}$. Then if $\omega_{n_2} = \omega_{n_1} \pm \Delta\omega_{res}$, we have

$$\omega_{n_3} \approx \omega_{n_4} \approx \omega_{n_1} \pm \Delta\omega_{res}/2 \tag{3.32}$$

$$\mid k^r_{n_1} + k^r_{n_2} - 2k^r_{n_3} \mid = \mathrm{Max}\{l^{-1}_{tt}, k^i_n\}. \tag{3.33}$$

Notice, that the l.h.s. of equation (3.33) depends only on $\Delta\omega_{res}$, because of equation (3.31). The deviation of the wavenumber k^r_n from the wavenumber of the beamless helix are not negligible as was seen in section 2.3.2. Since we cannot measure them when mode-coupling has set in, we use the solutions of the QL dispersion relation

[2]Other combinations are not possible within the frequency range of the launched spectrum

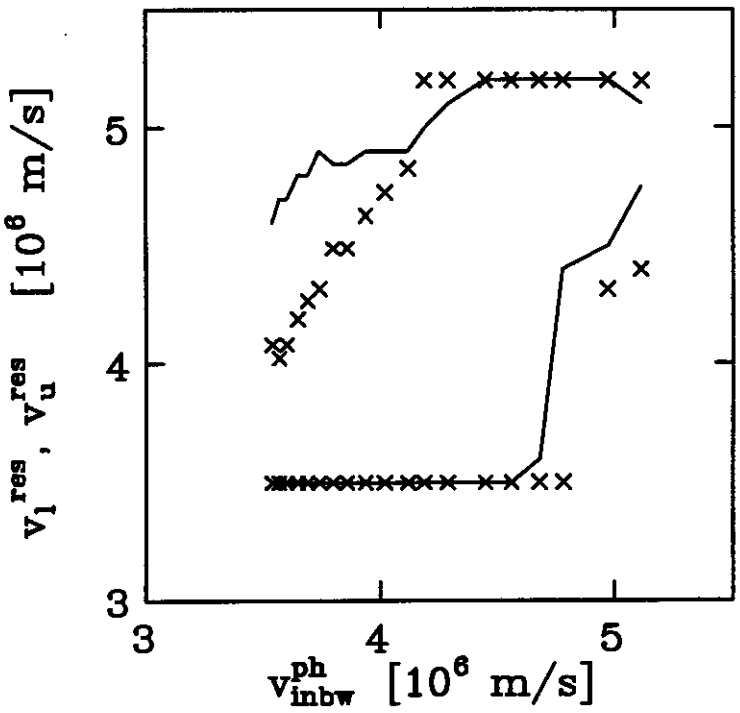

Figure 3.17: Experimentally measured upper and lower phase velocities v_u^{res}, v_l^{res} ($\times$) of the mode-coupling resonance for different phase velocities of the inbetween test mode. Solution of (3.33) shown as line, $A = -8$ dB.

as an approximation. We then solve equation (3.33) graphically in order to obtain $\Delta\omega_{res}$.

Figure 3.17 compares the experimentally determined limits v_l^{res} and v_u^{res} of the mode-coupling resonance with the predictions of equation (3.33) for inbetween modes at different phase velocities. The model predicts coupling ranges wider than experimentally observed. This could be due to the crudeness of the model or to a systematic error of the experiment where the resonance region is truncated too small because the nonlinear product waves have not outgrown the launch contributions. The flat regions on the top and the bottom are because both, experimental data and the predictions of the model, are truncated at the edges of the launched spectrum. At the low velocity end this is justified since the helix dispersion (in lowest order) does not propagate waves with phase velocities lower than $\approx 3.5 \times 10^6$ m/s. At

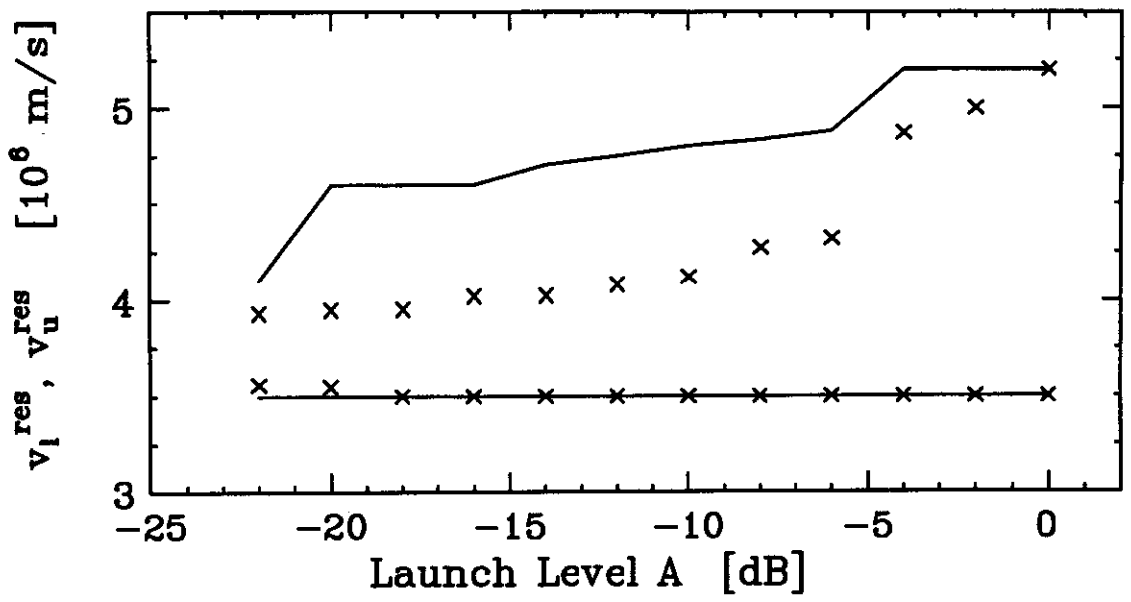

Figure 3.18: Experimentally measured upper and lower phase velocities v_u^{res}, v_l^{res} (×) of the mode-coupling resonance for launch amplitudes of the spectrum (×). The launch spectrum has the same shape as in figure 3.2, $N = 2048, n_{inbw} = 353$, $v_{inbw}^{ph} = 3.75 \times 10^6$ m/s.

high phase velocities we cannot measure wave coupling outside the launched range of waves.

Figure 3.18 compares the experimentally determined limits v_l^{res} and v_u^{res} of the mode-coupling resonance with the predictions of equation (3.33) for one inbetween mode at different launch levels. Again the model predicts coupling ranges wider than experimentally observed. At low phase velocities, coupling between waves is always over a wide range regardless how small the turbulent trapping length because all waves have approximately the same group velocity. We believe this to be the reason why mode coupling is stronger at low than at high phase velocities.

3.3.9 Tri-spectra measurements

Mode-coupling as defined and described in the previous sections leads to strong deviations of the phases of the modes in the nonlinear regime because the

scatter component is unrelated to the transmitted component. The inbetween mode measurements of the preceeding section indicated that this mode-coupling is localized around the inbetween test mode. This section confirms this assertion by showing the results of a "tri-spectral" analysis, that is a statistical means of quantifying the phase-coherence of four waves.

In recent years, bispectral analysis has become an often used tool for describing nonlinear wave coupling in fusion plasmas [32, 31, 49]. The underlying assumption for using the approach is that the relevant wave processes can be described by a nonlinear wave coupling equation. Bispectral analysis measures nonlinear phase coherences in order to statistically determine how strong two waves are coupled to produce a third wave.

For our situation we need to invoke an extension to four waves, hence we will embark on a tri-spectral analysis. We want to determine the coupling between all the modes and the scatter component of one particular mode. Since we still have perfect control over the evolution of the instability we launch waveforms with equal electric field densities (amplitudes), but random phases. By setting the launch amplitude of the mode of interest equal to zero, we only measure its scatter component in the nonlinear regime. We use the tri-spectral analysis to determine the correlation between the phase of this scatter component and the phase of three waves of frequencies such that equation (3.30) is fulfilled.

First we need to define a quantity γ_{n,n_1,n_2} that statistically describes the goodness of the following expression

$$S_n - \gamma_{n,n_1,n_2} E^*_{n_1} E_{n_2} E_{n+n_1-n_2} = 0 \tag{3.34}$$

Proceeding as in the section of the two-point correlation function, we ensemble average the squared magnitude over initial phases which is denoted by pointed brackets

$\langle\rangle$ (N=64).

$$\langle \mid S_n - \gamma_{n,n_1,n_2} E^*_{n_1} E_{n_2} E_{n+n_1-n_2} \mid \rangle = 0 \tag{3.35}$$

Separating the summands and approximating the occurring cross-term we find:

$$\langle \mid S_n \mid^2 \rangle + \mid \gamma_{n,n_1,n_2} \mid^2 \langle \mid E^*_{n_1} E_{n_2} E_{n+n_1-n_2} \mid^2 \rangle - 2 \mid \gamma_{n,n_1,n_2} \mid\mid \langle S^*_n E^*_{n_1} E_{n_2} E_{n+n_1-n_2} \rangle \mid \geq 0 \tag{3.36}$$

Solving for $\mid \gamma_{n,n_1,n_2} \mid$ one finds positive definite solutions only if

$$\gamma^2_{n,n_1,n_2} \equiv \frac{\mid \langle S^*_n E^*_{n_1} E_{n_2} E_{n+n_1-n_2} \rangle \mid^2}{\langle \mid E^*_{n_1} E_{n_2} E_{n+n_1-n_2} \mid^2 \rangle \langle \mid S_n \mid^2 \rangle} \leq 1 \tag{3.37}$$

γ^2_{n,n_1,n_2} equals unity if there is perfect correlation between S_n and the electric field amplitudes $E^*_{n_1}$, E_{n_2}, $E_{n+n_1-n_2}$, i.e. if the scatter component is only excited by coupling of the waves with mode numbers n_1, n_2 and $n + n_1 - n_2$. Because it is positive definite it is bounded by zero for no correlation. We call γ^2_{n,n_1,n_2} the "trispectral correlation parameter".

Since the calculation of the trispectral correlation parameter is very time and memory intensive, we use short waveforms with $N = 64$ and typically launch 1000 waveforms with different phases but the same amplitudes for calculating the ensemble-averages.

Figure 3.19 shows the trispectral correlation coefficient γ. The phase velocity of the mode of interest is $v^{ph}_S = 3.65 \times 10^6$ m/s. Figure 3.19a shows the phase velocity dependence of the case when one of the participating modes has a phase velocity of 4.6×10^6 m/s. Then the phase velocity of the third mode is scanned across the spectrum and the phase velocity (frequency) of the forth mode is determined from equation (3.30). Figure 3.19b shows the same plot for the phase velocity of one of the modes fixed at 3.85×10^6 m/s. We see that much stronger coupling occurs in this case than in the previous one. This is in qualitative agreement with the inbetween mode measurements, where strongest coupling also occurs in a regime around the inbetween test mode.

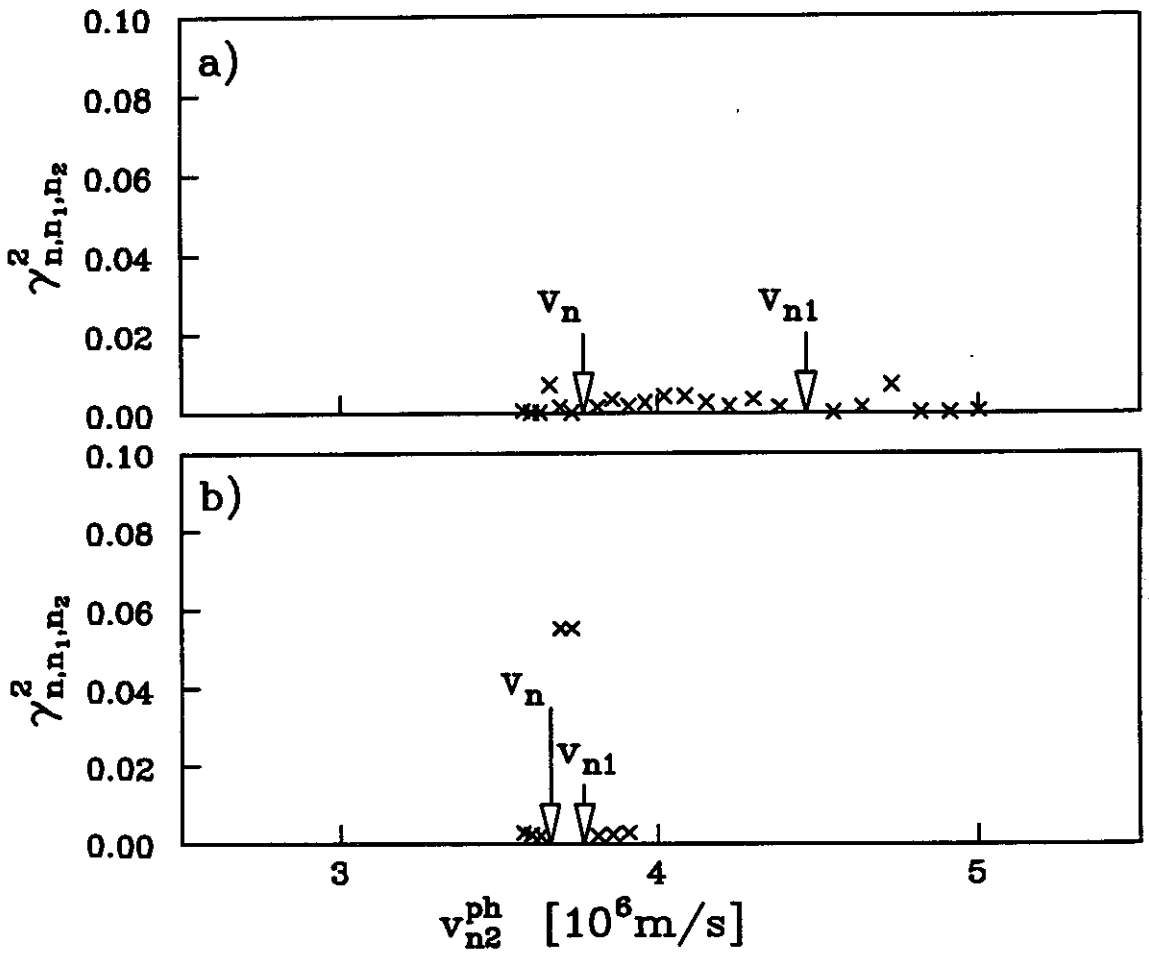

Figure 3.19: Trispectral correlation: a) $v^{ph}_{n_1} = 4.6 \times 10^6$ m/s, b) $v^{ph}_{n_1} = 3.85 \times 10^6$ m/s, $N = 64$, $A = -16$ dB, the launch spectrum and the beam are is similar to figure 3.2.

3.4 Kurtosis

In this section we investigate the evolution of the electric field not in Fourier space but in real time. We describe the probability distribution of the electric field by its kurtosis. Close to saturation the kurtosis suggests a transition to frequency modulation. This is not predicted by the four-wave coupling model.

Kurtosis K is the fourth moment of a statistically distributed quantity. In the following K is normalized such that its value is zero if the considered quantity is distributed according to a Gaussian distribution. It is defined as

$$K(z) \equiv \frac{\sum_{i=1}^{N_W} E^4(z,t_i)}{N_W \sigma_E^4(z)} - 3 \tag{3.38}$$

where the rms amplitude is given by

$$\sigma_E(z)^2 \equiv \frac{1}{N_W} \sum_{i=1}^{N_W} E^2(z,t_i) \tag{3.39}$$

and the t_i are the N_W sampling times equally distributed over the period T of the waveform. The mean of E is zero, since there is no dc component to the spectra. In our calculation, N_W is larger by a factor of 4 than the number of wavepoints N generated by the arbitrary function generator since the homodyning process increased the highest frequency of the waveform. One can show that for a waveform with a broad, dense randomly-phased spectrum, the waveform is Gaussianly distributed and the kurtosis is zero.

Figure 3.20a shows the electric field probability distribution near the launch position and near saturation. A fitted Gaussian is shown in comparison. Figure 3.20b shows the spatial evolution of the kurtosis for different launch levels. The initial value of the kurtosis close to zero reflects the good fit of the Gaussian to the initial distribution. The kurtosis is not exactly zero but still within the range of statistical jitter. Near saturation, the probability distribution has shorter tails than

the Gaussian and correspondingly the kurtosis becomes negative. The kurtosis for $A = -22$ dB changes little over the length of the helix. For this case the instability is still in the linear regime at the end of the interaction region. In contrast, the kurtosis reaches $K = -0.6$ for saturation for the case $A = 0$ dB. This change in the kurtosis is not due to the narrowing of the bandwidth, since the final spectra are all of similar width. Rather the negative kurtosis is due to a phase coherence developing between the Fourier modes of the spectrum. Randomly changing the phases of the measured spectrum (but keeping the amplitudes constant) changes the computed kurtosis again to values between -0.2 and 0.2.

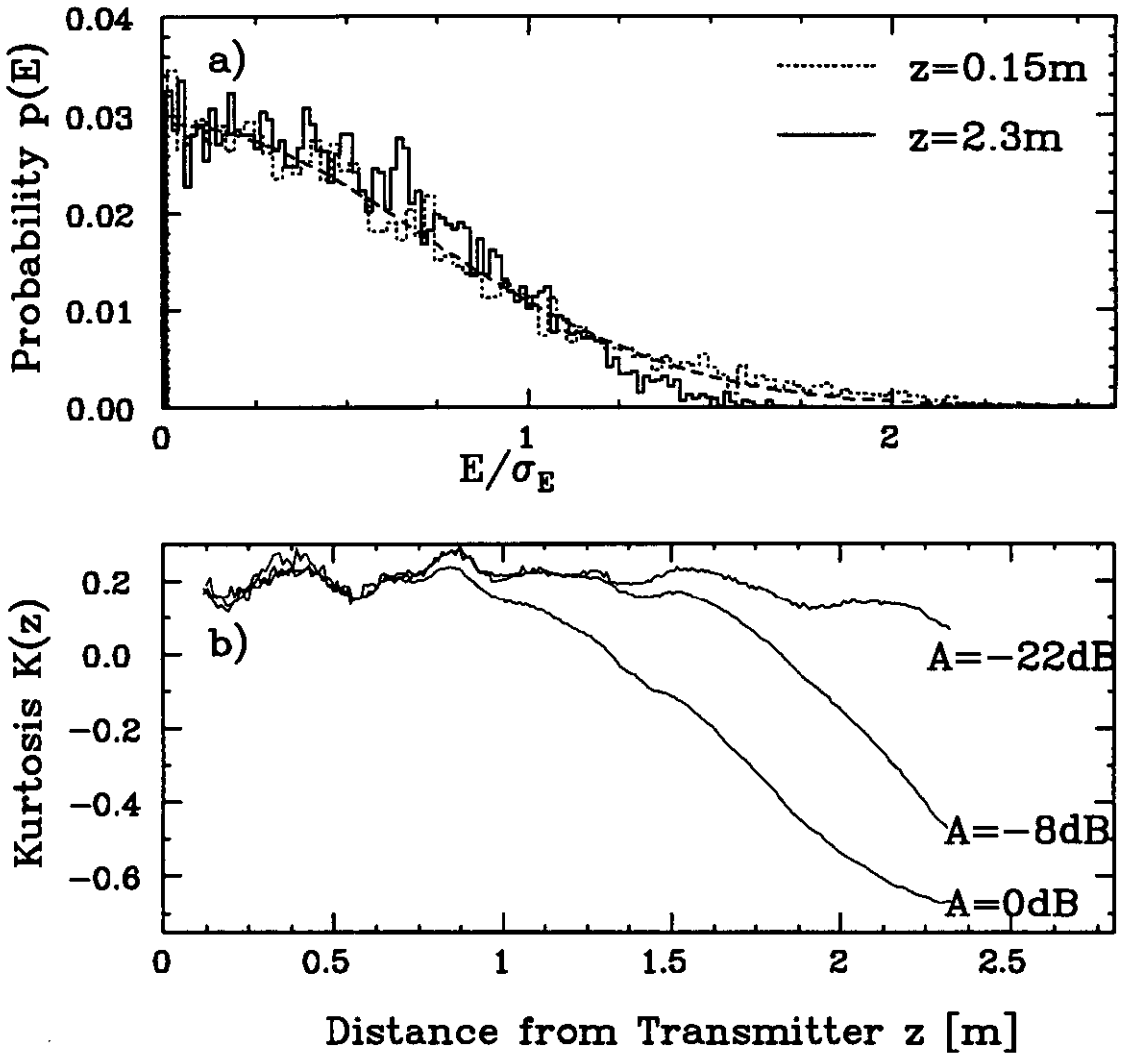

Figure 3.20: a) Probability distribution of electric field amplitudes $E(z,t)$ at $z = 0.15$m (dotted) and $z = 2.3$m (solid); fitted Gaussian (dashed); $N = 1024, A = 0$ dB. b) Spatial evolution of the kurtosis for three different launch levels A.

3.5 Measurements of Growth Rates

In this section we compare the measured ensemble-averaged growth rates near the end of the interaction region with the growth rates calculated from the dispersion relations of quasilinear theory and resonance-broadening theory. By changing the launch level of the spectrum, we change the level of nonlinearities at the end of the interaction region. We find that in the center of the spectrum, the measured growth rates in the nonlinear regime are larger than the calculated growth rates. The discrepancy seems to be larger than what can be accounted for with systematic measurement errors.

The ensemble-averaged growth rates $k_n^i(z)$ are obtained by fitting a straight line to the frequency-averaged mode amplitudes, as displayed in figure 3.21. Typically we divide the total spectrum into 20 "physical" frequency bins, and average the square of the Fourier modes, obtaining $<\mid E_n \mid^2>_{\Delta\omega}$ from equation (3.13). We then fit a straight line to the spatial evolution of this averaged electric field amplitude in the last 0.20 m before the end of the interaction region using the least-squares-method. Since the growth rates might be changing even over this distance, this measurement approach is prone to yield growth rates that are too high. We estimate this effect to be maximal $0.2\mathrm{m}^{-1}$. Because of strong local irregularities of the helix and high damping rates the growth rates at low phase velocities have the largest errors bars. The modulations are caused by the sharp fall-off of the beam distribution at its high velocity end that leads to incomplete phase-mixing at these distances from the transmitter. It is analyzed in more detail in appendix D.

We measure the corresponding velocity distribution as described before in section 2.2. Even in the nonlinear regime, the measured velocity distribution is essentially homogeneous across the cross-section of the beam, with slightly increased diffusion (flattening) near the beam edges. The solution of the quasilinear dispersion

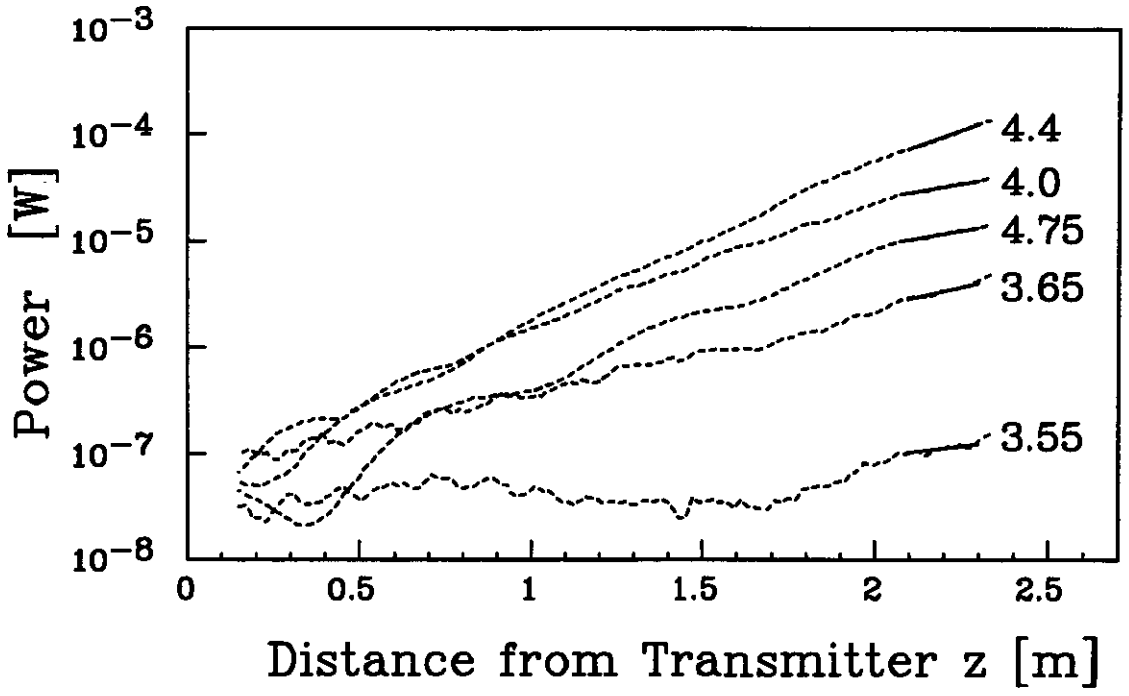

Figure 3.21: Total power in a frequency band of ΔN modes versus distance for different phase velocities (in units of 10^6 m/s)(dashed). Straight line fit between 2.1 and 2.3 m (solid). $A = -8$ dB, $N = 1024, \Delta N = 21$.

relation (B.16) is then straightforward. For the resonance-broadening dispersion relation (B.32), it is necessary to first calculate the turbulent trapping lengths, l_{tt}, versus phase velocity of the waves for which a solution is desired. l_{tt} is self-consistently obtained from (B.34) with the space-charge contribution H_q as calculated from the quasilinear dispersion relation.

In figure 3.22 we compare the ensemble-averaged growth rates with the calculated growth rates of quasilinear theory and resonance-broadening theory for various launch levels A. In figure 3.22a the spectrum of figure 3.2 is launched with $A = -22$ dB. The measured velocity distribution function is hardly distinguishable from the case where no waves are launched, shown in figure 3.3 (dashed). The solutions of the dispersion relation of QL theory and RB theory are almost the same because $k^i \times l_{tt} \gg 1$. The measured growth rates agree well with the predictions except for very low and for very high phase velocities: at low phase velocities ($v^{ph} \lesssim 3.65 \times 10^6$

m/s) the irregularities of the helix require fits over longer distances, at high phase velocities ($v^{ph} \gtrsim 4.85 \times 10^6$ m/s) the linear wave growth is obscured by the incomplete phase mixing.

In figure 3.22b the spectrum of figure 3.2 is launched with $A = -8$ dB. The measured velocity distribution is shown in figure 3.27a. The growing solutions of the dispersion relations of QL theory and RB theory are slightly different. At high phase velocities where the space-charge term H_q becomes large, the calculated turbulent trapping length l_{tt} is likely to be too small which in turn causes the growth rates to be too small also (see section 3.6.2). "Eyeball-Averaging" over the jitter at low phase velocities one might deduce that the measured and the calculated QL growth rates still agree with one another at low and at high frequency. In the central range of phase velocities, the measurements agree better with the prediction of RB theory than with QL theory. In this range, however, the steepness of the velocity distribution renders the phase-mixing assumption in the standard derivation of the quasilinear equations not applicable. Appendix D attempts to calculate the growth rates when the phase-mixing assumption is not made. The results for QL theory and RB theory are shown as thin lines. In both cases this leads to an increase in the predicted growth rates, such that the experimental growth rates agree reasonably with the predictions of the modified RB theory.

In figure 3.22c the spectrum of figure 3.2 is launched with $A = 0$ dB. The measured velocity is shown in figure 3.3 (solid). The growing solutions of the dispersion relations of QL theory and RB theory are slightly different. Overall the experimental growth rates agree reasonably with the predictions of RB theory, and slightly worse with QL theory. Since the diffusion has washed out the high velocity falloff of the beam distribution, the phase-mixing assumption is justified.

In figure 3.23a-c we compare the measured final growth rates for various

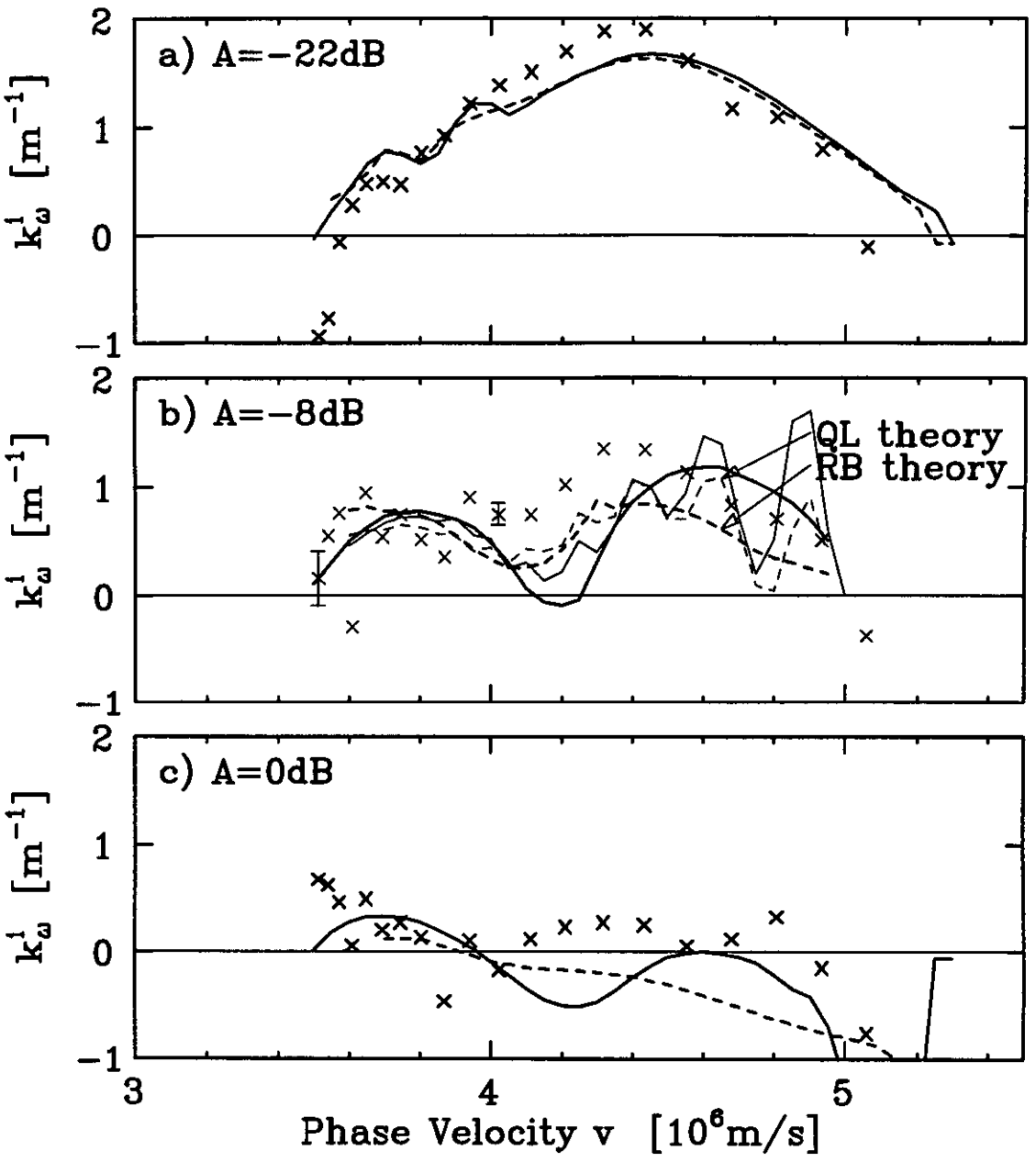

Figure 3.22: Comparison of the measured growth rates (×), growing solution of QL theory (thick solid line), growing solution of RB theory (thick dashed line), $N = 1024$, $\Delta N = 21$. a) $A = -22$ dB; b) $A = -8$ dB, QL theory for incomplete phase mixing (thin solid line), RB theory for incomplete phase mixing (thin dashed line); c) $A = 0$ dB.

launch levels A with the predictions of QL theory and RB theory. We find that the agreement between the measured and the calculated growth rates is good for quasilinear theory except in the region of intermediate phase velocities. The agreement with resonance-broadening theory is good except in the region of large phase velocities. For high phase velocities, however, RB might yield too low growth rates because of too small values of l_{tt}. In figure 3.23d we show the products of growth rates and turbulent trapping lengths, $k_n^i \times l_{tt}$, for the three phase velocities of figures 3.23a-c. If the product is larger than ≈ 1, then QL theory and RB theory yield the same results. If the product is smaller than ≈ 1, then it depends on the shape of the distribution function whether the predictions of QL theory and RB theory agree with one another or not.

The ensemble-averaged growth rates is the key-calculation of many theories that are trying to describe the weak warm beam instability. The question that all the theories want to answer is whether mode coupling leads to zero order modifications. Therefore there is considerable interest in experimental measurements. As we have shown, our measurements are hampered by a number of caveats that influence the growth rate predictions. We are also by no means certain, that we have uncovered all systematic errors associated with measuring the velocity distribution. However, we tend to conclude from our experimental data, that mode-coupling induced growth rate enhancement can only be possible close to saturation where the velocity distribution has changed and is likely to be small.

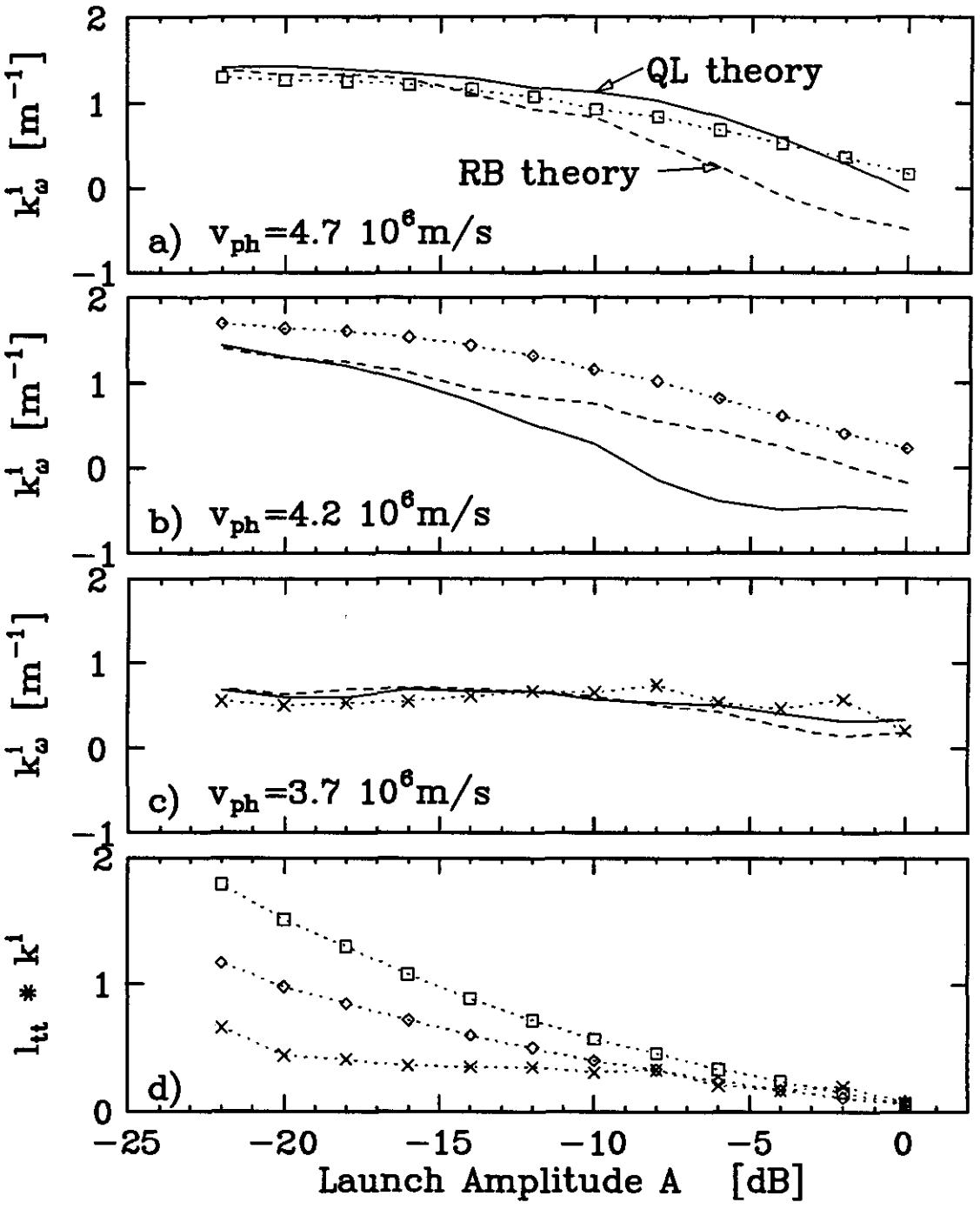

Figure 3.23: a) Comparison of Measured Growth Rates with QL and RB theory versus the launch level of the spectrum A for different phase velocities. b)Product of $k^i_{\omega_n} \times l_{tt}$ for above cases.

3.6 Measurements of Diffusion

In this section we measure two cases of the evolution of the beam velocity distribution, and compare it with calculations based on quasilinear theory and resonance-broadening theory. In the first case, we launch a broad spectrum of waves and a weak cold electron beam. The electron beam diffuses under the influence of the electric fields, but is too weak to react back on them. We calculate the diffusion coefficient from the spreading of the beam distribution, and find it to agree well with calculations based on quasilinear theory. The results of resonance-broadening theory are similar to the results of quasilinear theory, because $l_{tt}^{-1} \lesssim \mid k_{\omega}^{0i} \mid$.

In the second case we launch a stronger, warm beam, and measure the changes in the beam distribution during wave growth. We find that the measured beam velocity distribution at the end of the interaction region agrees only qualitatively with the calculated distribution based on quasilinear theory and resonance broadening theory. The difference between the predicted velocity distributions of QL theory and RB theory are small. Some of the disagreement between theory and experiment may be due to systematic errors in calculating the diffusion coefficient.

3.6.1 Linear Diffusion

In this section a small cold test electron beam is used to measure the velocity diffusion caused by a launched broad spectrum of many randomly phased waves. We find good agreement between the measured diffusion coefficient and the quasilinear prediction for a wide range of electric field amplitudes and overlap parameter. In all cases the total wave power is much larger than the beam kinetic power, so that the back reaction of the test beam on the waves is small.

The dashed line in figure 3.24 shows the measured velocity distribution of the cold test beam when no waves are launched. The beam current in this case is

only about 0.1% of the current used in the weak warm beam instability. When a broad spectrum of waves with random phases is launched, the measured velocity distribution function changes. The shape of the launched spectrum of waves is very similar to the spectrum shown in figure 3.2 with $N = 1024$. The solid lines show the measured velocity distribution for different launch levels A.

In all the cases, the measured beam distributions are well approximated by Gaussians, i.e. $e^{-(v-v_0)^2/(v_\sigma)^2}$. Best-fit Gaussians are shown in figure 3.24 as dotted lines and these fit the experimental distributions well. We use the mean v_0 and the width v_σ of the fitted Gaussian to completely characterize the normalized velocity distribution function. We denote the initial width of the beam by v_σ^0; it is the measured width when no waves are launched.

Figure 3.25 shows the change of the width of the test beam Δv_σ

$$\Delta v_\sigma \equiv \sqrt{v_\sigma^2 - (v_\sigma^0)^2}$$

as a function of the launch level A of the wave spectrum for different beam velocities. The change in v_σ is proportional to the electric field strength, as can be seen by comparing the data points with the dashed line. Changing the launch amplitude of the spectrum changes the overlapp parameter [11]. In all cases, however, the overlapp parameter is greater than 50 where computer simulations predict the validity of quasilinear theory.

We calculate a diffusion coefficient from the measured warming of the beam by solving the diffusion equation (B.18). The diffusion coefficient $D(v, z)$ is approximately proportional to the square of the electric field of the wave with phase velocity $v_{ph} = v$. Because the electric field is being damped by the lossy slow wave structure the diffusion coefficient can therefore be written as

$$D(v, z) = D_0(v)e^{-2*|k_\omega^{0i}|z} \tag{3.40}$$

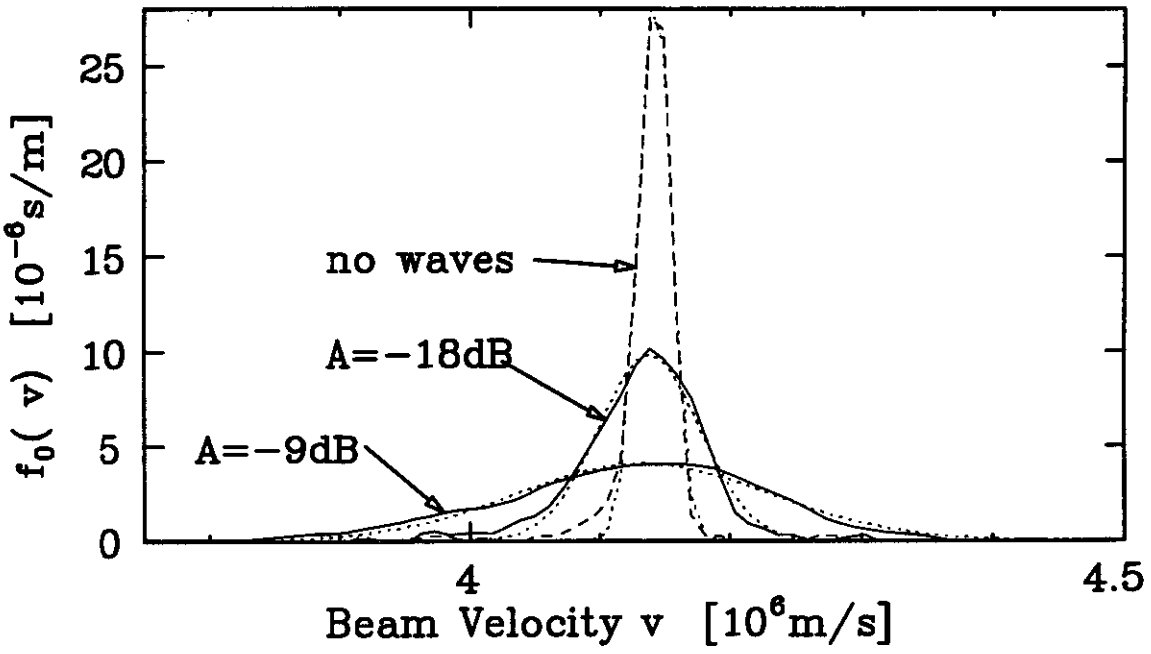

Figure 3.24: Measured velocity distribution of an initially cold beam for different launch levels A of a broad spectrum similar to 3.2 (solid). Initial cold beam distribution if no waves are launched (dashed); Gaussian least square fits (dotted). (N=1024).

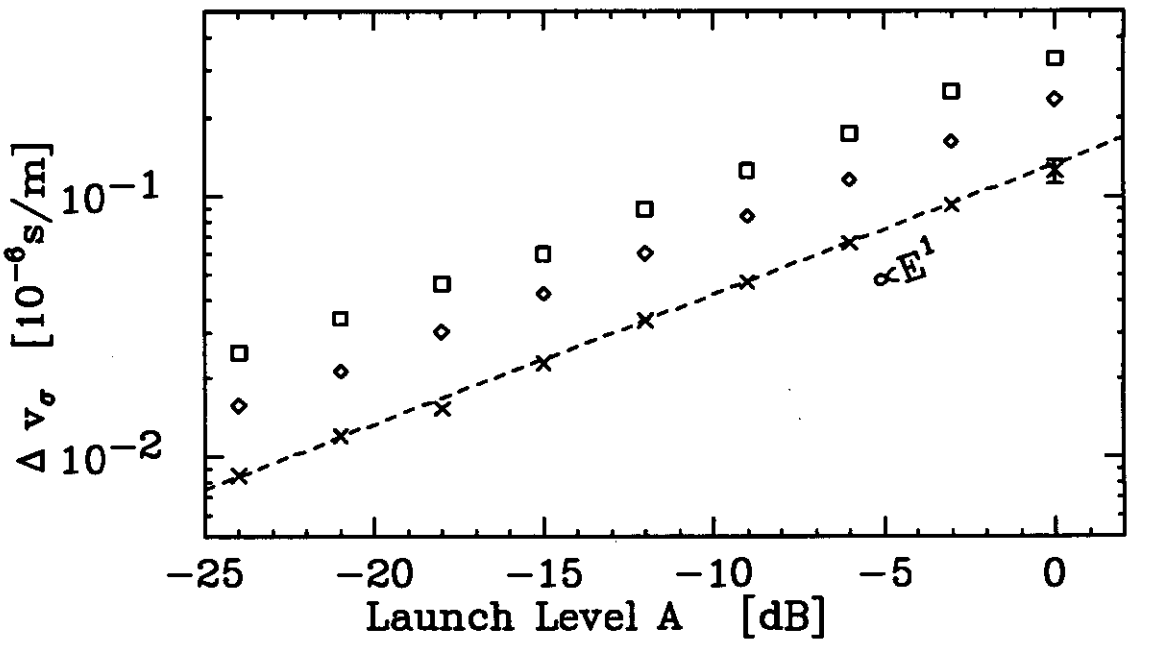

Figure 3.25: Measured test beam diffusion for launch levels A. V_c = 75V (×),V_c = 65V (◇), V_c = 55V (□). Dashed lines shows dependence predicted by QL theory.

where k_ω^{0i} is the damping rate of the wave with phase velocity $v_{ph} = v$ and $D_0(v)$ is the diffusion coefficient at $z = 0$. Using a Gaussian (centered at v_0 and with width v_σ^0) as the initial velocity distribution, the solution of the quasilinear diffusion equation becomes:

$$f_0(v,z) = \frac{1}{\sqrt{\pi v_\sigma^2(z)}} e^{-(v-v_0)^2/(v_\sigma^2(z)} \tag{3.41}$$

where the width of the electron beam $v_\sigma(z)$ is given by

$$v_\sigma^2(z) = (v_\sigma^0)^2 + \frac{2D_0(v)}{v_0 \mid k_\omega^{0i} \mid}(1 - e^{-2*|k_\omega^{0i}|z}). \tag{3.42}$$

Setting $z = L$ to be the distance from the transmitter to the end of the helix and using the measured v_σ^0 and $v_\sigma(L)$, we obtain the diffusion coefficient $D_0(v)$ at the launch position of the spectrum.

From quasilinear theory we calculate the diffusion coefficient according to equation (B.13) (where we have neglected the space-charge term):

$$\begin{aligned} D^{ql}(v,z) = & \frac{e^2}{m^2} \sum_n \mid E_n(z) \mid^2 \frac{v k_n^{0i}}{(\omega_n - v k_n^{0r})^2 + (v k_n^{0i})^2} \\ + & \ 2\pi \frac{e^2}{m^2} \mid E_n(z) \mid^2 \frac{1}{\delta\omega \mid 1 - v_{ph}^0/v_{gr}^0 \mid} \mid_{v_{ph}^0 = v} . \end{aligned} \tag{3.43}$$

Here we use the measured values of the electric field $E_n(z)$ and the average wavenumbers k_n^{0r} and damping rates k_n^{0i} of the first half of the beamless slow wave structure. Due to the damping of the waves, it is necessary to deform the Landau contour of the sum over the frequencies and include the pole of the wave-particle resonance.

Using resonance-broadening theory, we calculate the diffusion coefficient according to equation (B.34), where again we neglect the space-charge contribution H_q and set $k_n = k_n^0$. Because the turbulent trapping length, l_{tt}, depends on the diffusion coefficient through equation (B.28), equation (B.34) has to be solved self-consistently.

In figure 3.26 the measured diffusion coefficients, $D_0(v)$, the quasilinear predictions, $D^{ql}(v, z = 0)$, and the resonance-broadening predictions, $D^{ql}(v, z = 0)$, are

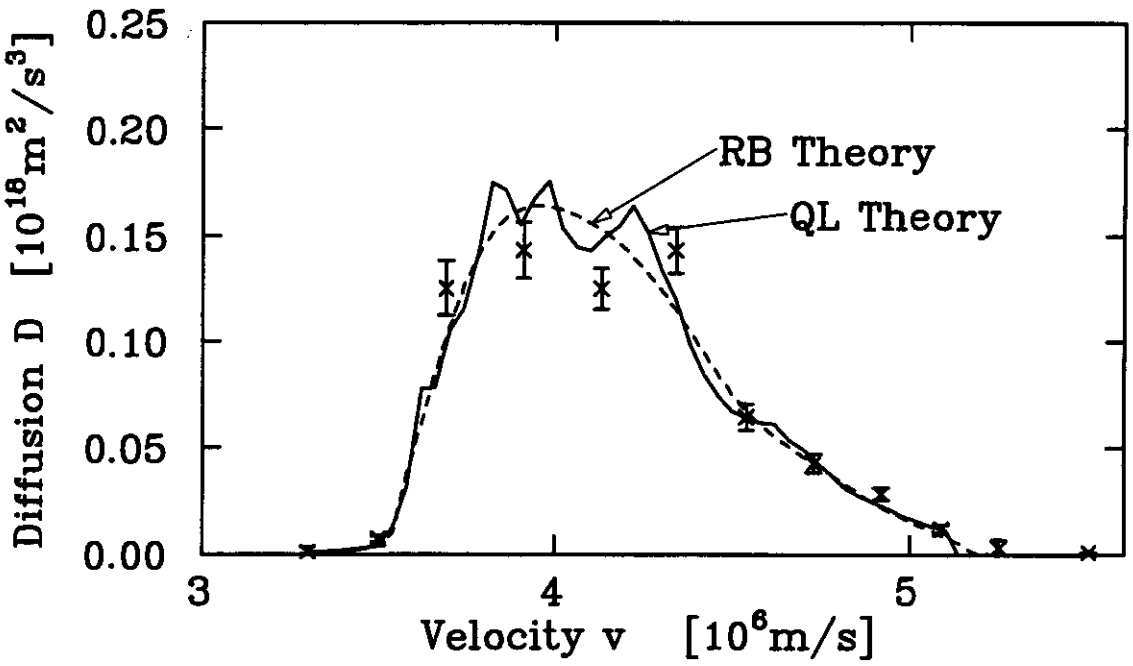

Figure 3.26: Comparison of the measured test beam diffusion coefficient ($\times$) with QL theory (solid) and RB theory (dashed)

shown versus beam velocity. They agree with one another over the range of the spectrum.

3.6.2 Diffusion in the Weak Warm Beam Instability

The measured beam evolution of the weak warm beam instability is well predicted by QL or RB diffusion from the measured electric fields. In this section we compare the measured velocity distribution with the velocity distribution function obtained from solving the diffusion equation where the diffusion coefficients are calculated from the measured electric field according to QL theory and RB theory. We solve the diffusion equation with the calculated values of the quasilinear and resonance-broadened diffusion coefficients from the measured wave amplitudes and the measured initial velocity distribution function.

The diffusion coefficients at any position and velocity are calculated using equations (B.19) and (B.34). We obtain the growth rates by locally fitting straight

lines to the evolution of the ensemble-averaged spectrum and use the cold helix wavenumber k_n^{0r} as an approximation for $k_n^r(z)$. As was shown when calculating the solution of the warm beam dispersion relation, the k_n^{0r} approximation fails near the high velocity edge of the beam where $k_n^r \geq k_n^{0r}$. This renders the wave-particle resonance stronger and therefore overestimates the diffusion coefficient by up to 50%. We also include the space-charge term $H_q(\omega_n)$. Calculating $H_q(\omega_n)$ involves the local velocity distribution of the beam, and is also very sensitive to the value of $k_n(z)$. Rather than solving the dispersion relation at each position in z in order to determine $k_n^r(z)$ and $H_q(\omega_n)$, we find that $H_q(\omega_n)$ is not very sensitive to the shape of the velocity distribution. Therefore we use the values of $H_q(\omega_n)$ calculated from the final velocity distribution for the whole evolution. This procedure slightly underestimates the actual diffusion coefficient.

With these approximations we calculate the QL and RB diffusion coefficient at every 50 mm using the measured electric field spectra for the evolution of the weak warm beam instability. At each position the diffusion coefficient is calculated at 75 different beam velocities spread equally over the width of the electron beam. The stepsize of the integration is chosen to be 50% of the stepsize where numerical instability sets in. The accuracy of the integration is monitored by calculating the total area under the velocity distribution function. In all cases it is 1 ± 0.02.

Figure 3.27 compares the measured velocity distribution function at the end of the interaction region with the calculated distribution using the quasilinear and the resonance-broadened diffusion coefficient, for two different launch levels A. In figure 3.27a a launch level of -8 dB results in an intermediate state at the end of the interaction region. In 3.27b - which is the same case as shown in figure 3.3 - saturation is reached with 0 dB launch attenuation.

The measured beam distribution is qualitatively as predicted by QL and RB

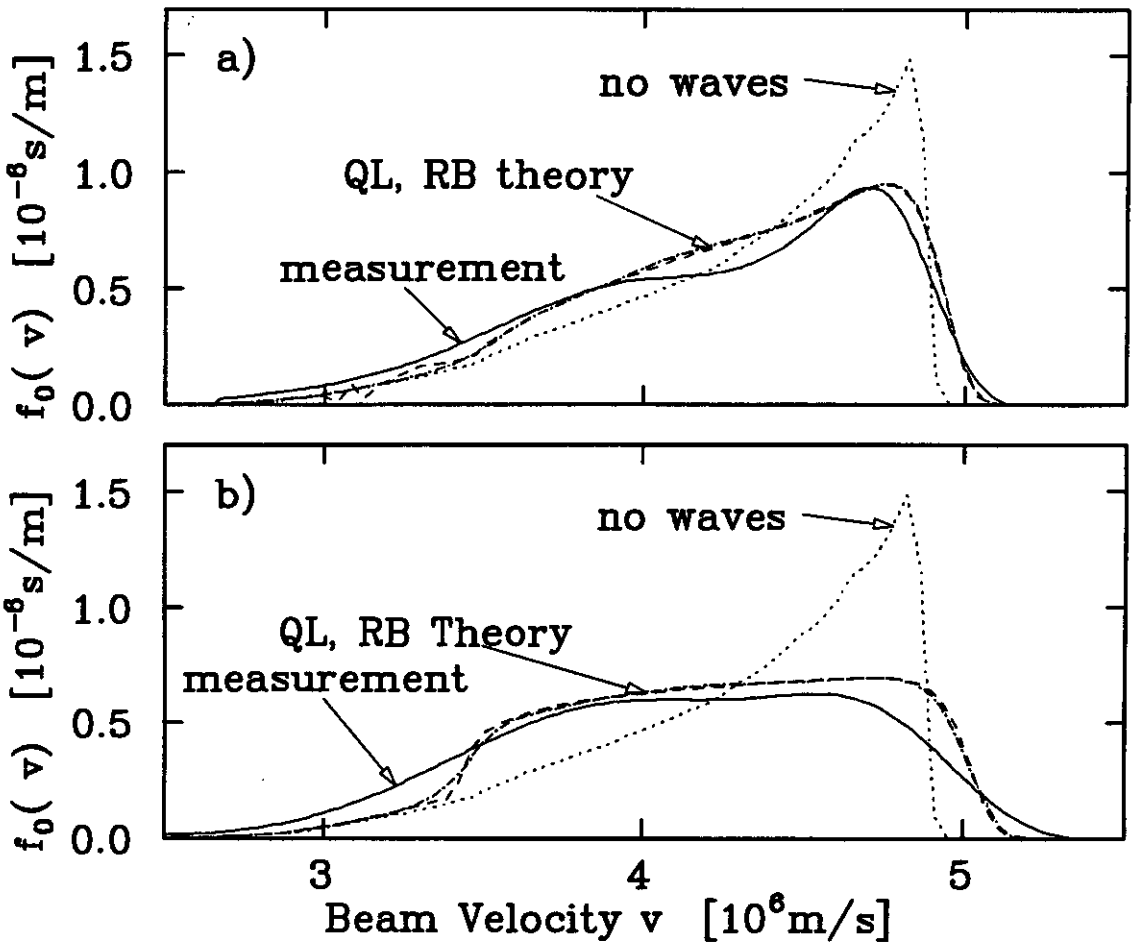

Figure 3.27: Comparison of the measured beam velocity distribution (solid) at the end of the helix with calculation based on QL (dot-dashed)and RB theory (dashed) . a) launch level: -8 dB, b) launch level: 0 dB

diffusion with little difference between the theories. The main systematic difference is that the actual beam is slowed down to velocities where there "should be" no waves according to the TWT dispersion relation. The cause of this effect is presently not understood.

3.7 Power

In this section we compare the total power in the wave spectrum and the power lost in the helix structure with the power loss of the beam. We find power conservation to within 40%.

The total wave power at the end of the interaction region L is calculated according to:

$$P_{tot}(L) = \sum_n \frac{\mid E_n(L) \mid^2}{2(k_n^{r0})^2 R_n} \tag{3.44}$$

The total wave power lost in the wave structure is approximated by:

$$P_{loss}(L) = \int_0^L dz \sum_n 2k_n^{i0}(z) \frac{\mid E_n(z) \mid^2}{2(k_n^{r0})^2 R_n} \tag{3.45}$$

where we use the measured local damping coefficient $k_n^{i0}(z)$. The total beam power is calculated from:

$$P_{beam} = n_0 m \int_0^\infty dv v^3 f_0(v) \tag{3.46}$$

from the measured velocity distribution at the end of the interaction region.

In figure 3.28 we show the wave power, the power loss in the helix and the beam power loss compared to the beam power if no waves are launched for different launch amplitudes A. We find power conservation to within 40% which is within the experimental accuracy of the measurements.

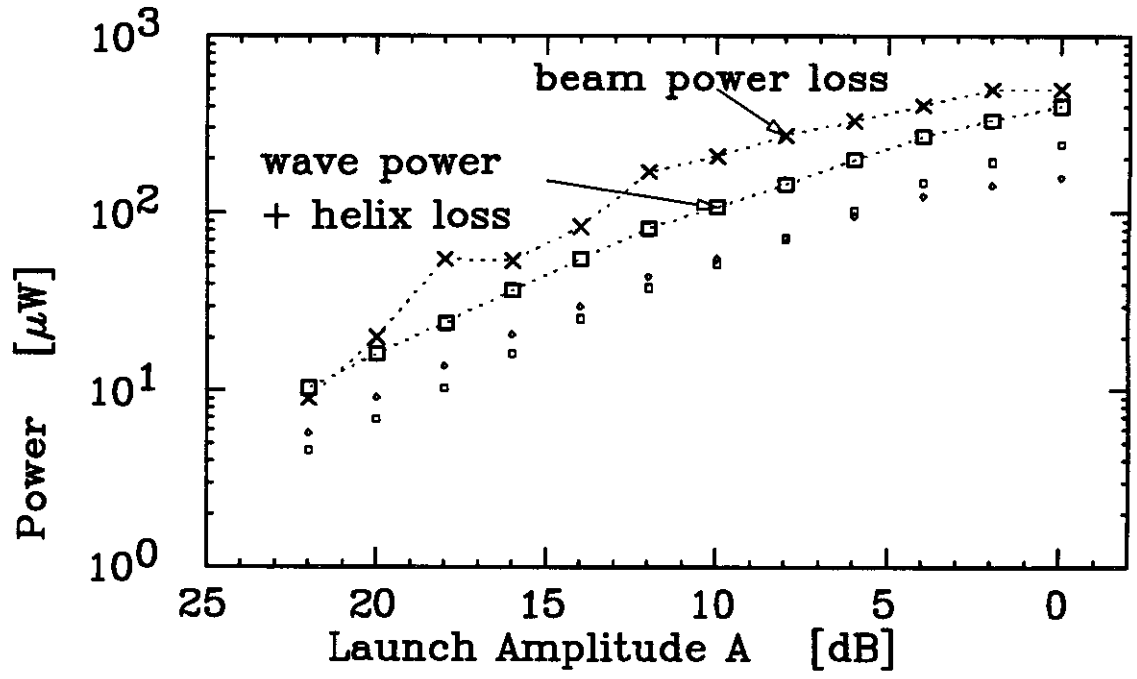

Figure 3.28: Conservation of power for different launch levels A. Beam power loss ($\times$), total wave power (small $\diamond$), total power lost in helix support structure (small $\square$), total wave power and total wave power lost in helix ($\square$).

Chapter 4

Sideband Instability

4.1 Introduction and Overview

In this chapter we experimentally and computationally investigate the stability of a trapped electron state with respect to sidebands. This trapped electron state is similar to the states that result from a saturated beam-plasma instability or from wave saturation in TWTs and Free Electron Lasers (FELs). In theoretical investigations the distribution of trapped electrons is often approximated as a trapped "macro-particle". The focus of this chapter is a comparison between the observed properties of the growing sidebands in experiments and particle simulations and the predictions of parametric theories based on the trapped macro-particle model. We find that growing sidebands that approximately fulfill the sideband resonance and wavenumber matching condition are coupled in qualitative agreement with parametric theories. However, better quantitative agreement exists only between the experiment and particle simulations, indicating the limits of the macro-particle approximation.

It is well known, both experimentally and theoretically, that the nonlinear motion of electrons in the field of a large amplitude plasma wave causes waves at nearby lower and higher frequencies to become unstable. These waves are called sidebands. Their growth was first observed by Wharton, Malmberg and O'Neil [69]

when launching a large amplitude wave in a Maxwellian plasma, and later verified in similar experiments [22, 13, 28, 66, 14]. Sideband growth has also been observed after saturation of a weak cold beam-plasma instability [5, 10, 42, 30, 15, 16], in FELs [68] and in high power TWTs [56]. Numerous authors have investigated the instability in computer simulations [36, 12, 41, 57, 33, 63]. In FELs the growth of these parasitic waves is one of the main mechanisms that limit the performance of the amplifier, since the waves can grow to amplitudes large enough to detrap the electrons, preventing further gain of the amplifier. There continues to be strong interest in the mechanisms and properties of the sideband growth.

Historically two different theoretical approaches have been employed to describe the sideband instability. They differ from one another in their assumption of the dominant mechanism, and each idealizes the real situation accordingly. They are simply called the "quasilinear approach" and the "parametric approach". Here we mention both, even though in our investigation we compare our results only to a parametric theory.

In the quasilinear approach [8, 9, 26, 55], one assumes that the sideband growth is mostly due to changes in the time-averaged velocity distribution. The trapping of electrons that causes a granulation of the velocity distribution in phase space is neglected. This model is successful in describing the sideband growth if a large amplitude wave is launched in a plasma [58], where often only one sideband is observed. The large amplitude wave causes a beam-like perturbation in the velocity distribution. Waves whose phase velocities fall on the positive slope of the distribution grow on this perturbation similar to a beam-plasma instability and form the growing sidebands. Their dispersive properties, particularly their growth rates, are readily derived from a Landau-type calculation. The good agreement between experiment and calculation justifies the presumption that mode-coupling between

waves can be neglected. In this model, no phase relationship exists between the large amplitude wave and the sidebands.

In the parametric approach[37, 24, 43] one assumes the opposite. The sideband growth is due to trapped electrons and the granulation of the velocity distribution in phase-space. Effects associated with the time-averaged velocity distribution are neglected. This approach is useful for studying the stability of BGK states [3] that contain trapped electrons. The theoretical stability analysis of such a state then leads to a parametric coupling between the trapped electrons and the unstable waves. Kruer, Dawson and Sudan [37] treat the simplest BGK-state. They approximate the trapped electron distribution with a single macro-particle trapped at the bottom of a large amplitude wave of constant amplitude. For this model they derive a dispersion relation for small amplitude waves (the sidebands) that are supported by motions of the macro-particle. Each root of the dispersion relation corresponds to a normal mode where the upper and the lower sidebands are coupled and where both have the same frequency separation from the frequency of the trapping wave. Obviously, approximating the trapped electron distribution with a macro-particle is very crude [43]. However, the macro-particle model is intriguing in its simplicity and physical insight, and thus warrants a detailed investigation of the predictions of the model. Such a study is the purpose of this chapter. We will sometimes refer to the macro-particle model by the acronym MPM, which - for good reason, given the authors - may also be interpreted as Maxwell-Prize(-Winner) Model.

A particularly promising trapped electron state, for which the MPM could be useful, has been pointed out by Morales [43]. In computer simulations with a dc electric field along the direction of propagation of an electron beam and a damped wave, he finds cases where the beam is partially trapped in the potential well of the wave. After a few trapping oscillations an asymptotic state of constant

amplitude is reached in which the energy gain of the trapped electrons in the dc electric field balances the energy loss of the damped wave. He argues that the phase space structure of the trapped electrons is sufficiently localized so that one can approximate it with a macro-particle of some effective charge to which the KDS analysis can be applied.

We will generate such a situation in experiments and in computer simulations. We investigate the properties of the growing sidebands both in the regime where the trapping wave amplitude has become constant, and in the regime where there are still some residual trapping oscillations. In both cases the velocity distribution is assumed to have become very granular in phase-space, so that using a parametric rather than a quasilinear approach is justified.

The macro-particle model leads to a number of interesting predictions to which we compare our experimental results. (A derivation of the prediction of the macro-particle models for a TWT will be given in chapter 3.2). Until now, few of these features have been investigated in experiments. The theoretical macro-particle dispersion relation has roots that correspond to two growing sidebands; the maximum growth rates occur for sidebands of angular frequency $\omega_{l,u}$ (the subscripts indicate lower and upper sideband) and wavenumber $k_{l,u}$ that fulfill the "sideband resonance condition" (4.1) [63], given by:

$$\omega_{l,u} - k_{l,u} v_T = \pm \omega_B, \tag{4.1}$$

where the bounce frequency, ω_B, is given by

$$\omega_B \equiv \sqrt{\frac{e k_T E_T}{m}}. \tag{4.2}$$

with v_T the phase velocity and E_T the electric field of the trapping wave. This is simply the requirement that the sideband frequency equals the electron bounce frequency, when Doppler-shifted into the frame of the trapped electrons. A number of authors have checked whether they observed the sidebands at the frequencies

predicted by (4.1) [22, 27] and whether their growth rates agree with the predictions [66]. In general the agreement was within the (large) experimental error bars. The dispersion relation also makes predictions about the wavenumber shifts of the sidebands that have not been investigated before. In particular, it predicts that for each root of the dispersion the wavenumbers of the sidebands fulfill the following matching conditions:

$$\omega_l + \omega_u = 2\omega_T \tag{4.3}$$

$$k_l + k_u = 2k_T \tag{4.4}$$

Each root of the dispersion relation couples the lower and the upper sideband in a "sideband normal mode", characterized by a particular relationship between the amplitudes and phases of the upper and lower sidebands. For the growing solution, the phase relationship is such that the two sidebands contructively interfere and drive the trapped electrons resonantly. The growing sideband normal mode of the KDS dispersion relation is a negative energy mode [63], so increasing the oscillation amplitude of the electrons leads to growth of the sideband amplitudes. A detailed physical model of the sideband growth mechanism is given by Tsunoda and Malmberg (TM) [63].

Tsunoda and Malmberg studied the phase relationship in detail in computer simulations for trapped electron states more complex and general than a single trapped macro-particle and found that the growing sidebands were still coupled and established a particular phase relationship with one another. They defined a new quantity, the (time-)"invariant phase", that conveniently measures the phase relationship between the trapping wave and the two sidebands. The focus of their analysis was the question whether this phase relationship had general relevance, and not whether the trapped particle model was quantitatively correct. Therefore, for example, they did not investigate the amplitude ratio between the sidebands for all

cases. As we will se, the invariant phase is just one property of the sideband normal modes.

Related work was done by Dimonte and Malmberg [16], who did not limit themselves to small sidebands and studied the detrapping mechanism and DeNeef [14], who studied sidebands for very small sideband frequency separations where the trapped electrons were not able to distinguish the sideband frequencies within the interaction length.

We have studied the evolution of the growing sidebands of small amplitudes in experiments and computer simulations for different cases of a dynamical trapped particle equilibrium and compared them with predictions of the KDS dispersion relation based on the macro-particle model. In our experiments the sideband frequencies are well separated from the trapping wave frequency such that the trapped beam electrons can distinguish their frequencies within the length of the interaction region L. This requires that

$$\frac{v_T}{\delta\omega_{sb}(1-\frac{v_T}{v_T^{gr}})} \ll L \tag{4.5}$$

where L is the length of the interaction region, v_T^{gr} is the group velocity of the trapping wave and $\delta\omega_{sb} \equiv \omega_u - \omega_T$.

Experimentally the trapped particle state is created by launching a wave of large amplitude that traps an almost synchronous cold electron beam. By applying an additional dc electric field one can obtain a situation where a fraction of the beam electrons is trapped near the bottom of the trapping wave potential, and where the trapping wave propagates with constant amplitude or with some trapping oscillations depending on the launch level of the wave. Following Kruer, Dawson and Sudan [37] and Morales [43] we approximate the trapped electron distribution as a trapped macro-particle. We can then describe the trapped electron state with four parameters:

- the bounce frequency of the trapped macro-particle (reduced compared to the bounce frequency given by equation (4.2) because of the applied dc electric field),
- the effective beam plasma frequency (reduced compared to equation (2.17) because only a fraction of the beam is trapped),
- the trapping wave frequency
- the phase velocity of the trapping wave (reduced compared to v_T^0 because of the trapped electrons).

We derive the dispersion relation of the sidebands for the TWT in appendix E. It depends only on these three parameters and the helix dielectric.

We study the evolution of the sidebands by launching a waveform with the arbitrary waveform generator, consisting of the trapping wave and two sidebands.The sidebands have equal frequency difference from the trapping wave but much lower amplitude. We establish that they evolve linearly. The spatial evolution of the sidebands depends only on their amplitude ratio and their phase relationship (given by the invariant phase) at launch. However, for certain sideband frequency separations from the trapping wave, we find that after a distance of one to two trapping oscillation lengths the evolution of the sidebands is independent of their initial conditions. Thus the evolution can be characterized by a

- constant and equal growth rate of both sidebands,
- constant wavenumber shift of both sidebands,
- constant amplitude ratio of the sidebands,
- constant phase relationship between sidebands.

This is in qualitative agreement with the macro-particle model, since after some distance the growing sideband normal mode has outgrown all other modes, such that only its properties are being measured.

We computationally simulate the evolution of the instability by following the orbits of the beam particles and find good agreement with the observed evolution. We find the maximum sideband growth for smaller frequency separations than predicted from the sideband dispersion relation. The quantities that characterize the experimentally growing sideband mode are only in qualitative agreement with the calculated values. With computer simulations that consider more idealized situations, that are not realizable experimentally, we establish that this discrepancy is due to the approximation of the trapped particle distribution with a macro-particle and not due to any peculiarities of the experiment.

We do not find phase-lock between sidebands if the dispersion of the helix requires large wavenumber changes of the sidebands in order to fulfill the wavenumber matching condition, even though the MPM dispersion relation still predicts such sideband normal modes. We also do not find coupling between sidebands and a wave at the frequency of the sideband frequency separation, in contrast to an extension of the sideband dispersion relation to three waves.

We also study the case where the trapping wave shows trapping oscillations, and we find coupling of the sidebands for certain sideband frequencies. All the quantities that describe the sideband normal mode are observed to be spatially modulated with the wavenumber of the trapping wave oscillations.

This chapter is organized as follows. In section 4.2 we introduce the main elements of the particle simulation and macro-particle theory. In section 4.3 we present the computational and experimental results for spatially constant trapping wave amplitudes and in section 4.4 for trapping wave amplitudes exhibiting trapping

wave oscillations.

4.2 Theory

In this section we describe the core elements of our computer simulations that follow the individual electron orbits, derive expressions that relate the properties of the trapped electron distribution to the measurable quantities and formulate the KDS theory of the considered trapped electron state for spatial evolution. We introduce all quantities that we will be measuring in the following sections of this chapter.

4.2.1 Nonlinear TWT Equations

In appendix F we review the derivation of the nonlinear TWT equations that we will be using. These equations describe the one-dimensional interaction of an initially cold beam with many waves on a slow wave structure. The wave frequencies are assumed to be commensurate and the beam is described as a collection of charged particles of cylindrical shape (radius r_b) that can penetrate one another. The wave frequency components of the beam charge distribution couple to the helix normal modes through the transmission line equation (2.9). The particles of the beam generate space-charge forces through Poisson's equation (2.12). Their accelerations are determined from Newton's equation (2.6) and therefore retain the full nonlinear dynamics. The resulting equations are first order in the spatial distance from the transmitter and are solved by integration, starting with known initial conditions. This situation is exactly analogous to the experiment where the waves also have commensurate frequencies and completely defined initial conditions.

4.2.2 Trapped Macro-Particle State

Morales [43] pointed out that a BGK state where all the trapped electrons form a localized clump in phase space is very idealized and typically does not exist. Even for the cold beam-plasma instability where the trapping oscillations finally

subside due to phase-mixing, one cannot apply such a simple-minded model since the trapped electrons are not bunched in phase space. However, a BGK-like state with clumped trapped electrons can be reached in a situation where the plasma has some damping mechanism other than Landau damping and an external dc electric field is applied to the electrons. In computer simulations he finds that deeply trapped electrons that cannot be accelerated in the dc electric field transfer their energy gain to the wave and lead to an increase in wave amplitude. The wave power grows until a final state is reached where the wave power loss due to damping equals the power gain of the trapped electrons. This final state is characterized by trapped electrons bunched in phase space within the separatrix given by the trapping wave amplitude. The electrons that were not trapped initially are constantly being accelerated by the dc electric field and create a high velocity beam. Since the interaction of the very fast, untrapped electrons with waves with frequencies close to the trapping wave frequency is negligible, he argues that this final state renders the MPM applicable.

Within the framework of the traveling wave tube theory the final steady state for such a situation is found from energy and momentum conservation. Limiting the analysis to one wave and neglecting space-charge, one obtains from (F.7) and (F.8) for the conservation of momentum (all scaled quantities are introduced in appendix F)

$$\frac{d}{dy}\Big[\frac{1}{1+Cb}\int_0^{2\pi}\frac{d\phi_0}{2\pi}q+A^2\Big]=-2A^2d+\frac{1}{1+Cb}\int_0^{2\pi}\frac{d\phi_0}{2\pi}\frac{E_{dc}}{E_T}\frac{1}{1+Cq} \tag{4.6}$$

and for the conservation of energy

$$\frac{d}{dy}\Big[\int_0^{2\pi}\frac{d\phi_0}{2\pi}\frac{q^2}{2}+\Big(2\frac{d\Theta}{dy}+b\Big)A^2\Big]=-2\frac{d\Theta}{dy}A^2d+\int_0^{2\pi}\frac{d\phi_0}{2\pi}\frac{E_{dc}}{E_T}. \tag{4.7}$$

Steady state requires that the left hand sides of equations (4.6) and (4.7) vanish. Following the analysis of Morales [43] and assuming that the trapped electrons form a macro-particle of zero spread in phase space one finds the following relations for

the final electric field amplitude E_T^{∞} of the trapping wave

$$k_T^{0i} \frac{E_T^{\infty 2}}{k_T^{0r 2} R_T} = e n_0 \sigma u_0 E_{dc} \tag{4.8}$$

and for the wavenumber

$$k_T^{\infty} = k_T^{0r}[1 + \sqrt{\left(\frac{E_T^{\infty}}{E_{dc}}\right)^2 - \frac{k_T^{0i}}{k_T^{0r}}}]. \tag{4.9}$$

σ is the ratio of the trapped electrons to the total number of electrons; it is a dimensionless quantity between 0 and 1. R_T is the interaction impedance of the trapping wave. Because not all the electrons of the beam are trapped, the beam plasma frequency is reduced by $\sqrt{\sigma}$. The wavenumber shift, $k_T^{\infty} - k_T^{0r}$, is always positive and decreases the phase velocity of the trapping wave, even though the applied electric field is pulling on the electrons in the direction of the wave propagation. The asymptotic phase velocity v_T^{∞} of the trapping wave is given by:

$$v_T^{\infty} \equiv \frac{\omega_T}{k_T^{\infty}} \tag{4.10}$$

The formed macro-particle is in a modified equilibrium state compared to the original KDS model. Due to the applied dc electric field, the macro-particle's equilibrium position is shifted with respect to the trapping wave potential by

$$\Delta\Theta \equiv \arcsin\left(\frac{E_{dc}}{E_T^{\infty}}\right) \tag{4.11}$$

in the opposite direction of the externally applied field. The modified bounce frequency, ω_B^{dc}, of oscillations around this new equilibrium is given by:

$$\omega_B^{dc} \equiv \omega_B \left[1 - \left(\frac{E_{dc}}{E_T^{\infty}}\right)^2\right]^{\frac{1}{4}} \tag{4.12}$$

This is not to be confused with an effective bounce frequency of the macro-particle of finite extend that is an average of the bounce frequency of electrons at different positions in the sinusoidal trapping well.

Within the macro-particle picture this trapped electron state is now characterized by four quantities:

- ω_B^{dc} the modified bounce frequency of the trapped electrons,
- $\sqrt{\sigma}\omega_p$ the beam plasma frequency of the trapped electrons,
- ω_T the trapping wave frequency,
- v_T^{∞} the modified phase velocity of the trapping wave.

4.2.3 Macro-particle Model

Kruer, Dawson and Sudan [37] in their sideband analysis argue that the main mechanism of the sideband growth is due to the presence of trapped particles in the potential well of the large amplitude wave. In Appendix E we apply their analysis to the spatial evolution of the instability on a TWT. Here we summarize the main steps of this derivation.

Kruer, Dawson and Sudan simplify the trapped particle distribution with a macro-particle and consider the linear stability of an array of harmonically bound oscillators (with bounce frequency ω_B) that is moving with velocity v_T through a linear background plasma. This is an analytically tractable stability analysis of a BGK equilibrium [25]. They require that the sidebands are self-consistently generated by the trapped macro-particles. This leads to a set of equations that couple waves of different frequencies and wavenumbers. They truncate the series by limiting the possible coupling to lower and upper sidebands of frequencies ω and $2\omega_T - \omega$ and arrive at two linear equations for the complex amplitudes of these two sidebands. The requirement to fulfill both equations simultaneously leads to a dispersion relation. For our case this dispersion relation is given by (E.7):

$$\frac{\sigma\omega_p^2}{(kv_T^{\infty}-\omega)^2-\omega_B^{dc2}}\left[\frac{\omega/kv_T^{\infty}}{\epsilon^h(\omega,k)}+\frac{(\omega-2\omega_T^{\infty})/(k-2k_T^{\infty})v_T^{\infty}}{\epsilon^h(\omega-2\omega_T^{\infty},k-2k_T^{\infty})}\right]=1 \qquad (4.13)$$

Here we have anticipated that we will study the asymptotic case predicted by Morales [43].

For some frequencies, one can find roots of this dispersion relation. These roots correspond to growing or to damped sidebands. Both sidebands have the same growth rate k_{sb}^i and their wavenumbers k_u, k_l are related by:

$$k_u^r + k_l^r = 2k_T^\infty \tag{4.14}$$

Each root corresponds to a "sideband normal mode" with a particular relationship between the complex amplitudes of the upper and the lower sideband given by equation (E.8).

$$\frac{E_u^*}{E_l} = \frac{E^*(k_u^r, w_u)}{E(k_l^r, \omega_l)} = \Big[\frac{kv_T^\infty}{\omega_p}\frac{\epsilon^h(k,\omega)}{\omega_p^2}\Big((\omega - kv_T^\infty)^2 - (\omega_B^{dc})^2\Big) - 1\Big] \equiv -\alpha e^{i\theta} \tag{4.15}$$

We call α the "sideband amplitude ratio" and show below that θ is simply related to the "invariant phase" previously defined by Tsunoda and Malmberg [63].

Every wavenumber solution, $k_{l,u}$, of the modified KDS dispersion relation for given sideband angular frequency, $\omega_{l,u}$, corresponds to a "sideband normal mode" characterized by the following four quantities: the sideband wavenumber change relative to the trapping wave wavenumber $(k_{l,u}^r - k_{l,u}^{0r})/k_T^{0r}$, the sideband growth rate relative to the trapping wave wave number $k_{l,u}^i/k_T^{0r}$ and the magnitude, α, and phase, θ, of the ratio of the complex amplitudes of the upper to the lower sideband of the growing sideband mode. In this study we compare these four quantities with the experimentally measured values.

The modulational phase Θ of the two sidebands is easily measured and has physical relevance. With our previous definition (2.1) of the phases and amplitudes of the complex electric field amplitudes we define our modulational phase in accordance with Tsunoda and Malmberg [63] as:

$$\Theta(z) = 2 * \phi_T(z,t) - \phi_l(z,t) - \phi_u(z,t) \tag{4.16}$$

$$= 2k_T^r - k_l^r - k_u^r + 2\phi_T^0 - \phi_l^0 - \phi_u^0 \tag{4.17}$$

It is time-independent because the frequencies of the upper and the lower sidebands are symmetric to the trapping wave frequency ω_T.

$$w_l = \omega_T - \delta\omega_{sb} \tag{4.18}$$

$$w_u = \omega_T + \delta\omega_{sb} \tag{4.19}$$

If the upper and the lower sideband form a sideband normal mode, then their wavenumbers are related to one another through equation (4.14) with the wavenumber of the trapping wave given by the asymptotic value of the steady state case. Using (4.15) we indeed find:

$$\Theta(z) = \theta - \pi + 2\Delta\Theta \tag{4.20}$$

where we have included the change induced by the change of the equilibrium position of the macro-particle. We call Θ the "modulational phase", because one can show that the sum of the trapping wave and two small sidebands of equal amplitude ($\mid E_l \mid = \epsilon \mid E_T \mid$, $\mid E_u \mid = \epsilon \mid E_T \mid$ with $\epsilon \ll 1$) can be written as:

$$E_T(z,t) + E_l(z,t) + E_u(z,t) = \mid E_T \mid (1 + \epsilon f)\cos(\psi_0 + \epsilon g) \tag{4.21}$$

where

$$f = 2\cos\Theta\cos\Big(-\delta\omega_{sb}t + \frac{k_u - k_l}{2}z + \frac{\phi_u^0 - \phi_l^0}{2}\Big)$$

$$g = 2\sin\Theta\cos\Big(-\delta\omega_{sb}t + \frac{k_u - k_l}{2}z + \frac{\phi_u^0 - \phi_l^0}{2}\Big)$$

If $\Theta = 0$, g vanishes and the sum of the three waves is amplitude modulated, if on the other hand $\Theta = \pi$, f vanishes and the sum is frequency modulated.

4.3 Trapped State without Trapping Oscillations

In this section we experimentally investigate a trapped electron state where the trapping wave amplitude does not show trapping oscillations. An external dc electric field is applied of such magnitude that the trapping wave amplitude is fairly constant near the end of the interaction region. The experimentally observed evolution of the sidebands is in good agreement with computer simulations for different cases. Near the end of the interaction region we observe a growing sideband normal mode characterized by constant growth rates, wavenumber shifts, amplitude ratio and phase relationship of the sidebands. The predictions of the sideband dispersion relation are only qualitatively correct.

In section 4.3.1 it is shown how a trapped electron state of nearly constant trapping wave amplitude can be created by applying an external dc electric field to an otherwise damped wave. The measured evolution is compared with computer simulations and good agreement is found. Using conservation of momentum (4.6) we can calculate the trapped particle ratio σ in good agreement with the computer simulation.

In section 4.3.2 the measured spatial evolution of the sideband amplitudes and phases is shown for different initial conditions. We find good agreement between the measured evolutions and computer simulations. The evolution of the sidebands depends on the amplitude ratio and the initial value of the modulational phase. After about one to two trapping oscillations the sidebands are found to grow independently of their initial conditions and can be characterized by a constant growth rate, wavenumber shift, amplitude ratio and modulational phase. This is in agreement with the sideband dispersion where some distance away from the transmitter the growing sideband normal mode is able to become dominant. We focus on the evolution of the modulational phase in order to decide whether we obtain a side-

band normal mode near the end of the interaction region. For some singular initial conditions we do not see "phase-lock" (modulational phase spatially constant and independent of its initial values) near the end of the interaction region. Within the trapped particle model we argue that for those cases the growing sideband mode was launched too low to be able to outgrow the non-growing sideband modes by the end of the interaction region. We observe phase-lock for a range of frequencies for different trapping wave amplitudes.

In section 4.3.3 we compare the experiments with computer simulations that follow the many beam particles and find good agreement.

In section 4.3.4 the characteristics of the experimental and computational sideband growth are compared with the predictions of the macro-particle model. The frequency regime for which we experimentally find phase-lock corresponds to a lower bounce frequency than predicted from the macro-particle model. The values of the growth rates, wavenumber shifts, amplitude ratio and modulational phase only qualitatively agree with the experimental values. Reducing the value of the bounce frequency used in the sideband dispersion leads to better agreement. We show that in contrast to the macro-particle model and the sideband dispersion we find phase-lock only for certain regions of the helix dispersion relation where the required wavenumber shifts of the sidebands are small. An extension of the sideband dispersion relation to three waves predicts coupling and a large wavenumber shift of the difference wave. We do observe a difference wave; it is, however, not phase-locked to the sidebands and the trapping wave, because its wavenumber shift is small. It therefore cannot be explained within the frame-work of the macro-particle model.

In section 4.3.5 we establish that the found discrepancies between the experimental observations and the predictions of the sideband dispersion relation are caused by simplification of modelling the trapped particle distribution with a macro-

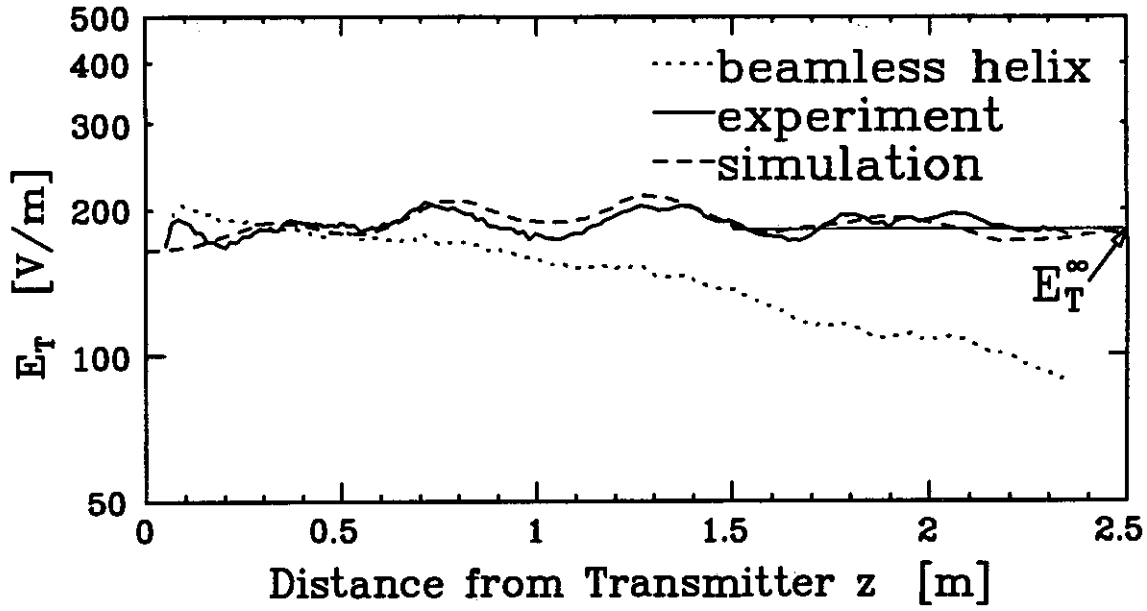

Figure 4.1: Spatial evolution of the trapping wave experiment (solid), computer simulation (dashed), wave on beamless helix (dotted). Parameters are: $f_T = 55.5\text{MHz}$, $I_b = 48\mu\text{A}$, $V_c = 46.5\text{V}$.

particle.

4.3.1 Creating a Trapped Electron State

Experimentally, the mono-energetic electron beam is trapped by launching the trapping wave at about the saturation level of the cold beam instability. At the position of the transmitter, the electron beam velocity approximately equals the phase velocity of the trapping wave. Tsunoda and Malmberg [62] showed that the largest growth rates of a wave due to trapped electrons that are subject to an externally applied dc electric field occur if the wave is launched at a high level and initially traps a large fraction of the electron beam. For such high launch values of the trapping wave we find that the initial trapping oscillations are small and that a state of constant wavenumber shift and constant amplitude can be reached within the length of the interaction region. This can be seen in figure 4.1 where the solid line shows the experimentally observed spatial evolution of the electric field

amplitude of the trapping wave when an accelerating dc electric field is applied and the initial velocity of the electron beam equals the phase velocity of the trapping wave. For $z > 1.5$m we assume that an asymptotic trapped particle state has been reached and we approximate the measured field amplitude with its averaged value of $E_T^\infty = 182$V/m. This value is shown as a thin line in figure 4.1. Near the end of the helix the trapping wave still shows some amplitude modulations by about 1.5 dB. They are caused by the spatial dependence of the wavenumber and damping rate in the beamless helix and by space-charge effects that prevent a steady-state. We find good agreement with our computer simulations only if we use the local values of wavenumber and damping rate and keep the space-charge term. The result of the computer simulation is shown as a dashed line and agrees well the experiment. The dotted line shows the wave damp by about a factor of 2.5 over the length of the interaction region in the beamless case.

In figure 4.2a we show the calculated phase space distribution of the electrons and in figure 4.2 its velocity histogram. It can clearly be seen that the electron distribution consists of a trapped and an untrapped portion. The untrapped electrons have been accelerated by the dc-electric field to high velocities and therefore no longer resonate with the trapping wave. In fact, by the end of the interaction region the untrapped electrons have velocities higher than the highest phase velocity of the helix waves ($v_{ph} \approx 5.5 \times 10^6$m/s). Therefore they cannot contribute to wave-particle resonances. The separatrix of the trapping wave calculated from the average electric field E_T^∞ is shown as a dashed line. Since an electron experiences the trapping wave potential and the applied dc field, the effective separatrix of the trapping wave is distorted. It is shown as a solid line. The location of the minimum of the effective wave potential is marked with a cross $\times$. It is at velocity v_T^∞ (calculated from equation (4.10)), that is slightly smaller than the phase velocity v_T^0

on the beamless helix, and at the phase $\Delta\theta$ (calculated from equation (4.11)). We find that most of the electrons, that have not been become run-aways, are confined within the effective separatrix. The trapped macro-particle model approximates this trapped distribution with one macro-particle of effective charge, mass and certain location. The diamond $\diamond$ in figure 4.2 marks the location of the center of mass of the trapped distribution. It is located close to the minimum of the effective potential ($\times$). Therefore we conclude that we can use equations (4.10) and (4.11) to obtain the center of the macro-particle in phase space. With our experimental setup it is not possible to measure the position of the electrons in phase-space. But we can measure the time-averaged axial energy distribution at the end of the interaction region and compare it to the simulation results. This is done in figure 4.2b for the case shown in figure 4.1. The dashed line shows the time-averaged velocity distribution function obtained from the simulation for the parameters of the case shown in figure 4.1. It is simply the histogram of the phase space distribution shown in a). The agreement between the experiment and the results of the simulation is reasonable. The shaded region marks the region of trapped electrons given by the effective trapping wave potential. Since the electrons are bunched within the separatrix of the effective potential and since the potential is only slightly distorted one can approximate the region of trapped electrons from $v_T^0 \pm \sqrt{eE_T^\infty/mk_T^\infty}$.

We characterize the final trapped electron state with the modified bounce frequency ω_B^{dc}, the final phase velocity v_T^∞ and the effective beam plasma frequency $\sqrt{\sigma}\omega_p$ in addition to the trapping wave frequency f_T. The final electric field amplitude of the trapping wave E_T^∞ and its wavenumber shift δk_T^∞ can be measured directly. The trapped electron ratio can be inferred from the time-averaged energy distribution function (the fraction of the shaded area to the total area) and from energy (4.9) and momentum conservation (4.8). In figure 4.3 the values of σ calculated

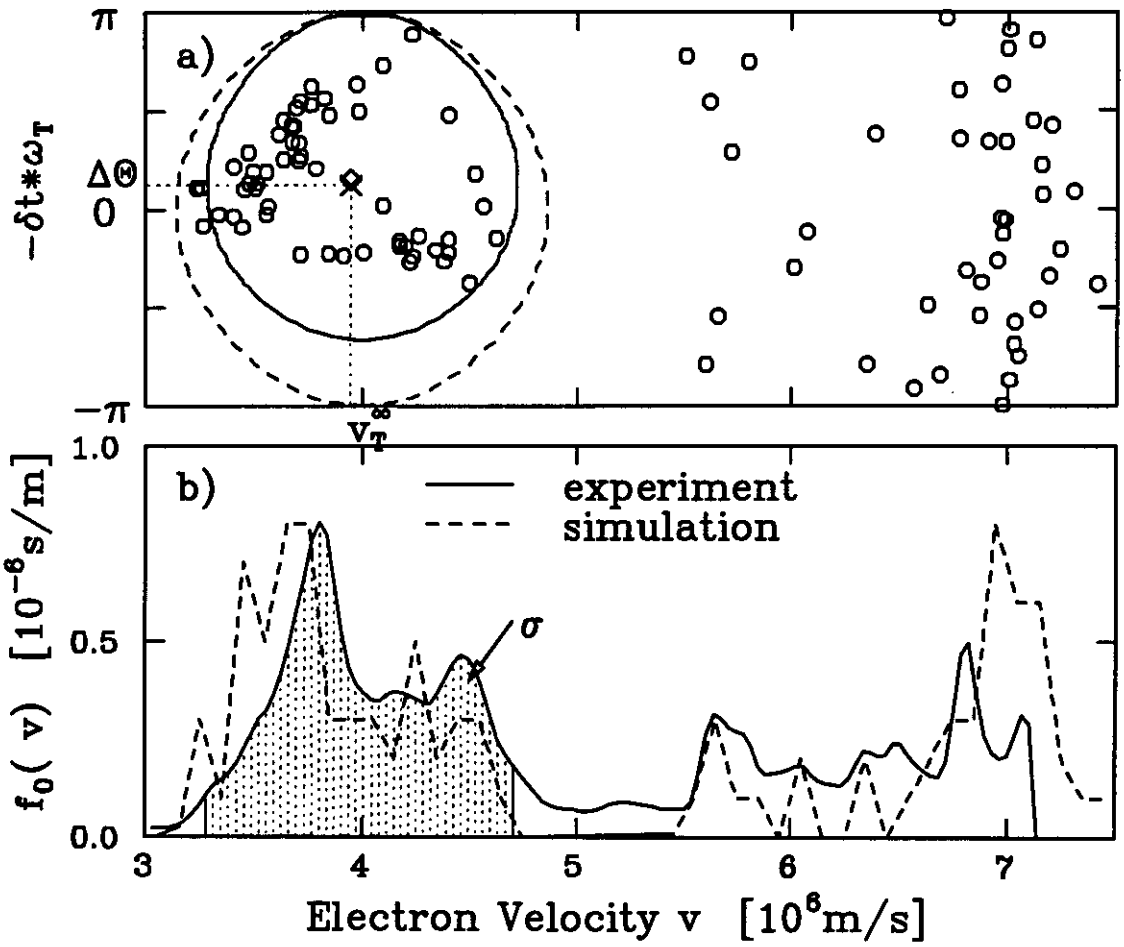

Figure 4.2: a) Phase-space plot of the electrons of the simulation. Dashed line is separatrix of trapping wave amplitude $E_T^{\infty} = 182\text{V/m}$, solid line is separatrix distorted by E_{dc}. $\times$ is center of trapped electrons from (4.10) and (4.11). $\diamond$ is center of trapped electrons from simulation.b)Time-averaged axial velocity distribution function at the end of the interaction region of the case shown in figure 4.1. Experiment (solid), simulation (dashed). The shaded area approximately marks the electrons trapped in the wave trough.

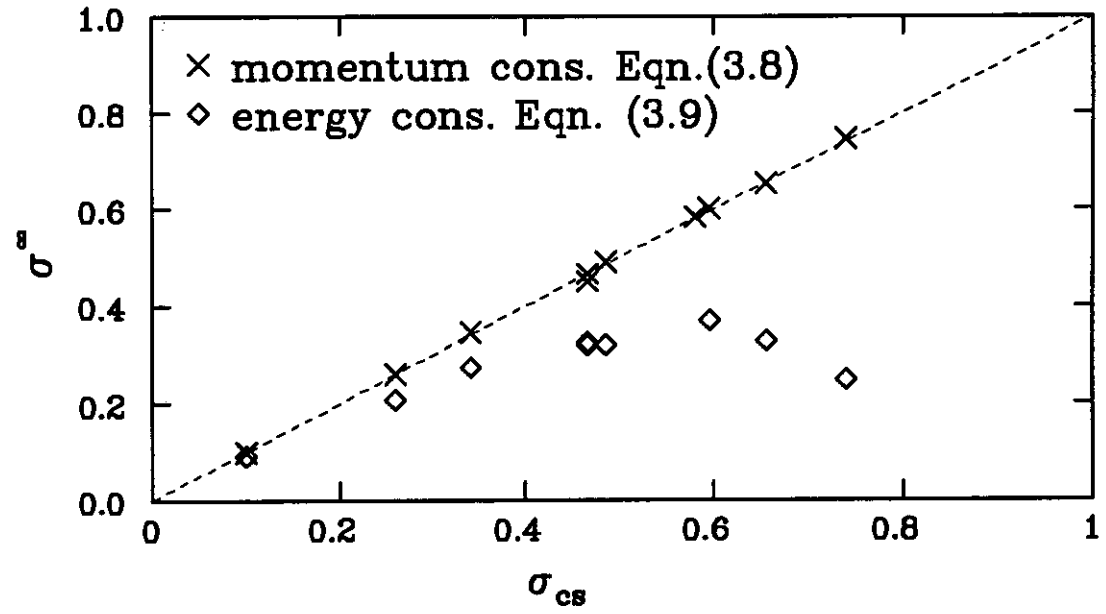

Figure 4.3: Trapped electron ratio. σ_{cs} from simulations compared to σ^{∞} from equations (4.8)(×) and (4.9)(◇).

from (4.8) and (4.9) are compared with the actual fraction of trapped electrons σ_{cs} derived from computer simulations for different cases. It is obvious that the trapped electron ratio based on momentum conservation (4.8) agrees well with the trapped electron ratio of the computer simulation, whereas the trapped electron ratio based on energy conservation does so only in the limit of small σ. This shows that the macro-particle approximation of the distribution of trapped electrons approximately preserves momentum conservation but violates energy conservation. Therefore we use the momentum conservation (4.8) to calculate the trapped electron ratio σ from the measured values of the applied dc electric field, the final wave amplitude and beam current. The ratio of the shaded area to the total area under the velocity distribution function is the trapped electron ratio σ and agrees with the value derived from equations (4.8) within 20%.

4.3.2 Evolution of the Sidebands

In this section we investigate the properties of sidebands for such a trapped electron state. The sidebands are launched with equal frequency separations from the trapping wave and small amplitude. Experimentally they are launched at the same position as the trapping wave and in a manner described in section 2.2 making it possible to choose particular initial values of the phases and amplitudes of the sidebands. The focus of this study is the sideband evolution well before detrapping of the electrons occurs, while the perturbations of the trapped electron orbits are still small. This region is given experimentally where the evolution of the sidebands depends only on the ratio of the sideband amplitudes to each other and not to the trapping wave amplitude. Such a situation could arise from sideband growth from noise if the interaction region was long enough so that the fastest growing sidebands could become dominant over the background noise.

We find that for small enough sideband amplitudes the evolution of the sidebands depends only on the sideband amplitude ratio α and the modulational phase Θ. For a certain band of sideband frequencies we observe that the sidebands evolve differently depending on the initial values of amplitude ratio and modulational phase but in such a manner that close to the end of the interaction region their amplitude ratio and their modulational phase are independent of their initial values and spatially constant. Also growth rates and wavenumber shifts are approximately independent of the initial waveform and constant. This is in agreement with the sideband dispersion relation based on the macro-particle model where the growing sideband normal mode outgrows the other modes by the end of the interaction region. Singular cases where this is not the case arise for particular values of the initial amplitude ratio and modulational phase and can be interpreted as situations where a nongrowing mode of the sideband dispersion relation is being launched. Outside this band of sideband

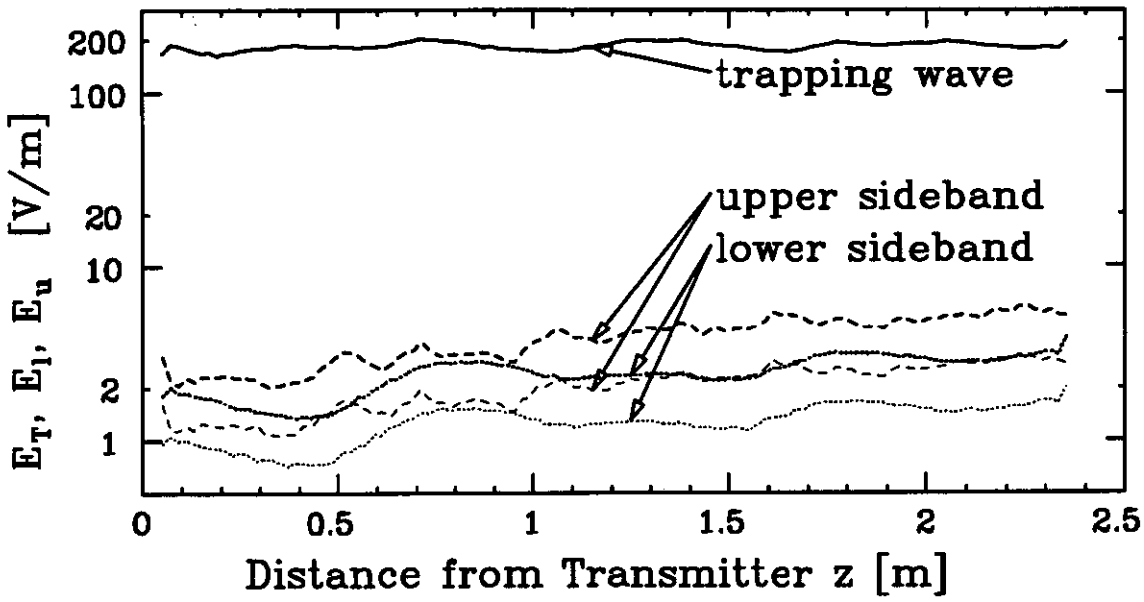

Figure 4.4: Spatial evolution of the sidebands for different launch amplitudes. For thin lines sidebands are launched 50% lower. Same parameters as in figure 4.1, $f_T = 55.5\text{MHz}$, $\Delta f = 14.06\text{MHz}$, $\Theta(z=0) = \pi$, $\alpha(z=0) = 1$.

frequencies we do not observe phase-locking, however, at least one of the sideband is growing.

Linear Perturbation of the Electron Orbits

The spatial evolution of the sidebands studied depends only on the launch value of the sideband amplitude ratio and the modulational phase.

The thick lines in figure 4.4 show the spatial evolution of the sidebands and the trapping wave amplitudes for a case where the sidebands are launched with equal amplitudes and a modulational phase of π. This launched waveform could be described as a frequency modulated wave.

In a second experiment, the sidebands are launched by a factor of 2 smaller. Their evolutions are shown in figure 4.4 as thin lines and track the evolution of the sidebands of the first case with a 6 dB offset. From this, one can conclude that the perturbation of the electron orbits is linear and that the KDS theory is applicable. In

general, this is true for sidebands smaller than the trapping wave by about a factor of 20 throughout the interaction region.

We also find that changing the initial phases of the sidebands but keeping the modulational phase and the amplitude ratio of the sidebands constant does not change the evolution of the sidebands. This is expected from the simple expression for the superposition of the trapping wave and the sidebands (4.21).

Sample Sideband Evolution

In figure 4.5 we show the experimentally observed spatial evolution of the amplitudes and phase shifts of the trapping wave and the sidebands for $\Theta(z=0)=\pi$ and $\alpha(z=0)=1$. The launch levels of the sidebands are the same as for the larger amplitude case in figure 4.4. It shows that at some distance from the transmitter the growth rates of the sidebands are equal and constant, their amplitude ratio is constant, their wavenumber changes are constant and the modulational phase is constant in agreement with the macro-particle model where the growing sideband normal mode has outgrown the non-growing sideband normal modes.

In figure 4.5a we see that, in the second half of the interaction region for $z > 1.5$m, the sidebands are growing at approximately the same constant rate. A straight line fits well to the spatial evolution of the logarithm of the amplitudes and yields growth rates of $k_u^i \approx 0.23\text{m}^{-1}$ for the upper and $k_l^i \approx 0.20\text{m}^{-1}$ for the lower sideband. Because the growth rates of the sidebands are approximately the same, their amplitude ratio stays nearly constant, $\alpha \approx 1.7$. In figure 4.5b we see that the phase shift of the trapping wave is approximately linear with distance for $z > 1$m, corresponding to a spatially constant wavenumber change $\delta k_T^\infty \approx 1.2\text{m}^{-1}$. This is another confirmation (in addition to the constant trapping wave amplitude) that an asymptotic trapped particle state has been reached. For distances $z > 1.5$ m the

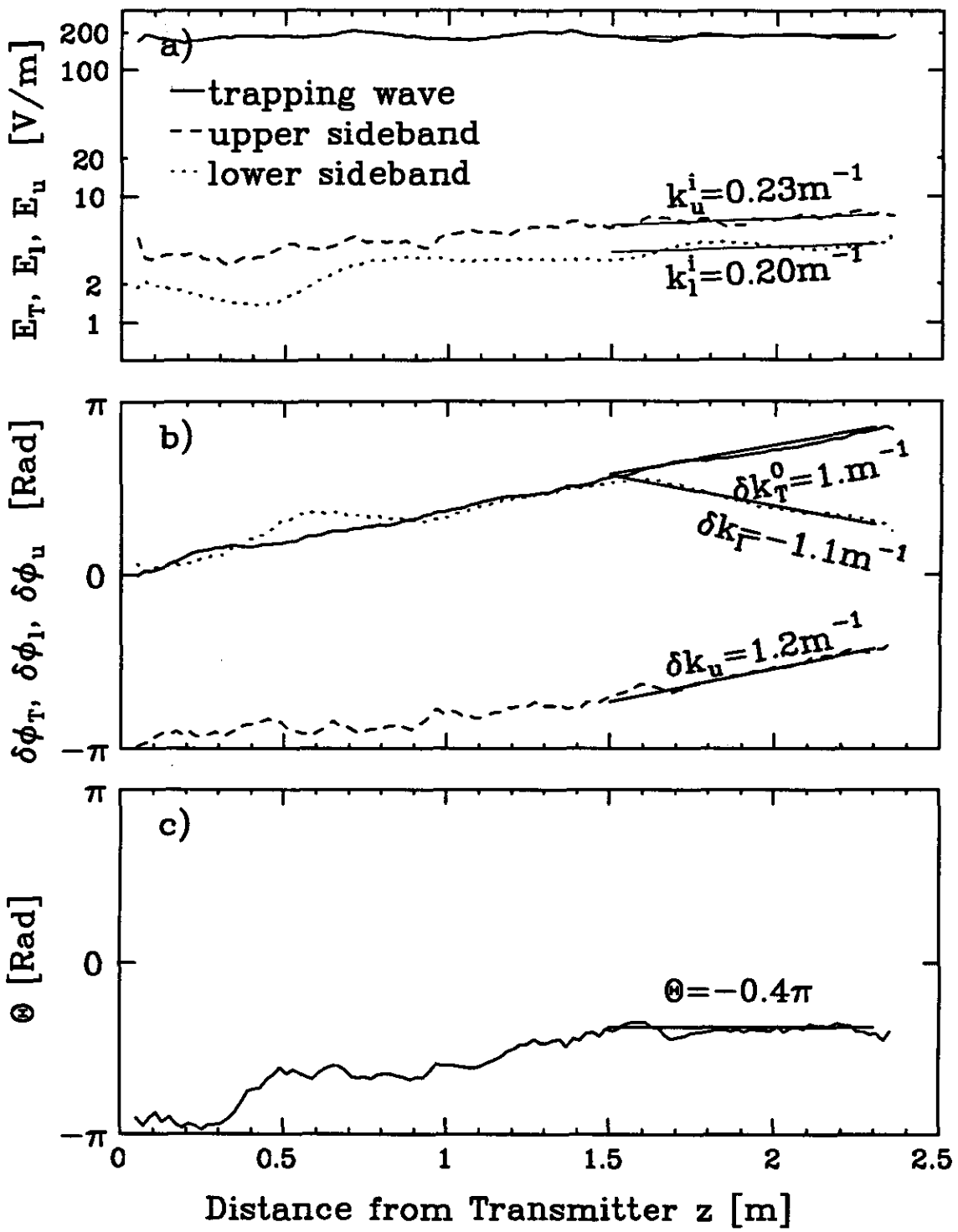

Figure 4.5: Spatial evolution of the growing sidebands, phases shifts and modulational phase (thick lines). Straight line fits (thin lines) between $z = 1.5$m and $z = 2.3$m. The trapped particle state is the same as in figure 4.1. The sideband frequency separation is $\Delta f_{sb} = 14.06$ MHz and $\alpha(z = 0) = 1.$, $\Theta(z = 0) = \pi$ (same as figure 4.4).

phase shift of the sidebands is also linear, therefore their wavenumber changes are also spatially constant, $\delta k_l \approx -1.1\text{m}^{-1}$, $\delta k_u \approx 1.3\text{m}^{-1}$. We show the linearity of the phase shifts by the good fit to straight lines between $z = 1.5$ m and $z = 2.35$ m. In figure 4.5c we see that the modulational phase is spatially constant with $\Theta \approx -0.4\pi$.

Dependence on $\Theta(z = 0)$ and $\alpha(z = 0)$

We find that the initial evolution of the sidebands depends on the initial value of the modulational phase and the sideband amplitude ratio, near the end of the interaction region, however, the values of the sideband growth rates, amplitude ratio, wavenumber change and modulational phase are independent from the values of $\alpha(z = 0)$ and $\Theta(z = 0)$.

In Figure 4.6 we show the spatial evolution of the sidebands for different launch values of the modulational phase $\Theta(z = 0)$ but constant initial sideband amplitude ratio $\alpha(z = 0) = 1$. Figure 4.6a shows the evolution of the sideband amplitudes for an initial value of the modulational phase $\Theta(z = 0) = 0.$, but the same value $\alpha(z = 0) = 1$. The trapped particle state is the same and the sideband frequency separation are the same as in figure 4.5. The initial conditions correspond to an amplitude modulated wave. Even though the initial evolution if different, the growth rates of the sidebands are approximately the same after $z \approx 1.5$m. Straight line fits yield growth rates of $k_l^i = 0.19\text{m}^{-1}$ and $k_u^i = 0.22\text{m}^{-1}$, $\alpha \approx 0.15$. They approximately agree with the previously obtained values. Figure 4.6b shows the measured phase shifts. They are approximately linear with distance for $z > 1.5$m and the changes of their wavenumbers agree with the previous values, $\delta k_l = -1.1\text{m}^{-1}$, $\delta k_u = 1.1\text{m}^{-1}$. In this case the value of the modulational phase $\Theta(z = 0)$ was changed by changing the initial phase of the lower sideband ϕ_l^0. Had we have changed any other phase such that the modulation phase still was $\Theta(z = 0) = 0$, then the

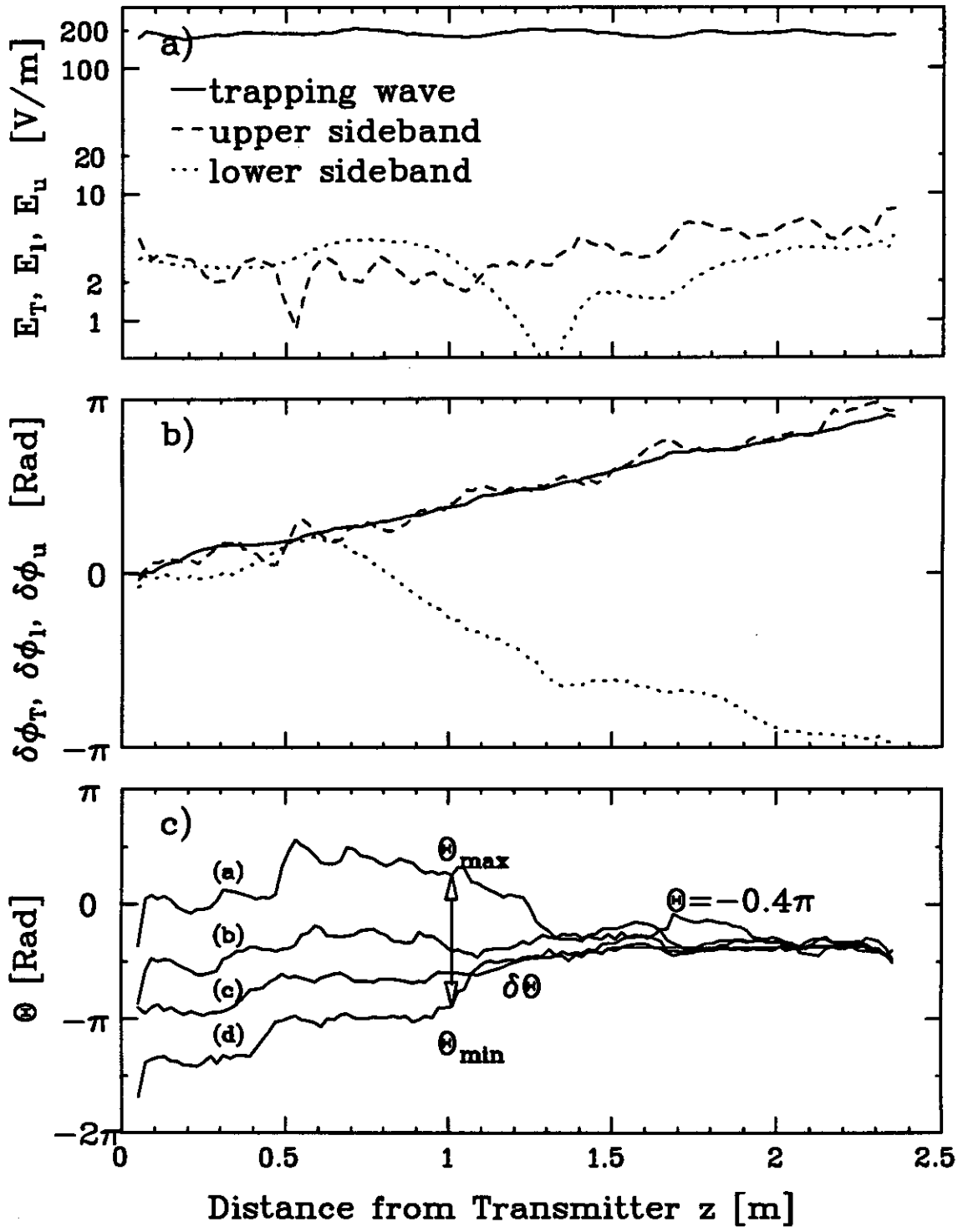

Figure 4.6: Evolution of the sidebands for different values of $\Theta(z=0)$. a), b): $\Theta(z=0)=0., \alpha(z=0)=1.$, c) $\Theta(z=0)$ =0, $\pi/2, \pi, 3\pi/2$. The trapped electron state and the sideband frequency separation are the same as in figure 4.5.

evolution of the sideband amplitudes and phases would have been the same, safe an offset in the sideband phases. Figure 4.6c shows the evolution of the modulational phase for this case (thick line, labeled "(a)") and for three different initial values. The case labeled "(c)" corresponds to the frequency modulated case shown before in figure 4.5.

In Figure 4.7 we show the spatial evolution of the sidebands for different launch values of the amplitude ratio $\alpha(z = 0)$ but the same modulational phase $\Theta(z = 0)$. Figure 4.7a shows the evolution of the sideband amplitudes for $\alpha(z = 0) = 1$, 2 and 4. and modulational phase $\Theta(z = 0) = 0$. The trapped particle state is the same and the sideband frequency separation are the same as in figure 4.5. Even though the initial evolutions are different, the growth rates of the sidebands are approximately the same after $z \approx 1.5$m. Straight line fits yield growth rates that approximately agree with the previously obtained values. Figure 4.7b shows the measured phase shifts. They are approximately linear with distance for $z > 1.5$m and the changes of their wavenumbers agree with the previous values, $\delta k_l = -1.1\text{m}^{-1}$, $\delta k_u = 1.1\text{m}^{-1}$. In figure 4.7 we see that also the modulational phase changes again to the same final value as before.

These measurements are easily explained within the framework of the KDS theory. At $z = 0$m different sideband normal modes are excited. The growing sideband normal mode with its particular phase and amplitude relationship outgrows the other modes, becomes dominant, and finally emerges as the only measured mode. This mode is characterized by a certain value of the modulational phase, and also by a certain ratio of the sideband amplitudes, growth rates and wavenumber shifts. This description presumes that the trapped particle state already exists at $z = 0$m. In our experiment, however, it first needs to be established. Therefore the initial evolution of the sidebands is not simply a superposition of growing and non-growing

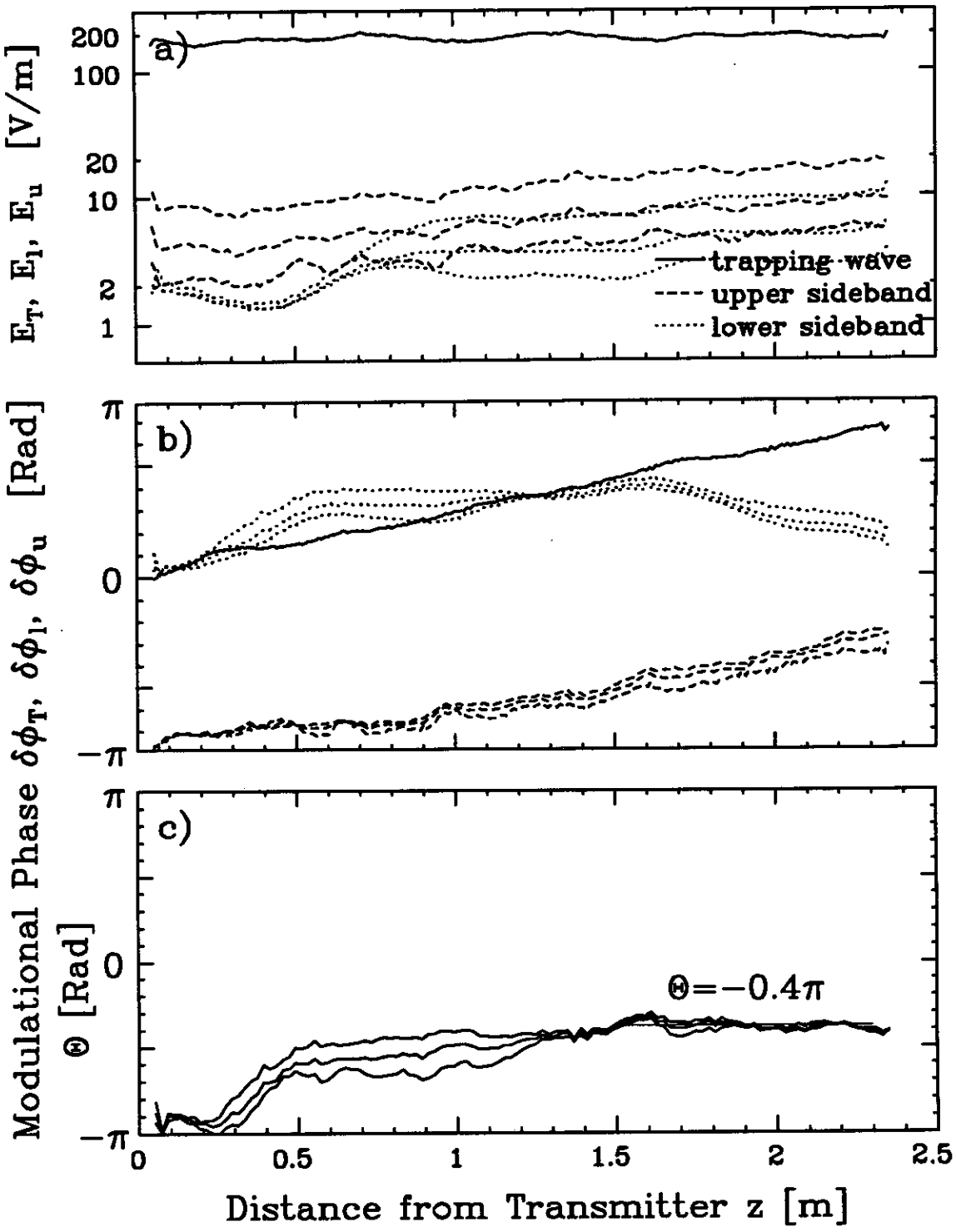

Figure 4.7: Sidebands for different amplitude ratios $\alpha(z = 0) = 1, 2, 4$ and $\Theta(z = 0) = \pi$. The beam parameters are the same as in figure 4.5.

sideband normal modes.

Theory suggests that the modulational phase is to be treated on equal footing with the sideband growth rates, their wavenumber shifts and the amplitude ratio. We did not find consistent evidence that the modulational phase has importance beyond the regime of linear perturbations of the electron orbits. However, of the four quantities that describe a sideband normal mode of the KDS dispersion relation, the modulational phase is the most readily derivable quantity, and we use it in the following as an indicator of whether the macro-particle model is applicable or not.

Non-growing sideband modes

There can be launched waveforms with particular values of the modulational phase and sideband amplitude ratio for which the growing sideband normal mode is excited much less than the non-growing sideband normal modes. Then the growing mode may not have outgrown the other modes, even at the end of the interaction region. The spatial evolution of such a case is shown in figure 4.8. The beam parameters and the trapped electron state are the same as in figures 4.5, but the initial values of the modulational phase and amplitude ratio have been chosen differently. For these values the sidebands do not grow, and the modulational phase does not evolve to the same final and constant value as in the other cases (figures 4.6 and 4.7). Similarly the sideband amplitude ratio and the wavenumber shifts are not constant close to the end of the interaction region.

Modulational phase for different sideband frequencies

In order to show whether the modulational phase evolves to the same values for different initial conditions at other sideband frequencies, we define the upper and the lower limits of the measured modulational phase, $\Theta_{max}(z)$ and $\Theta_{min}(z)$, and its

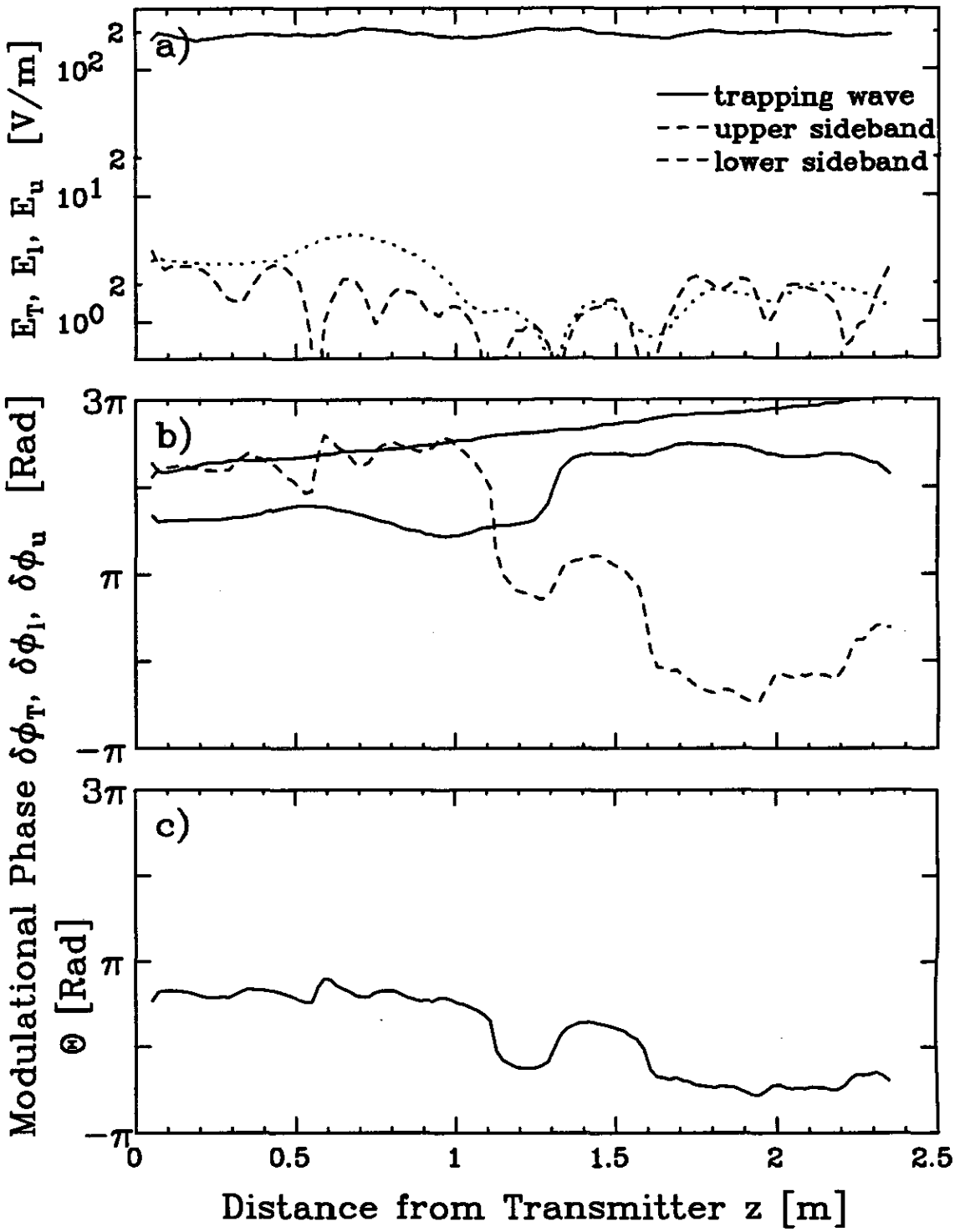

Figure 4.8: Evolution of a non-growing sideband mode found for $\alpha(z = 0) = 1$, $\Theta(z = 0) = \pi/2$. The experimental parameters are the same as in figure 4.5.

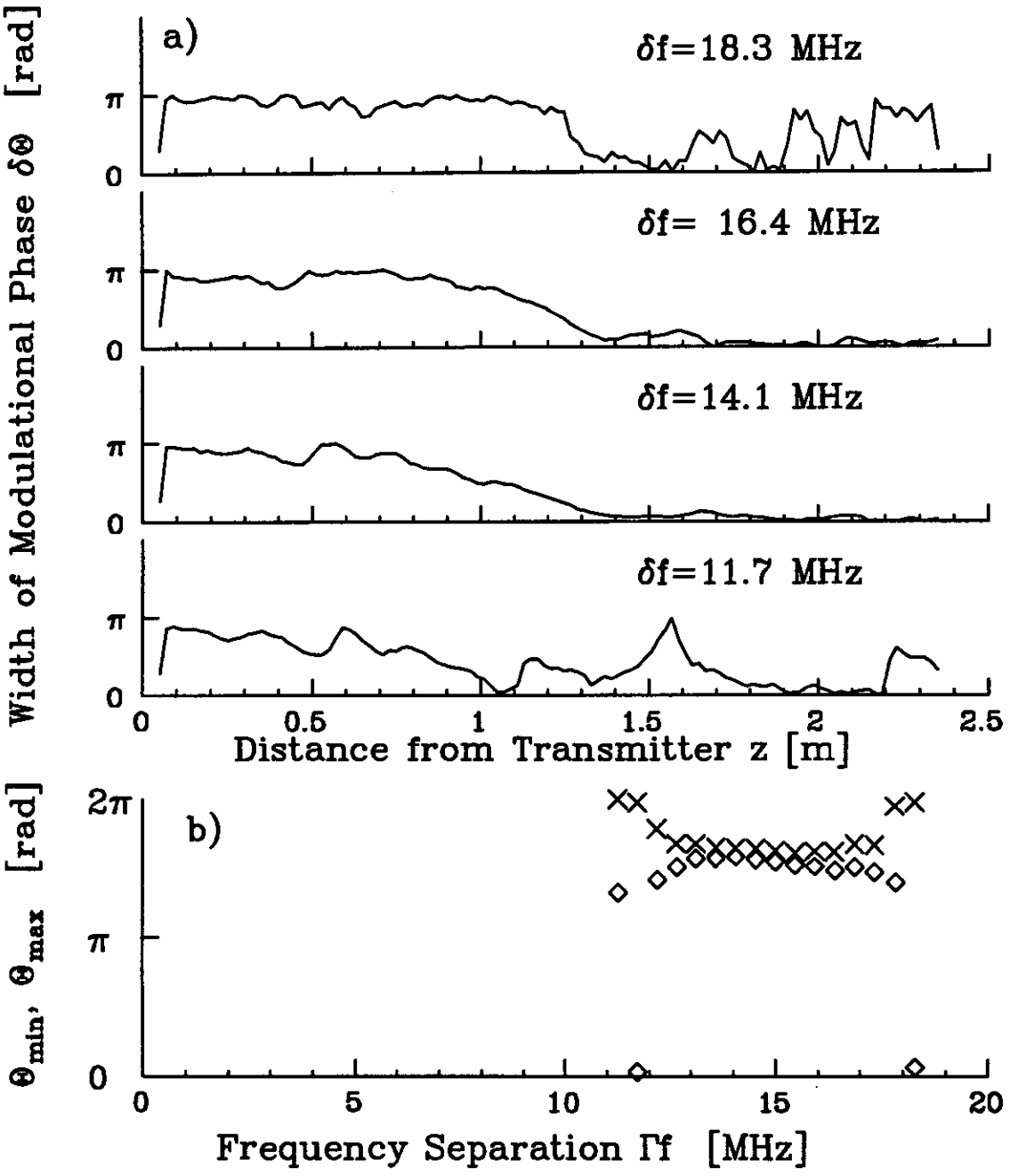

Figure 4.9: a)Width of the modulational phase evolution for different sideband frequency separations δf_{sb}. b) Values of $\Theta_{max}(\times), \Theta_{min}(\diamond)$ for different sideband frequency separations δf_{sb}.

"width" $\delta\Theta(z) \equiv \Theta_{max}(z) - \Theta_{min}(z)$, for four different initial values $\Theta(z = 0)$ spread equally over 2π. The value of $\alpha(z = 0)$ is chosen such that the growing sideband normal mode has outgrown the other modes by the end of the interaction region , typically $\alpha = 2$. In figure 4.6c $\Theta_{min}(z = 1\text{m})$, $\Theta_{max}(z = 1\text{m})$ and $\delta\Theta(z = 1\text{m})$ are indicated for clarification. Figure 4.9a shows the spatial evolution of $\delta\Theta(z)$ for a few different sideband frequency separations δf_{sb}. For sideband frequency separations from $\delta f_{sb} = 12.5$ MHz to $\delta f_{sb} = 17.0$ MHz the width of the modulational phase $\delta\Theta(z)$ becomes very small, i.e. the modulational phase approaches the same final value Θ^{∞} independent of its initial values. We call this region of frequencies a "resonance" where the growing sideband normal mode has outgrown the non-growing modes. We define a resonance region of the modulational phase if $\delta\Theta(z = 2\text{m}) < 2\pi/10$ [1] and compare the measured values of α, $\delta k_{l,u}$, $k^i_{l,u}$ and Θ in this region with the theoretical predictions in the next section . Figure 4.9b shows the values of $\Theta_{max}(z = 2.1\text{m})$ and $\Theta_{max}(z = 2.1\text{m})$ versus the sideband frequency separation δf_{sb}. For sideband frequency separations from $\delta f_{sb} = 12.5$ MHz to $\delta f_{sb} = 17.0$ MHz the final value of the modulational phase is relatively well defined. It shows a slight frequency dependence.

Resonance for different trapping wave amplitudes

We measure the region of sideband frequency separations for which we find a modulational phase resonance for different trapping wave amplitudes. Trapped electron states of different trapping wave amplitude are created by simultaneously changing the launch amplitude of the trapping wave, the beam current and the applied dc electric field. In all cases the trapping wave amplitude is spatially constant, with deviations smaller than 1.5 dB near the end of the interaction region. These trapped electron states are investigated by launching sidebands at different frequency

[1] For frequency separations δf_{sb} where we do not find a resonance, we cannot conclude that no growing sideband mode exists, but only that it has not outgrown the other modes.

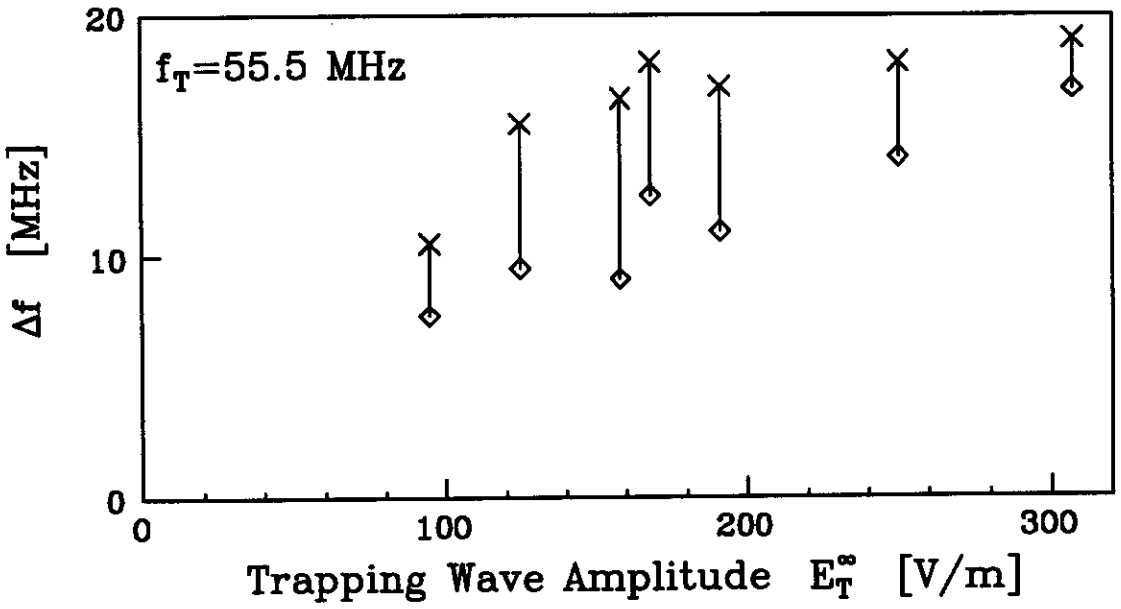

Figure 4.10: Frequency separation of sideband frequencies that show resonance versus trapping wave amplitude

separation from the trapping wave and with different initial values of the modulational phase. In figure 4.10 we plot the largest and the smallest sideband frequency separation δf_{sb} for which we still observe a resonance of the modulational phase for different trapping wave amplitudes. We find that the frequency separation of the resonance is increasing with trapping wave amplitude.

4.3.3 Comparison with Computer Simulations

In figure 4.11 we compare our experimental measurements with our computer simulations. We find fairly good agreement.

The nonlinear, multi-wave TWT equations are reviewed in appendix F. We solve them numerically by integration with the initial values by the measured initial amplitudes and phases. The frequency ratio of the upper sideband to the trapping wave frequency of the experiment is well approximated by a rational number of small denominator l (see appendix F). In the integration it is necessary to use the actual local wavenumbers and damping rates of the beamless helix in order to obtain

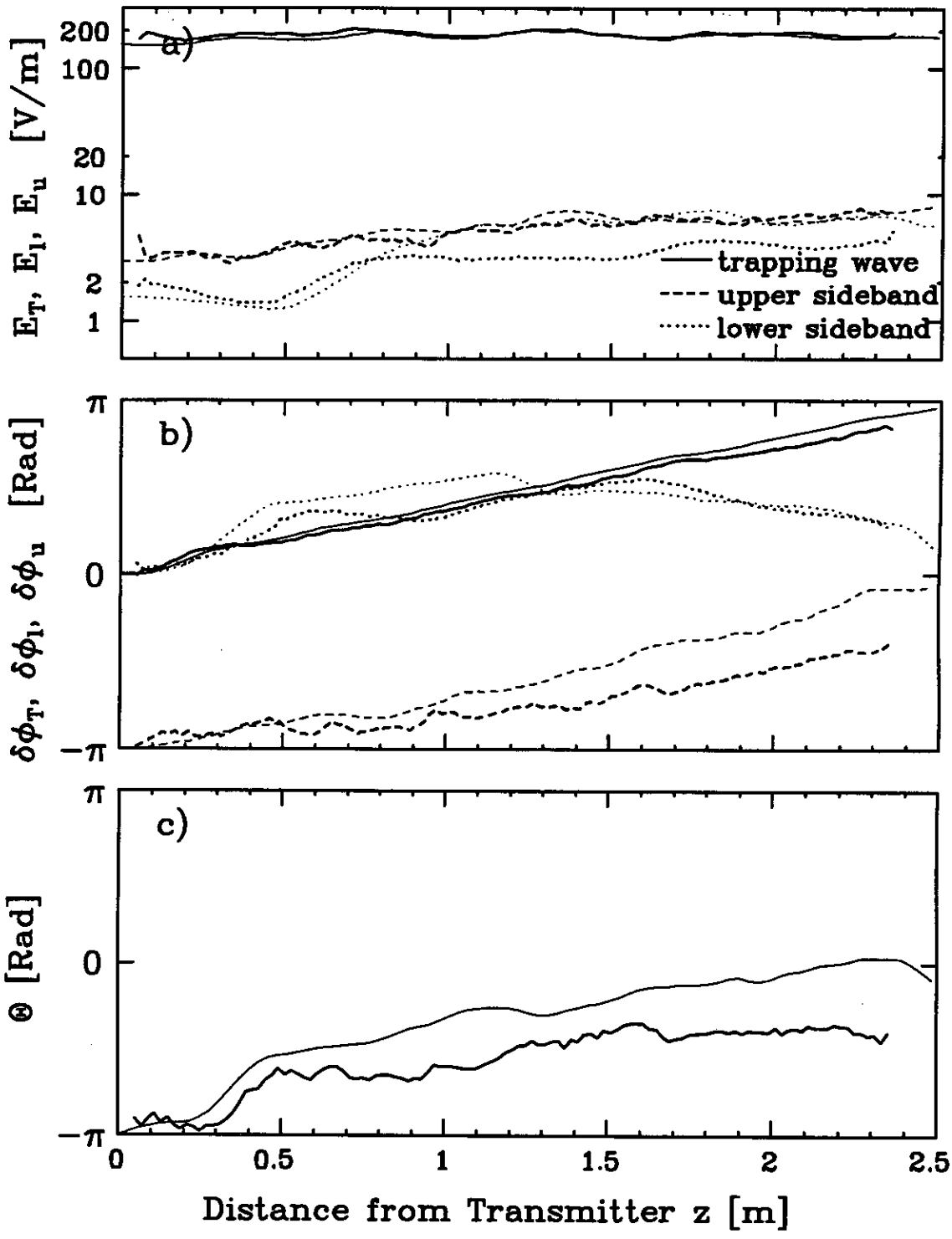

Figure 4.11: Spatial evolution of the growing sidebands, phases shifts and modulational phase (thick lines). Straight line fits (thin lines) between $z = 1.5$m and $z = 2.35$m. The trapped particle state is the same as in figure 4.1. The sideband frequency separation is $\delta f_{sb} = 14.06$ MHz and $\alpha(z = 0) = 1.$, $\Theta(z = 0) = \pi$ (same as figure 4.4).

good agreement. The plasma frequency reduction factor is obtained from figure 2.5. We find that the wavenumber change of the trapping wave is very dependent on the space-charge term, i.e. the plasma frequency reduction factor P_q. We sometimes need to adjust P_q by as much as 25% from its value determined from the fit of figure 2.5 in order to obtain the same wavenumber shift as in the experiment. In addition, the sideband amplitudes and trapping wave amplitudes are sometimes adjusted within the experimental error. Typically we solve the equations with 100 beam particles per wave trough.

The thick lines in figure 4.11 are the experimental measurements shown before. The thin lines are the results of our computer calculation. The calculated amplitudes agree reasonably well with the measurements of the sideband amplitudes. The calculated phase shifts and the modulational phase do not well agree with the measurements. However, the computer calculations also show the modulational phase resonance.

4.3.4 Comparison with the KDS Model

In this section we compare the experimentally determined properties of the growing sideband mode with the predictions of the macro-particle model and with computer simulations of the evolution. In general, we find qualitative agreement between the predictions of the macro-particle model and the experiment and slightly better quantitative agreement between the computer simulations and experiment. In particular, we find for the

- **location of the resonance** that the macro-particle model predicts the fastest growing sidebands at larger sideband frequency separations than the experiment,

- **properties of the growing sideband normal mode** that observed growth rates, wavenumber shifts and modulational phase are smaller than predicted,
- **dependence on the helix dispersion** that we experimentally observe a modulational phase resonance only if the required wavenumber changes of the sidebands are small, whereas there is no such requirement in the sideband dispersion relation,
- **difference wave** (wave at the frequency difference of upper sideband - trapping wave) no coupling to the sidebands, whereas the macro-particle model predicts coupling.

Location of the resonance

According to the KDS macro-particle model the growing sideband modes have the maximal growth rates if the sideband resonance condition (4.1) is fulfilled. Tsunoda and Malmberg found this for a case where it was assumed that the group velocity and the wave-beam coupling of all three waves was constant [63]. We use this relation to obtain a value of the bounce frequency of the trapped electron distribution in the experiment according to

$$f_B^{u,l} = \mid f_{u,l} - v_T^{\infty} k_{u,l} \mid, \tag{4.22}$$

where we use the measured values of the sideband wavenumbers. We calculate the "sideband bounce frequency" $f_B^{u,l}$ for the sidebands for which we find the maximum growth rate. We compare it with the "modified bounce frequency" f_B^{dc} of a trapped macro-particle trapped when a dc electric field is applied. Its value is calculated from equation (4.12) for the electric field amplitude of the trapping wave E_T^{∞}. In figure 4.12 the two bounce frequencies are compared with one another. The experimentally determined bounce frequencies are smaller than the predictions from the trapped

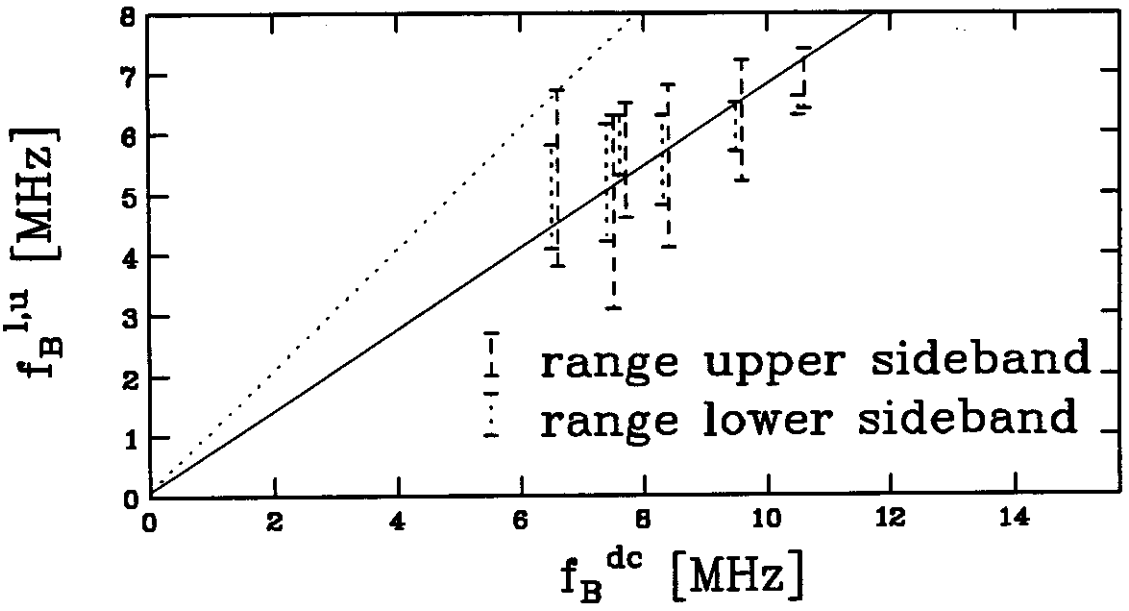

Figure 4.12: Experimental versus theoretical bounce frequency. Theory: dotted line; best fit to experiments: solid line.

macro-particle model. This is probably due to the trapped particle distribution having finite extend in phase-space, as seen in figure 4.2, so that it is not reasonable to use a harmonic trapping potential. Experimentally we find that

$$f_B^{l,u} \approx 0.7 * f_B^{dc} \tag{4.23}$$

Properties of the growing sidebands

The growth rates and wavenumbers shifts of the sidebands are obtained by fitting straight lines to the measurements of the logarithms of the amplitudes and to the phase shifts; the values of the modulational phase Θ and amplitude ratio α are the spatial averages of the quantities within the region where the modulational phase is equal and fairly constant for different initial values. We fit the straight lines to the case where the amplitudes of the sidebands are the largest, so that the other (non-growing) sideband modes can be assumed to be very small. The crosses

in figure 4.13 show the experimental measurements.

We use the same procedure to obtain the properties of the growing sidebands for the computer simulations. The calculated values are shown as diamonds in figure 4.13. The frequencies are normalized to the trapping wave frequency, i.e. the data of the lower sideband is shown on the left side of the plot, and the data of the upper sideband is shown on the right side of the plot. In the model the k^i, Θ and α are the same for lower and upper sideband frequency, in the experiment only Θ and α are necessarily the same for upper and lower sideband.

The predictions of the sideband dispersion relation of the macro-particle model are obtained by numerically finding the growing solutions of equation (4.13) for a given frequency. We find two growing solutions; in figure 4.13 we only plot the solution with the larger growth rates. The modified bounce frequency, the beam plasma frequency of the trapped electrons and the phase velocity of the trapping wave are obtained from the experimental measurements as described in section 4.3.1. The dashed line shows the frequencies of the sidebands as expected from the sideband resonance condition (4.1). It agrees well with the maximum growth rate of the upper sideband of the sideband dispersion relation. The horizontal dashed line in the top plot is wavenumber shift of the trapping wave. We see that for maximum growth rate, the upper sideband wavenumber change equals the wavenumber change of the trapping wave (intersection of the two dashed lines).The experimentally determined properties do not agree with the prediction of the dispersion relation. The wavenumber shifts are too small, but are in the predicted direction. The growth rates are too small by at least a factor of 2.5. The modulational phase has the same frequency dependence but is more negative. Only the sideband amplitude ratio of the experiment for the sidebands with largest growth rates agrees with the predictions.

If we artificially reduce the bounce frequency and the trapped electron ratio

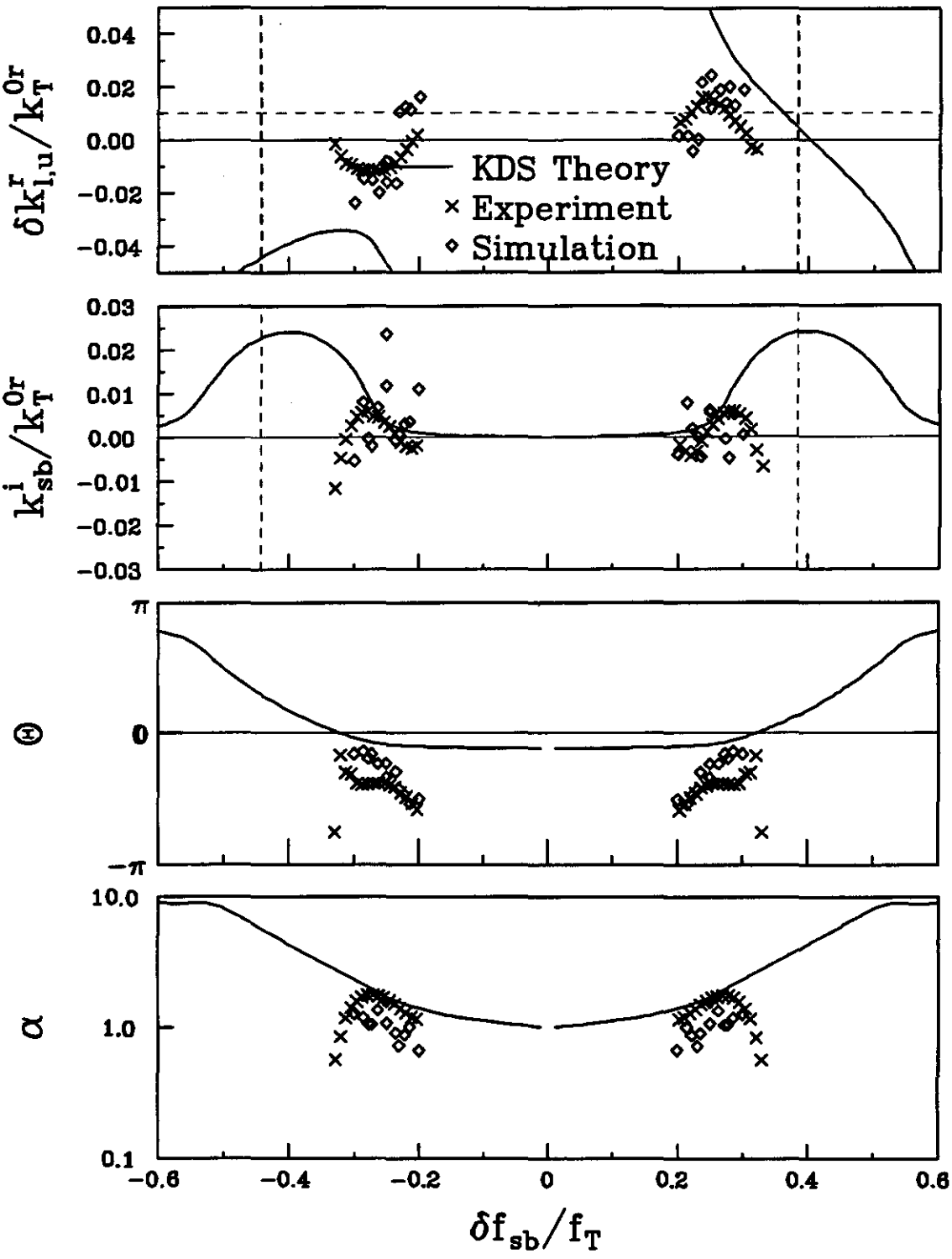

Figure 4.13: Comparison of the of the growing sideband mode: Experiment, particle-simulations and KDS theory. The experimental parameters are the same as in figure 4.5. The parameters used for the KDS sideband dispersion relation are: $k_T^{\infty}/k_T^{0r} = 1.01, \sigma = 0.6, \omega_B^{dc}/\omega_T = 0.15, \omega_p/\omega_T = 0.033$.

we obtain a slightly better agreement in 4.14. This reduction might by justified by arguing that only the particles trapped near the bottom of the well are involved in the sideband instability and that some adjustments have to be made for the sinusoidal, rather than harmonic trapping potential. In figure 4.14 we plot the growing sideband modes for $\sigma = 0.3$ and $\omega_B^{dc}/\omega_T = 0.1$.

Dependence on the dispersion relation

The sideband dispersion relation of the macro-particle model has growing solutions for a wide range of background (helix) dielectric functions $\epsilon^h(\omega, k_\omega)$. In particular, there is no requirement on the group velocity of the waves in regions where one looks for sidebands. As was pointed out before, a characteristic property of all solutions of the sideband dispersion is that

$$2k_T^\infty - k_u^r - k_l^r = 0, \tag{4.24}$$

which makes the modulational phase spatially independent. Notice that, in contrast, the background dispersion does not have the same property, i.e. in general

$$2k_T^\infty - k_u^{0r} - k_l^{0r} \equiv \Delta k \neq 0. \tag{4.25}$$

If $k_T^\infty = k_T^{0r}$ then the expression on the l.h.s. vanishes only if the group velocity is constant. Therefore in the experiment, in order for the modulational phase to become spatially independent, the wavenumbers of the sidebands have to change by a total amount given by Δk. Obviously, this amount depends on the trapping wave frequency, the sideband frequency separation and the wavenumber shift of the trapping wave $\delta k_T^\infty = k_T^\infty - k_T^{0r}$.

In the figure 4.15 we plot $\Delta k/k_T^{0r}$ for a particular value of $\delta k_T^\infty = 0.9\mathrm{m}^{-1}$ in form of contour lines for various values of the trapping wave frequency f_T and the sideband frequency separation δf_{sb}. The crosses mark experiments where we

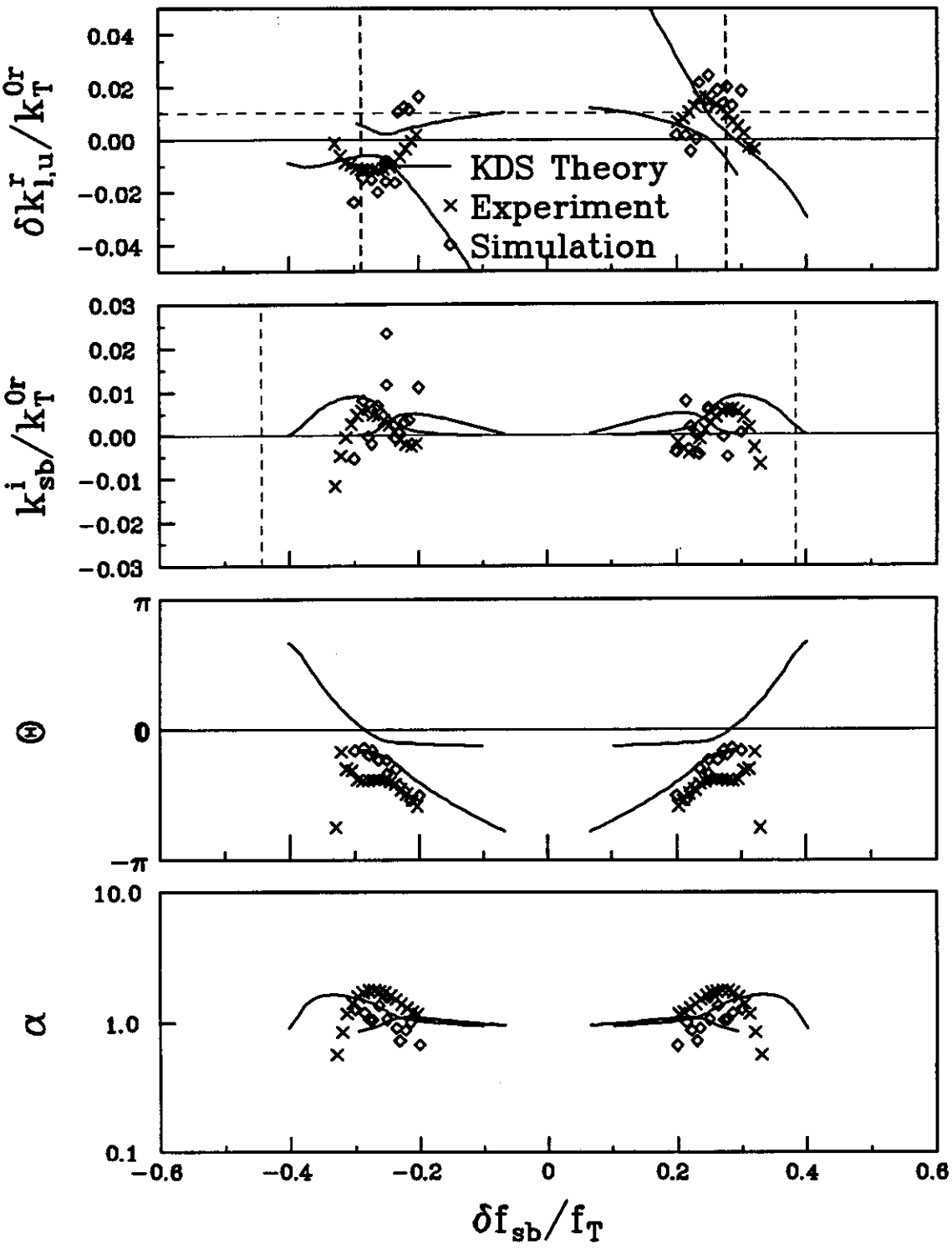

Figure 4.14: Comparison of the of the growing sideband mode: Experiment, particle-simulations and KDS theory. The experimental parameters are the same as in figure 4.5. The parameters used for the KDS sideband dispersion relation are: $k_T^{\infty}/k_T^{0r} = 1.01, \sigma = 0.3, \omega_B^{dc}/\omega_T = 0.10, \omega_p/\omega_T = 0.033$.

have observed a resonance of the modulational phase, i.e. the sidebands in these experiments adjusted their wavenumbers such that equation (4.24) was fulfilled. The crosses occur only where the required total wavenumber change is small. Since a spatially constant modulational phase is equivalent to phase-lock between the sidebands, we therefore find that we observe phase-lock only if the wavenumbers of the sidebands do not have to change much from the values given by the helix dispersion. In those cases where we do not observe phase-lock, the sidebands may still be growing, however, there will not be a region where the initial conditions are no longer important, and the growing sidebands do not form a sideband normal mode.

Evolution of the difference wave

Near the end of the interaction region, we not only observe the three launched waves but also nonlinear product waves. The strongest of those has a frequency equal to the frequency difference between the trapping wave and one of the sidebands. It is not phase-related to the other waves, and cannot be explained within the framework of the KDS model.

The spatial evolution of the "difference" wave is shown in figure 4.16 with a thick line. (For this case the sidebands evolve as shown in figure 4.5). Close to the transmitter the difference wave growth is rapid, but diminishes with distance. The thin line in figure 4.16 shows the calculated evolution of a computed case when four waves interact with the beam and the difference wave is launched with an initial amplitude 40 dB below the initial amplitude of the sidebands. The agreement between the computer simulations and the experiment is reasonably good.

An obvious extension of the KDS theory is to include the difference wave in the linear system of equations that describe the coupling between the different frequencies of the electric field in equation (E.6). This leads to a 3×3 rather than

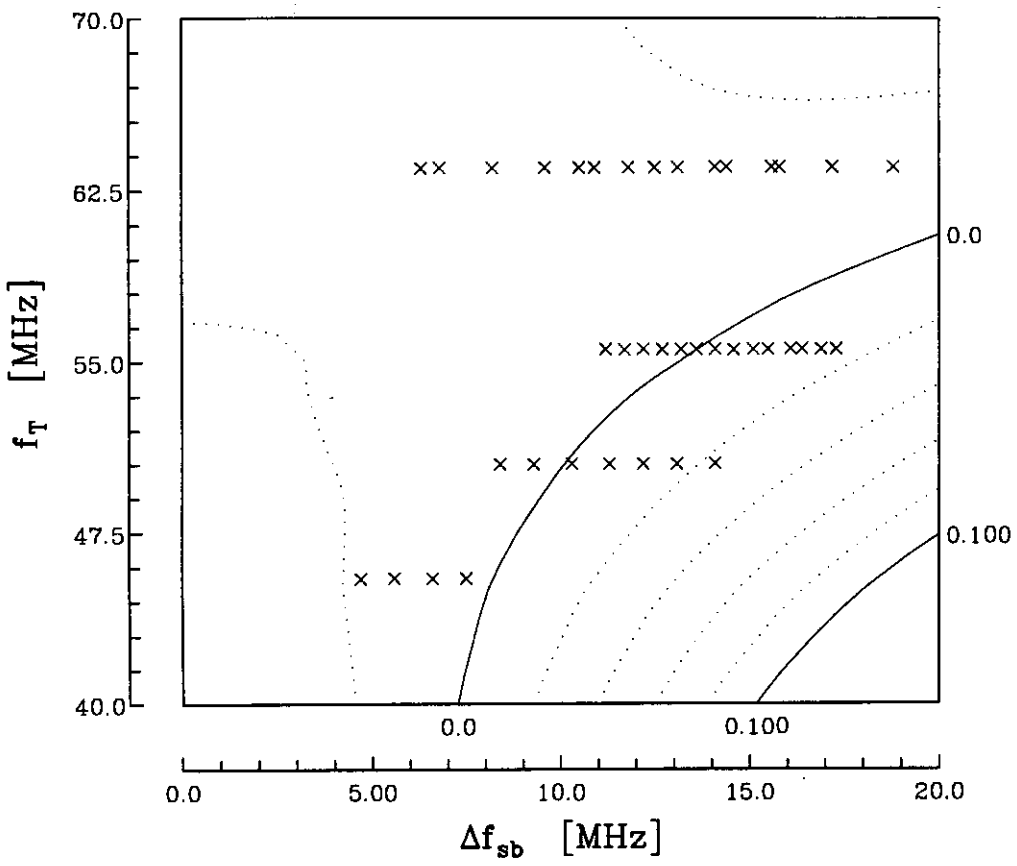

Figure 4.15: Contour plot of the cumulative wavenumber changes of the sidebands required to obtain a spatially independent modulational phase. The nonlinear wavenumber shift of the trapping wave is $\delta k_T^{\infty} = 0.9m^{-1}$. The crosses are experimental conditions for which the growing sideband mode with spatially constant modulational phase was observed.

a 2×2 matrix. Setting the determinant to zero yields a dispersion relation for the sidebands and the difference wave. For the sidebands, the growing solution is almost identical to the growing solution of the original dispersion relation. For the difference wave it predicts a growth rate that equals the growth rate of the sidebands, $k_D^i = k_l^i = k_u^i$, and a wavenumber shift such that not only $f_D + f_{lsb} = f_T$ but also $k_D + k_l^r = k_T^{\infty}$.

From figure 4.16 we find that the growth rate of the difference wave between $z = 1.5$m and $z = 2.3$m is $k_D^i \approx 0.3\text{m}^{-1}$, compared to $k_l^i \approx 0.2\text{m}^{-1}$. Its wavenumber

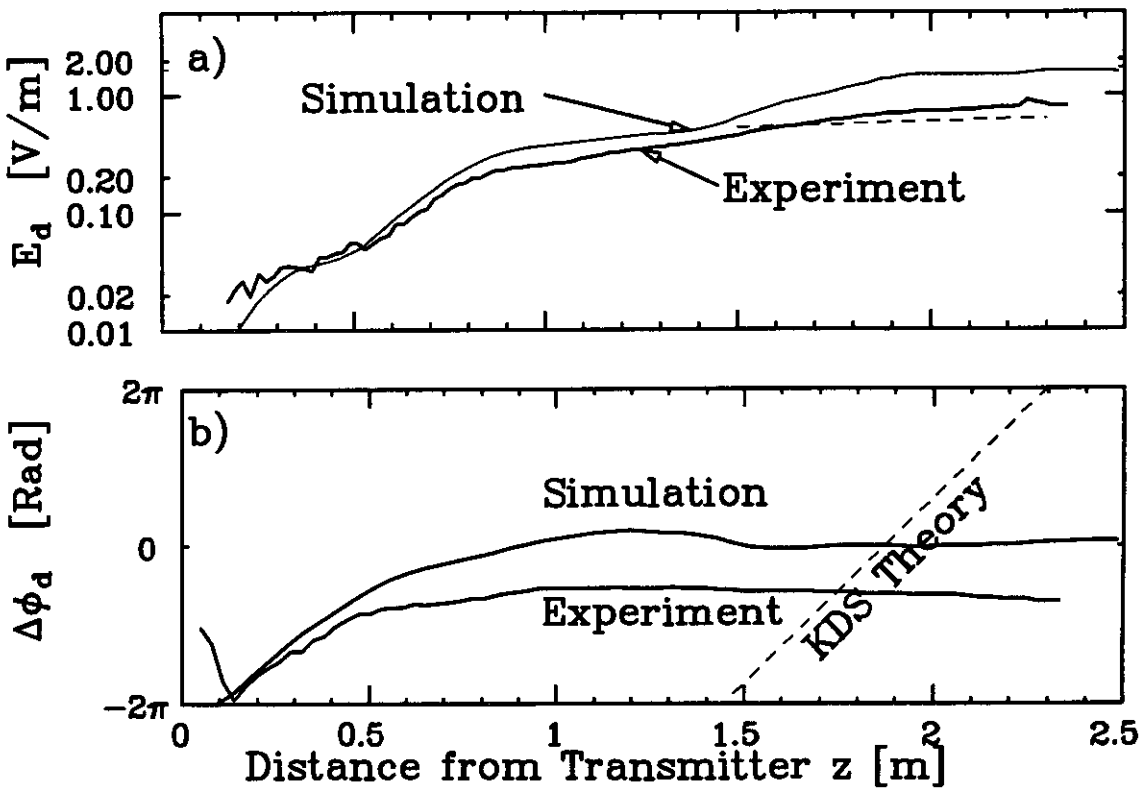

Figure 4.16: Evolution of the difference wave at $f = 14.06$MHz for four different values of the initial phase of the upper sideband. Equal patterns correspond to the same initial conditions. Experimental parameters are the same as in figure 4.5

shift is $\delta k_D^r \approx= 0.5\text{m}^{-1}$, compared to a predicted value of $k_T^\infty - k_l^r - k_D^{0r} \approx 16.8\text{m}^{-1}$. The predicted values of the growth rates and phase shifts from the macro-particle model are shown as dashed lines. We also find that its evolution is independent of the phases of either the upper or the lower sideband [2].

4.3.5 Single Particle versus Macro-Particle

This section compares the properties of the growing sidebands in computer simulations of idealized situations with the predictions of the KDS dispersion rela-

[2]Due to small nonlinear coupling of the launched waves in the launch circuitry the difference wave is launched together with the other waves. Its initial amplitude is at least 40 dB below the amplitude of the lower sideband and its initial phase is coupled to the lower sideband. This coupling only determines the initial phase; it does not extend into the nonlinear regime.

tion. Idealized means that we neglect space-charge effects, the spatial dependence of the wavenumbers and damping rates of the beamless helix and higher order correction in the beam-helix coupling (see appendix F). Otherwise the helix dispersion relation and its frequency dependent interaction impedance is used. The trapped electron states investigated are steady states that are the result of the interaction of an externally applied dc electric field with the trapped electrons as described in section 4.3.1. Steady states consisting of single macro-particles per potential trough of the trapping wave or consisting of distributions of trapped electrons are investigated. The first situation is the dynamical analog of the macro-particle model of Kruer, Dawson and Sudan. The second situation is our experiment without its peculiarities.

We find that for trapped macro-particles the properties of the growing sidebands agree well with the predictions of the KDS sideband dispersion relation. In the case of a trapped distribution of electrons, we find only qualitative, not quantitative agreement. Therefore we conclude that the discrepancy between our experimental results and the predictions of the macro-particle model are a reflection of the oversimplified description of the trapped particle distribution by a single macro-particle.

Macro-particle

In this subsection the evolution of the sidebands is studied for the case where each potential well of the trapping wave traps one macro-particle. This has already been studied for some cases by TM. In our situation the trapping wave is damped and a dc electric field is applied to the electrons. We find perfect agreement between the predictions of the modified KDS dispersion relation and the derived properties of the growing sidebands.

We first establish that we obtain a dynamic equilibrium for the case where

a dc electric field is applied to the macro-particle and the trapping wave is damped. Depending on the initial position of the macro-particle with respect to the wave potential, damped trapping oscillations are observed for small distances. Damped trapping oscillations occur also for the case where the macro-particle is put at the bottom of the wave trough and the initial macro-particle velocity is adjusted to the wave phase velocity of the beamless helix. The oscillations then arise because the final steady state requires the wave to have a different phase velocity, so also the macro-particles have to adjust their velocity. After the oscillations have subsided, the values of the final amplitude, E_T^∞, the shift in wavenumber, δk_T^∞, and the offset of the macro-particle position from the minimum of the trapping wave potential $\Delta\Theta$ agree with the values derived from (4.8), (4.9) and (4.11) with $\sigma = 1$.

In the simulation two sidebands symmetric in frequency to the frequency of the trapping wave are launched at low amplitudes at the same position as the trapping wave. After some initial transition region both sidebands grow exponentially at the same rate.

In figure 4.17 the asymptotic wavenumber shifts $\delta k_{l,u}^r$, growth rates, $k_{l,u}^i$, modulational phases, Θ, and sideband amplitude ratios, α, are compared with the properties of the growing sideband mode calculated from the sideband dispersion (4.13) for different sideband frequencies. The agreement between the model and the computer simulation is expectedly good. Two growing branches of sideband normal modes are found in the dispersion relation. The results of the computer simulation agree with the branch that has the larger growth rate.

A few properties of the growing sideband mode deserve to be pointed out. The vertical dashed lines in the plot of the growth rates in figure 4.17b mark the sideband frequencies for which the sideband resonance condition (4.1) is fulfilled. It agrees fairly well with the frequency where the upper sideband has maximum growth

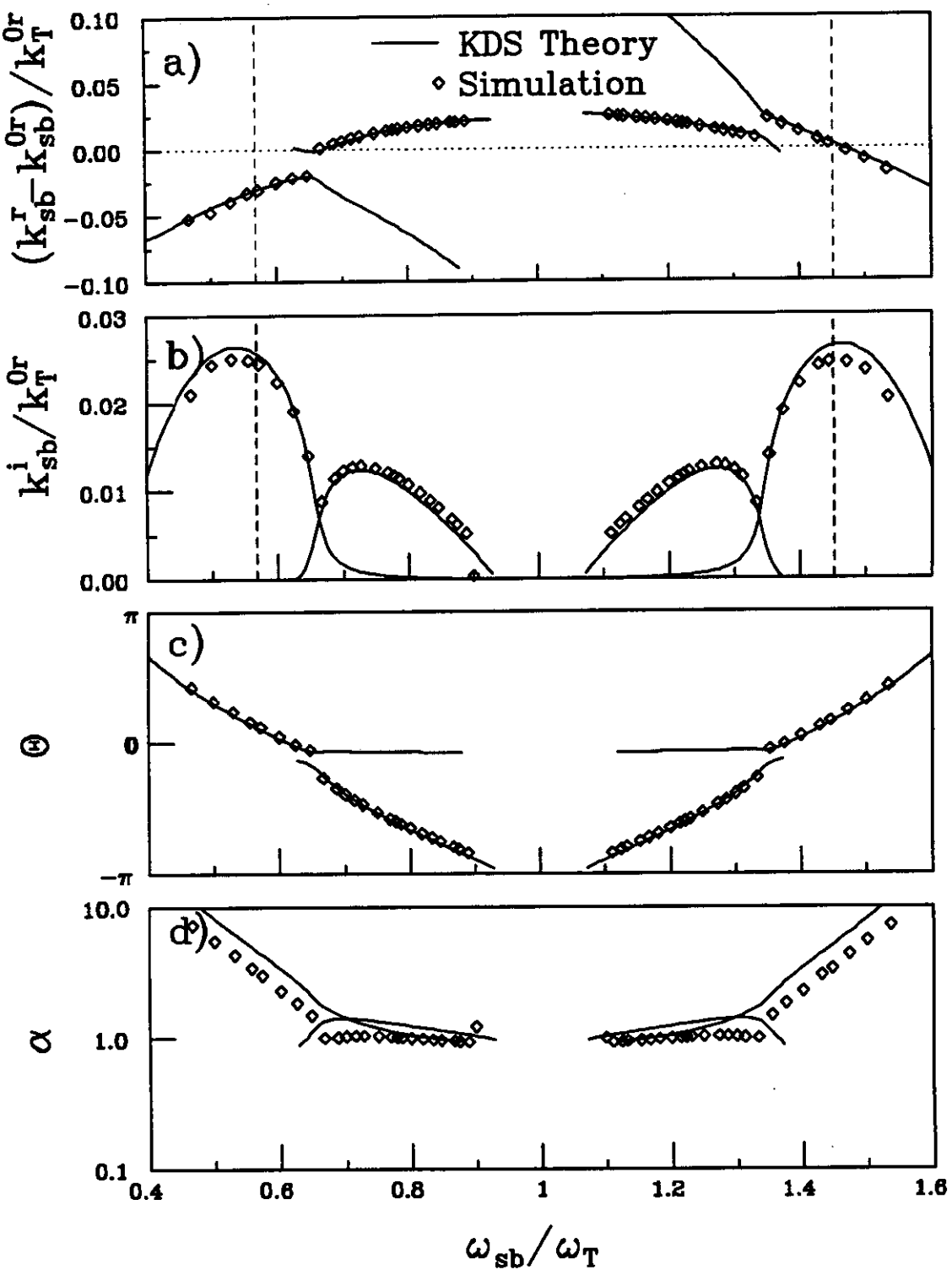

Figure 4.17: Properties of growing sideband mode for trapped macro-particle. The trapping wave frequency is $f = 55.5$ MHz as in figure 4.5. $\sigma = 1$, $\omega_b/\omega_T = 0.041$, $\omega_p/\omega_T = 0.15$, $k_T^{\infty}/k_T^{0r} = 1.015$

rate. The slight asymmetry of the frequencies where the sideband resonance occurs has two reasons. Firstly, the trapping wave phase velocity has been lowered due to the interaction with the trapped macro-particles; secondly, the helix dispersion relation does not have constant group velocity in this frequency regime. It is seen that maximal growth rates of the sidebands occur where the upper sideband has a very small shift in wavenumber, whereas the lower sideband adjusts its wavenumber more to ensure that the modulational phase is constant in space for the growing solution. For sideband frequencies adjacent to the resonance, the wavenumber shifts are such as to reduce the mismatch of the Doppler-shifted sideband frequency with the bounce frequency. The final value of the modulational phase is not zero, but rather shows a dependence on sideband frequency. Figure 4.17d also shows the frequency dependence of the amplitude ratio of the sidebands. For all frequencies the amplitude of the upper sideband is higher than the amplitude of the lower sideband.

Trapped distribution of electrons

In this section simulations of the growing sideband mode are shown for the more realistic situation where a continuous electron beam is trapped by a large amplitude damped wave with external dc electric field. The wave eventually reaches a state of approximately constant amplitude and wavenumber shift.

As in the previous case, two sidebands with frequencies symmetric to the frequency of the trapping wave are excited simultaneously with the trapping wave at the beginning of the interaction region. The growth of the sidebands is approximately exponential in the region where the trapping wave amplitude is constant. As in the experiment we measure the parameters $k^i_{l,u}$, $\delta k^r_{l,u}$, θ, α that describe the growing sideband mode in the region where they have become spatially constant (the modulational phase is spatially dependent which causes the large changes for differ-

ent sideband frequencies). They are shown as diamonds in figure 4.18. We compare these values with the growing solution of the sideband dispersion relation for the parameters ω_B^{dc}, v_T^{∞}, σ (obtained directly from the number of trapped particles in the simulation). The growing solution is shown as lines in figure 4.18. Similar to the experiment we obtain no quantitative, merely qualitative agreement. Thereby we have established that the cause of the disagreement are not the peculiarities of the experiment (space-charge, spatially dependent dispersion relation) but the macro-particle assumption itself.

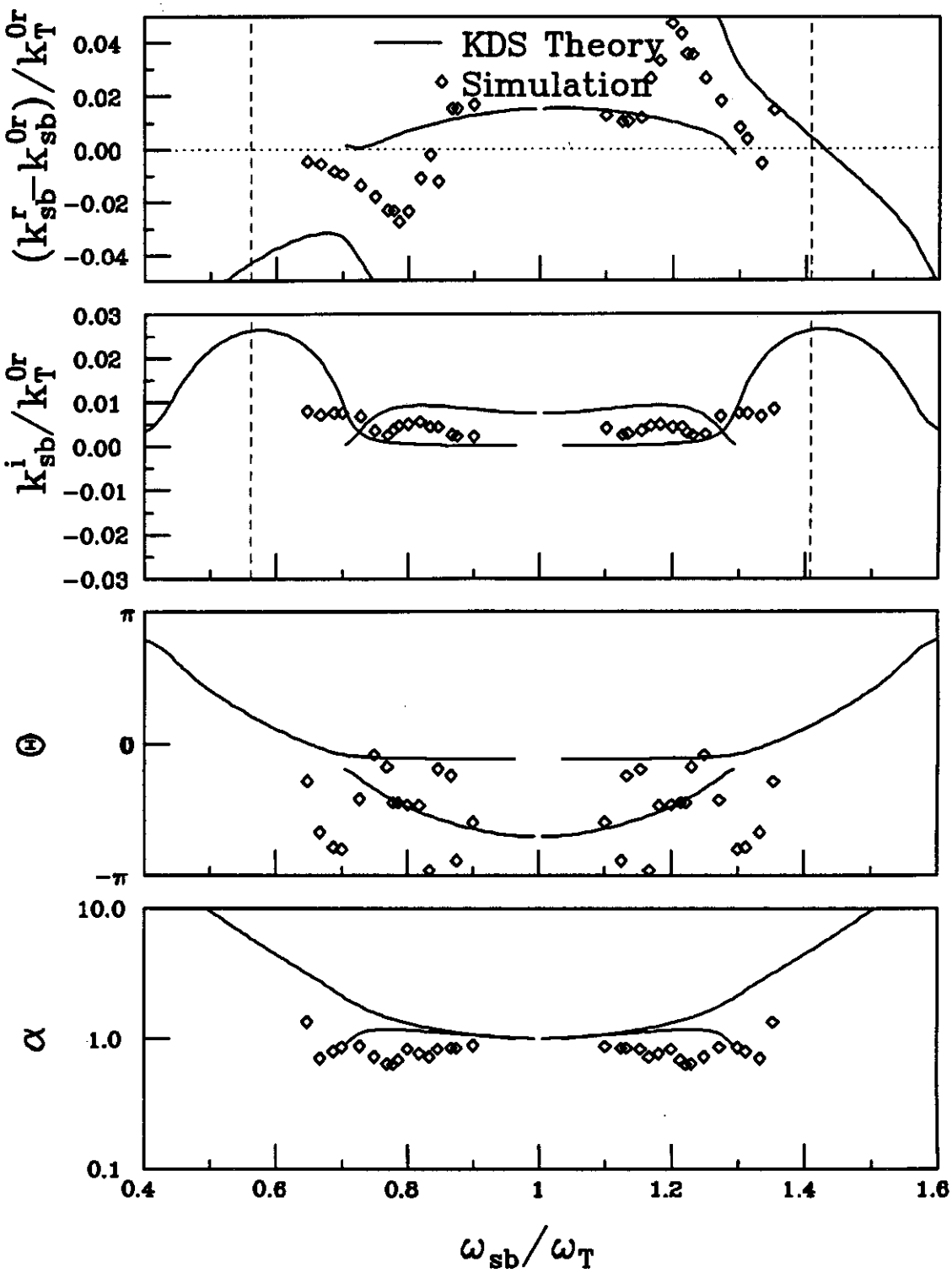

Figure 4.18: Growing sideband mode parameters in comparison with KDS theory for a trapped continuous beam: $\sigma = .4$, ω_b/ω_T=0.041, ω_p/ω_T=0.13, k_T^{∞}/k_T^{0r}=1.005.

4.4 Trapped State with Trapping Oscillations

In this section the initial and the intermediate evolution of the sidebands are studied for the case where the trapping wave undergoes bounce oscillations. This case is similar to the one studied by Dimonte and Malmberg [16]. Dimonte and Malmberg emphasized the detrapping mechanism caused by the growing sidebands. Here, the focus is on the evolution of the sidebands and in particular on their phase relationship before they grow to large amplitudes and detrap the electrons. We find that the essential features of the evolution are qualitatively well described by the macro-particle model.

4.4.1 Creating a Trapped Electron State

If a wave is launched at values lower than its saturation value, it continues to grow until its electric field is large enough to trap a fraction of the electrons. The trapped electrons then rotate in phase-space and continuously trade energy back and forth with the trapping wave. This leads to the well-known bounce oscillations of the trapping wave amplitude. By applying an external dc electric field, it is possible to replenish some of the wave energy that is lost to dissipation in the helix structure.

Experimentally a trapped electron state with oscillating trapping wave amplitude is created by launching the wave at a value below saturation, and applying an external dc electric field such that the subsequent evolution spatially averaged over the bounce oscillations is constant. An example of such an evolution is shown in figure 4.19. The dashed line marks the spatial average, where the bounce oscillations have been removed in a manner described by Tsunoda and Malmberg[62].

4.4.2 Evolution of the Sidebands

In this section we show the spatial evolution of the sidebands when the trapping wave amplitude has residual trapping oscillations. The later evolution of the sidebands, especially the modulational phase, is independent of the initial values of their amplitudes and modulational phase. Because of the bounce motion of the trapped electrons the modulational phase is not constant, but is modulated at the wavenumber of the bounce oscillations.

The sidebands are launched 40 dB below the trapping wave amplitude at the beginning of the wave-beam interaction region. Only for the highest growth rates do the sideband grow large enough to affect the trapping wave. Generally the sidebands can be considered linear. In figure 4.19a the evolution of the sideband amplitudes is shown for a case where the initial values of the the modulational phase and amplitude correspond to frequency modulation, $\Theta(z = 0\text{m}) = \pi$, $\alpha(z = 0\text{m}) = 1$. The sidebands grow approximately exponentially with a superposed oscillation that corresponds to the trapping wave oscillations. Figure 4.19b shows the spatial evolution of the phases, that also show some modulation with the trapping wave. In figure 4.19c the evolution of the modulational phase for the case shown in figure 4.19a and b (thick line) and three other initial values (thin lines) of the modulational phase is shown. The initial amplitudes of the sidebands and the trapping wave are kept the same for all four cases. Again it is observed that the modulational phase approaches the same downstream evolution independent of its initial values. The downstream evolution has a superposed modulation that is out of phase with the trapping wave amplitude oscillations.

The thin lines in figure 4.19 show the results of computer simulations of the full beam dynamics. They agree well with the measured evolution of amplitudes and phases.

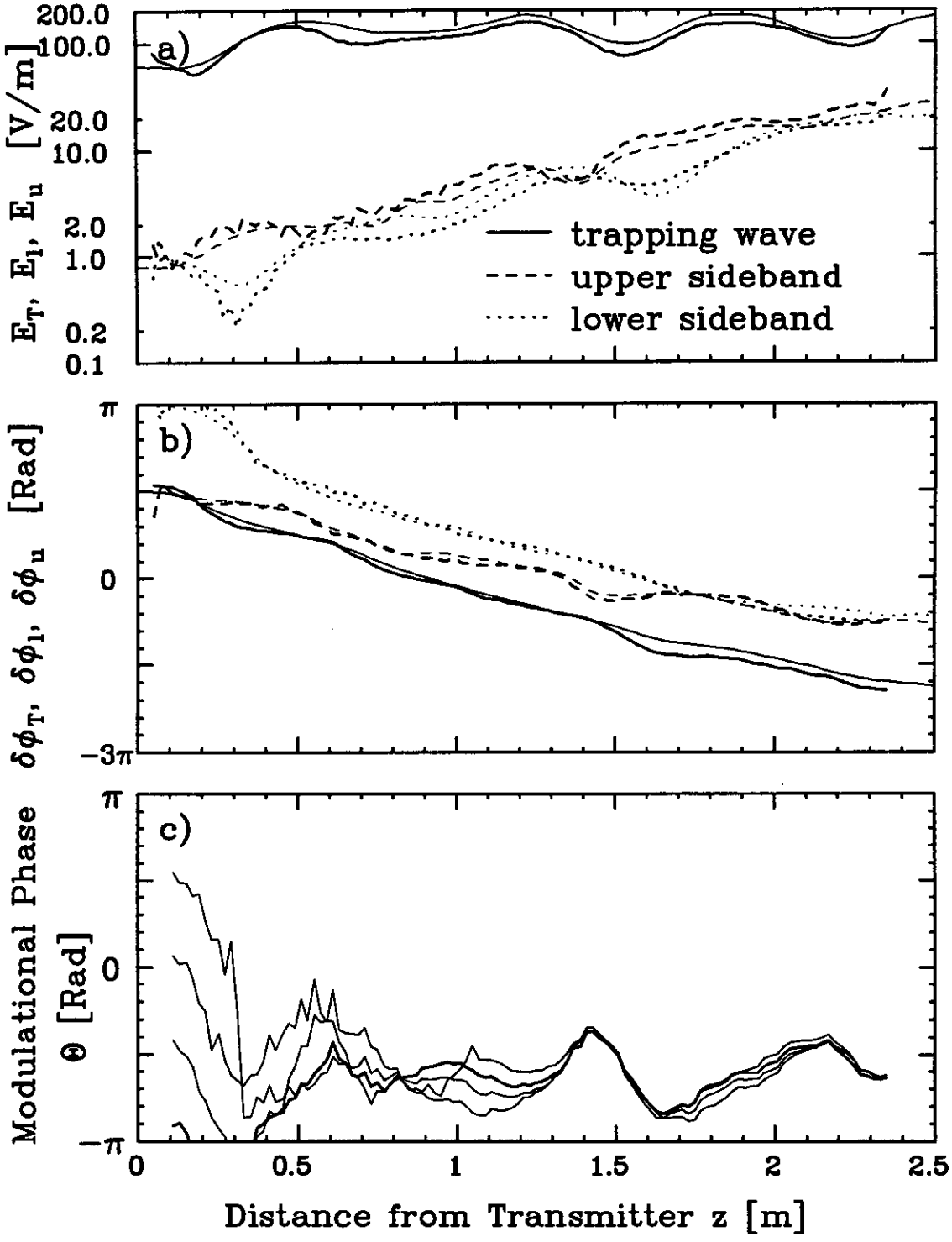

Figure 4.19: Evolution of the sideband amplitudes (a), nonlinear phases (b) and modulation phase (c) for trapping wave oscillations. The parameters are the same as in figure 4.1. Experiment: thick lines; computation: thin lines. In c) the evolution of the modulational phase is shown for $\Theta(z=0) = 0, \pi/2, \pi, 3\pi/2$. $f_T = 55.0$ MHz

4.4.3 Comparison with the Models

In this section we compare the measured, spatially averaged growth rates, wavenumber shifts, amplitude ratios and modulational phases of the sidebands in the experiments and in the computer simulations with the predictions of the sideband dispersion relation. The spatial averaging is done in a manner described by Tsunoda and Malmberg [62]. Accordingly, a spatial Fourier transformation is used to eliminate the trapping oscillations of the trapping wave and the growing sidebands by truncating the spatial Fourier modes that correspond to the trapping oscillations. This method is applied to the experimental and the computational evolutions. From the averaged values of the trapping wave amplitude and the applied dc electric field the trapped particle ratio σ is determined and used to calculate the sideband dispersion relation. Figure 4.20 shows the comparisons. In this case the agreement is better than in the case without trapping oscillations.

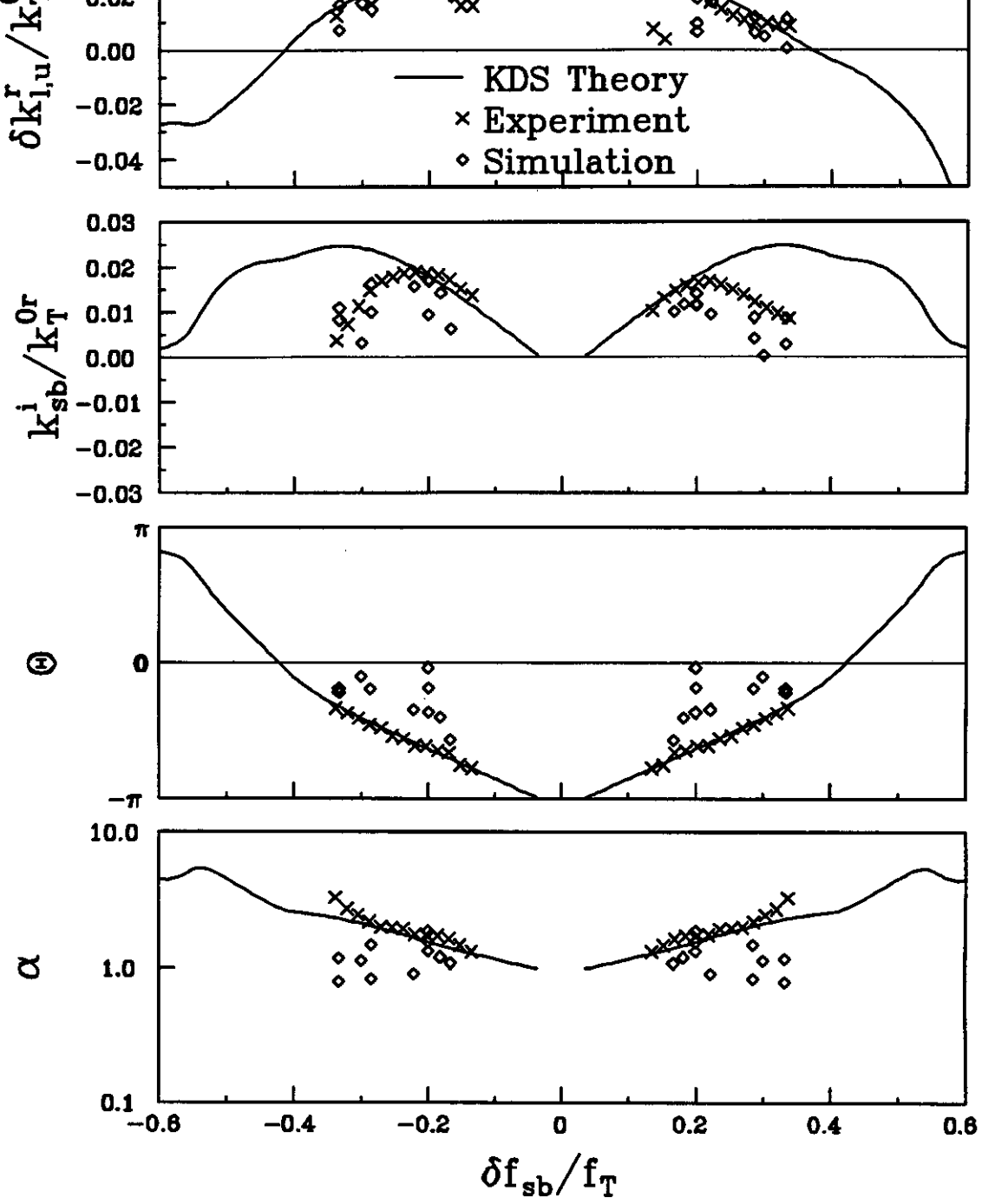

Figure 4.20: Comparison of the experiments, computer simulations and th KDS model for trapping oscillations. The parameters are the same as in figure 4.19. $\sigma = 0.67, \omega_B^{dc}/\omega_T = 0.12, \omega_p/w_T = 0.45, k_T^{\infty}/k_T^{0r} = 1.026$.

Appendix A

Local Helix Dispersion Relation

In this appendix the measurements of the local wavenumber and damping rate of the beamless helix are reported. The local values of the wavenumber and damping rates have to be included in the computer simulation of the sideband instability in order to obtain good agreement with the experiment.

Both wavenumber and damping rate can be measured with the setup described in section 2.2. A monochromatic waveform is launched on the beamless helix and its complex amplitude is measured as a function of distance along the helix. By fitting straight lines to the measured phase and the natural logarithm of the amplitude one can obtain approximate values of the real and imaginary wavenumbers. If one fits over short sections of the helix only, one can obtain local values of the real and imaginary wavenumbers.

Figure A.1 shows the spatial dependence of both the normalized difference between the measured real wavenumber and the calculated real wavenumber and of the normalized imaginary wavenumber of a typical wave. The sliding square window, that defines the region of the straight line fit, is about four wavelengths long, corresponding to 0.2 m. There are two distinct regions of approximately constant wavenumbers; both of them extending over about half the length of the helix. In the first half the average real wavenumber agrees within 0.5% with the calculated

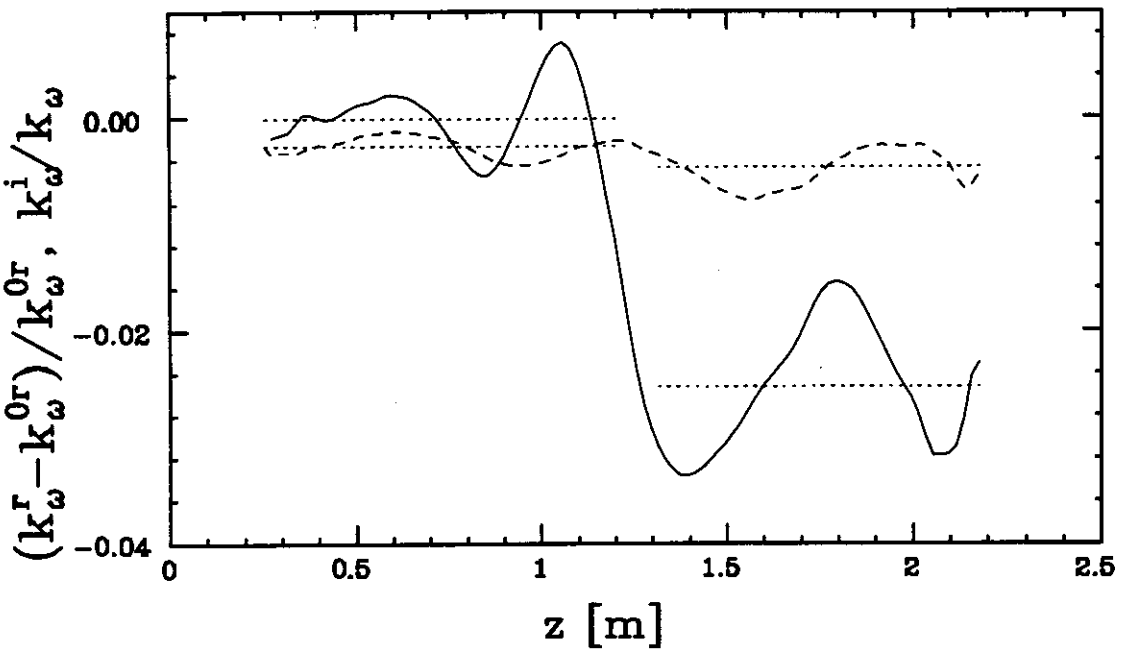

Figure A.1: Spatial dependence of the real (solid) and imaginary (dashed) wavenumber at 55.5 MHz

wavenumber. In the second half, the average real wavenumber is about 1.5% smaller than the calculated value and the imaginary wavenumber increases by about 100%. The spatial averages of the wavenumber and the damping rate for the first and the second half of the helix are shown with dotted lines in figure A.1. It is important to include the local dispersion relation in the computer simulations of the sideband instability in order to obtain good agreement with the measurements.

In figure A.2 the normalized differences between the measured and the calculated real wavenumbers are shown versus frequency for both halves of the helix. In addition the relative damping rates are shown for both halves of the helix. In the first half of the helix the measured and the calculated wavenumbers agree within 0.5% for all considered frequencies.

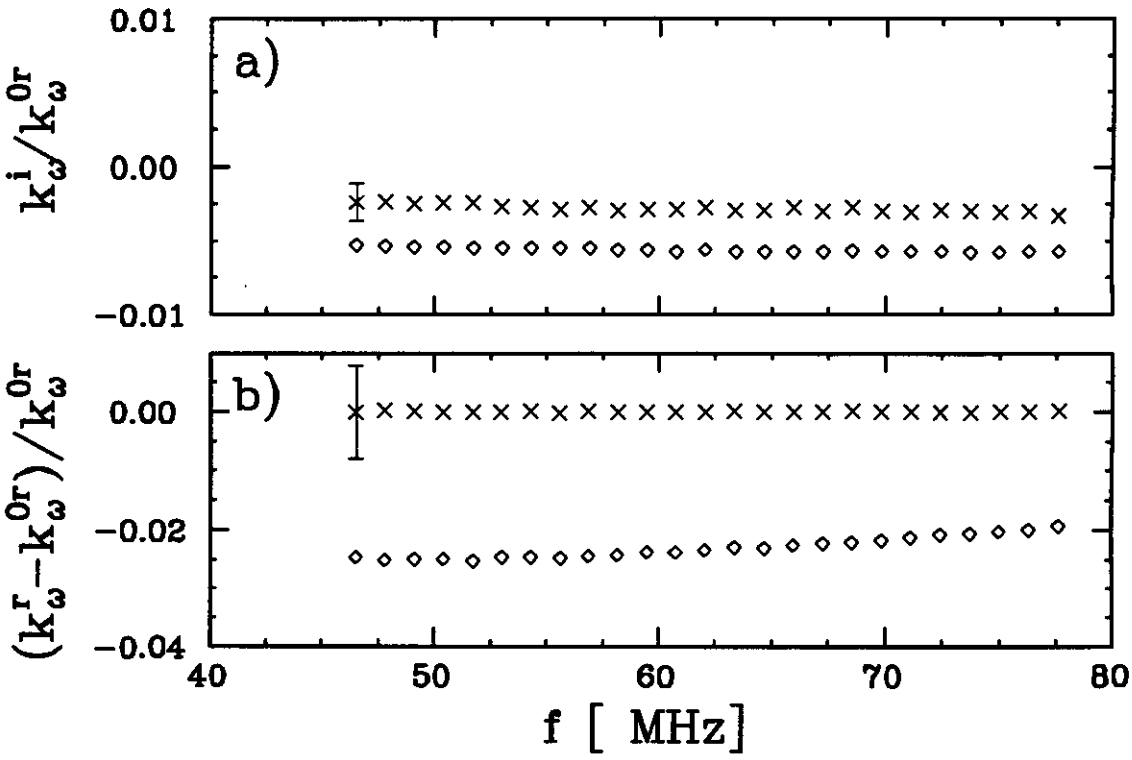

Figure A.2: a) Normalized damping rate versus frequency in first (crosses) and second (diamonds) half of helix; b) Normalized real wavenumber versus frequency in first and second half of helix.

Appendix B

Warm Beam Theories for TWT

B.1 Quasilinear Theory

In this section we derive the equations describing the interaction of a weak warm electron beam with waves on the slow wave structure of a traveling wave tube in the spirit of quasilinear theory. In the limit of a very weak beam and of small growth rates, the TWT equations become identical to the spatial equations of the one-dimensional beam-plasma case [17]. If the beam is of small but finite strength, a correction term that describes the space-charge forces that the electrons exert on each other needs to be included. As we have seen in the case of linear dispersion, the space-charge has to be included for our beam distributions.

The evolution of the electron beam is given by the one-dimensional Vlasov equation, where the electric field is the sum of the helix wave field $E^h(z,t) = -\partial V^h/\partial z$ and the space-charge field $E^{sc}(z,t)$:

$$\frac{\partial f}{\partial t} + v\frac{\partial f}{\partial z} - \frac{e}{m}(E^h(z,t) + E^{sc}(z,t))\frac{\partial f}{\partial v} = 0 \tag{B.1}$$

The space-charge electric field is given by (2.13).

The waves on the slow wave structure are described by the inhomogeneous wave equation 2.7 [7]:

$$\frac{d^2V_\omega^h}{dz^2} + k_\omega^{0\,2}V_\omega^h = -en_0\omega k_\omega^0 R_\omega \int_0^\infty f_\omega(v,z)dv \tag{B.2}$$

In the experiment a waveform with the period T is launched at $z = 0$[1].Since this signal is much larger than the inherent noise of the TWT, all time-dependent quantities $f(v,z,t)$, $E(z,t)$, $E^{sc}(z,t)$ have the same period T and can be expanded in a Fourier series:

$$f(z,v,t) = f_0(v,z) + \frac{1}{2}\sum_n f_n(v,z)e^{-i\omega_n t} \tag{B.3}$$

$$E^h(z,t) = \frac{1}{2}\sum_n E_n^h(z)e^{-i\omega_n t} \tag{B.4}$$

$$E^{sc}(z,t) = \frac{1}{2}\sum_n E_n^{sc}(z)e^{-i\omega_n t} \tag{B.5}$$

$$\text{with } E_n(z)^h = \frac{2}{T}\int_0^T dt E^h(z,t)e^{i\omega_n t} \text{ etc.} \tag{B.6}$$

The sums are over all the positive and negative Fourier mode numbers n of the launched waveform (dc excluded). Because of the homodyning process their corresponding frequencies $\omega_n/2\pi$ are between about 30 and 83 MHz and are given by

$$\omega_{|n|} = f_{\text{hom}} - \frac{|n|}{N} f_{\text{clock}}, \tag{B.7}$$

$$\omega_{-|n|} = -\omega_{|n|}, \tag{B.8}$$

where $f_{\text{hom}} = 86$ MHz is the homodyning frequency, $f_{\text{clock}} = 120$ MHz is the clock frequency of the arbitrary waveform generator and the sampling frequency of the digital oscilloscope, n the mode number and N the number of wavepoints constituting the waveform. In the following we will often use the subscript n as an abbreviation of ω_n. In our nomenclature: $E_{-n} = E_n^*$.

With this expansion the inhomogeneous wave equation and the Vlasov equation become

$$\frac{d^2V_n^h}{dz^2} + (k_n^0)^2 V_n^h = -en_0\omega_n k_n^0 R_n \int_0^\infty f_n dv \tag{B.9}$$

[1]Actually the launched waveform is not strictly periodic with period T, because the frequency of the local oscillator used for the homodyning process is not phase-locked to the clock of the arbitrary waveform generator. Using the clock itself as the local oscillator, we checked that this modulation does not affect the beam dynamics.

$$-i\omega_n f_n + v\frac{\partial f_n}{\partial z} - \frac{e}{m}(E_n^h + E_n^{sc})\frac{\partial f_0}{\partial v} = \frac{1}{2}\frac{e}{m}\sum_{n'}(E_{n-n'} + E_{n-n'}^{sc})\frac{\partial f_{n'}}{\partial v} \quad \text{(B.10)}$$

$$v\frac{\partial f_0}{\partial z} = \frac{1}{2}\frac{e}{m}\sum_{n}(E_{-n}^h + E_{-n}^{sc})\frac{\partial f_n}{\partial v} \quad \text{(B.11)}$$

Quasilinear theory completely neglects the mode-coupling terms on the r.h.s. of equation (B.10). Much of the controversy surrounding quasilinear theory is about whether keeping these terms changes the predictions of quasilinear theory in zeroth order. With this approximation the solution of equation (B.10) becomes:

$$f_n(v,z) = f_n(v,0)e^{i\frac{\omega_n}{v}z} + e^{i\frac{\omega_n}{v}(z-z')}\int_0^z \frac{dz'}{v}e^{i\frac{\omega}{v}(z-z')}(E_n^h(z') + E_n^{sc}(z'))\frac{\partial f_0(v,z')}{\partial v} \quad \text{(B.12)}$$

The first term describes the free streaming of the initial perturbation. We will neglect it in the following because - except near the edge of the velocity distribution - its contribution phase-mixes to zero over a few wavelengths. Writing $E_n^h(z')$ as

$$E_n^h(z') = E_n^h(z)e^{i\int_z^{z'} dz'' k_n(z'')} \quad \text{(B.13)}$$

we obtain from (2.12), (2.7) and (B.12):

$$E_n^{sc}(z) = P_q(k_n^r(z)r_b)\epsilon^h(\omega_n, k_n(z))E_n^h(z) = H_q(\omega_n)E_n^h(z). \quad \text{(B.14)}$$

Using (B.12) we obtain from (B.9):

$$\begin{aligned}&((k_n^0)^2 - k_n^2(z))E_n^h(z)\\ &= \frac{ie^2 n_0 R_n \omega_n k_n^0 k_n}{m}[1 + H_q(\omega_n)]E_n^h(z)\int_0^\infty dv\int_0^z \frac{dz'}{v}e^{i\int_{z'}^z dz''(\frac{\omega_n}{v} - k_n(z''))}\frac{\partial f_0(v,z')}{\partial v}\end{aligned} \quad \text{(B.15)}$$

If the time-averaged velocity distribution function $f_0(v,z')$ is a Gaussian centered around $v = v_b$ with a width of Δv_b then the major contributions to the v-integration come from regions where $|z - z'| \leq v_b^2/\omega\Delta v_b$. Assuming that the velocity width Δv_b is approximately equal to the width in phase velocity of the unstable waves, this

distance becomes equal to the autocorrelation length l_{ac} (see equation (3.8)). In the quasilinear regime the autocorrelation length is much smaller than the length scale of evolution of the electric field spectrum and the time-averaged velocity distribution function and one can therefore set $k_n(z') \approx k_n(z)$ and $f_0(v,z') \approx f_0(v,z)$.

With this approximation we obtain the quasilinear dispersion relation:

$$\epsilon^h(\omega_n, k_n(z)) = \omega_p^2[1 + H_q(\omega_n)]\frac{-1}{k_n^2(z)}\int_{0\mathcal{L}}^{\infty} dv \frac{\partial f_0(v,z)/\partial v}{v - \omega_n/k_n(z)} \qquad \text{(B.16)}$$

where the v-integration is taken along the Landau contour $\mathcal{L}$.

This expression together with equation (B.13) states that the growth rate of the waves at position z is determined by the solution $k_n(z)$ of the dispersion relation based on the **local** velocity distribution $f_0(v,z)$. In appendix D we discuss the validity of this expression for the beam distribution in the TWT, where initially above phase-mixing approximations are not valid because of the abrupt fall-off of the velocity distribution at high velocity. There we give an estimate of the contributions of $f_0(v,z')$ and $k_n(z')$ with $z' < z$ to the solutions of the dispersion relation at z.

Because the growth rate depends only on the time-averaged velocity distribution, which is (and stays as seen below) a smooth function of velocity, it also is a smooth function of frequency. Therefore quasilinear theory predicts that a launched smooth wave spectrum will stay smooth throughout the evolution of the instability.

The evolution equation for the velocity distribution function is obtained by using (B.12) in (B.11):

$$v\frac{\partial f_0(v,z)}{\partial z} = \frac{1}{2}\frac{\partial}{\partial v}\frac{e^2}{m^2}\sum_n \mid E_n^h(z) + E_n^{sc}(z) \mid^2 \int_0^z \frac{dz'}{v} e^{i\int_{z'}^{z}(\frac{\omega_n}{v} - k_n(z''))dz''} \frac{\partial f_0(v,z')}{\partial v} \qquad \text{(B.17)}$$

If the electric field spectrum E_n^h has the shape of a Gaussian centered around ω (where the phase velocity is v_{ph} and the group velocity is v_{gr}) with width $\Delta\omega$ then the major contributions to the sum over the frequencies come from regions where

$|z-z'| \leq v_{ph}^2/\omega\Delta v_{ph}$ which is equal to the autocorrelation length of the introduction; it is the approximate distance over which an electron of velocity $v = v_{ph}$ looses the correlation with the waves of the spectrum because of phase-mixing. In the quasilinear regime given by (3.1) we can replace $k_\omega(z')$, $f_0(z')$ and $E_\omega^{sc}(z')$ with the values at $z = z'$ and obtain the familiar Fokker-Planckh equation for the evolution of the time-averaged electron velocity distribution.

$$v\frac{\partial f_0(v,z)}{\partial z} = \frac{\partial}{\partial v}D^{ql}(v,z)\frac{\partial f_0(v,z)}{\partial v} \tag{B.18}$$

with

$$D^{ql}(v,z) \equiv \frac{e^2}{m^2}\sum_{n>0} \mid 1+H_q \mid^2 \mid E_n^h(z) \mid^2 \frac{vk_n^i}{(\omega_n - vk_n^r)^2 + (vk_n^i)^2} \tag{B.19}$$

where D^{ql} is the quasilinear diffusion coefficient.

If we had anticipated the phase-mixing, we could have simplified (B.12) with

$$f_n(v,z) = \frac{e}{m}(E_n^h(z) + E_n^{sc}(z))R^{ql}(\omega_n, k_n)\frac{\partial f_0 v, z}{\partial v} \tag{B.20}$$

with the quasilinear resonance function

$$R^{ql}(\omega_n, k_n) \equiv \frac{i}{\omega_n - k_n(z)v} \tag{B.21}$$

and obtained the quasilinear equations much faster.

B.2 Resonance Broadening Theory

In this section we derive Dupree's equations for the traveling wave tube. Dupree attempted to improve on quasilinear theory by including some of the mode-coupling terms from the r.h.s. of equation (B.10) when calculating the propagator of the perturbations of the velocity distribution function. This leads to a broadening of the wave-particle resonance, hence his theory is called "resonance-broadening (RB) theory". As has been pointed out by Rolland [51], trapping effects are associated

with mode-coupling terms that are not included in this approach. They become important when the turbulent trapping length becomes approximately equal to the growth length. So on grounds of simple arguments one would expect RB theory to break down when $l_{tt} \approx k_i^{-1}$, which is the threshold for the predictions of RB theory to deviate from QL theory.

To formulate the RB theory for the TWT we start again with equations (B.9) to (B.11). Without neglecting the mode-coupling term, (B.10) has the exact solution:

$$f_n(v,z) = \frac{1}{2}\frac{e}{m}\int_0^z \frac{dz'}{v} e^{i\frac{\omega_n}{v}(z-z')} \sum_{n'} (E^h_{n-n'}(z') + E^{sc}_{n-n'}(z')) \frac{\partial f_{n'}(v,z)}{\partial v} \qquad \text{(B.22)}$$

Iterating (B.10) with this solution, picking out terms with f_n and discarding the other mode-coupling terms yields:

$$\begin{aligned} &-i\omega_n f_n + v\frac{\partial f_n}{\partial z} \\ &\quad -\frac{1}{2}\frac{e^2}{m^2}\sum_{\omega_{n'}} (E^h_{n-n'} + E^{sc}_{n-n'}) \frac{\partial}{\partial v}\int_0^z \frac{dz'}{v} e^{i\frac{\omega'_n}{v}(z-z')} (E^h_{n'-n}(z') + E^{sc}_{n'-n}(z')) \frac{\partial f_n(v,z')}{\partial v} \\ &\quad = \frac{e}{m}(E^h_n + E^{sc}_n)\frac{\partial f_0}{\partial v} \end{aligned} \qquad \text{(B.23)}$$

which can be written as

$$-i\omega_n f_n + v\frac{\partial f_n}{\partial z} - \frac{\partial}{\partial v}\hat{D}(v,z)\frac{\partial f_n}{\partial v} = \frac{e}{m}(E^h_n + E^{sc}_n)\frac{\partial f_0}{\partial v} \qquad \text{(B.24)}$$

with the diffusion operator $\hat{D}(v,z)$ acting on $\partial f_n/\partial v$. In order to proceed we assume that $\hat{D}$ is simply a function $D^{rb}(v,z)$. Then the approximate Green's function of the l.h.s. of (B.24) is:

$$G(v, z-z') = e^{i\frac{n}{v}(z-z') + i\frac{\omega_n D^{rb}}{v_b^4}(z-z')^2 - \frac{D^{rb}\omega_n{}^2}{3v_b^5}(z-z')^3} + O(\frac{v}{v_b} - 1) \qquad \text{(B.25)}$$

where v_b is a typical beam velocity, e.g. the average velocity. For large $z - z'$ the second term in the exponential can be neglected compared with the third. Then the

solution of (B.24) is approximately given by:

$$f_n = \frac{e}{m}\int_0^z \frac{dz'}{v} e^{i\frac{\omega_n}{v}(z-z') - \frac{D^{rb}\omega_n{}^2}{3v_b^5}(z-z')^3} (E_n(z') + E_n^{sc}(z'))\frac{\partial f_0(v,z')}{\partial v} \tag{B.26}$$

This expression is used in (B.9) and (B.11) to obtain the dispersion relation of the waves and the diffusion equation of the time-averaged velocity distribution function. Similar to QL theory the major contributions will come from the values close to z. Anticipating this, one can simplify (B.26) to obtain:

$$f_n = \frac{e}{m}E_n^h(z)[1 = H - q(\omega_n)]\frac{\partial f_0(v,z)}{\partial v}\int_0^z \frac{dz'}{v} e^{i(\frac{\omega_n}{v} - k_n(z))(z-z') - \frac{(z-z')^3}{l_{tt}^3}} \tag{B.27}$$

where - spatially equivalent to Dupree - the "turbulent trapping length", l_{tt}, is defined by:

$$l_{tt} \equiv \Big(\frac{3v_b^5}{\omega_n{}^2 D^{rb}(v_b)}\Big)^{\frac{1}{3}} \tag{B.28}$$

The integral expression is a resonance function. If the electric field amplitudes are small and the turbulent trapping length l_{tt} is much larger than the scale length of the evolution of spectrum and of velocity distribution function, the last term in the exponential can be omitted and one again obtains the Lorentzian resonance function of quasilinear theory (B.21). In general, however, the resonance width is given by

$$\Delta(\frac{\omega_n}{v} - k_n^r) \approx Max\Big(\frac{\sqrt[3]{3}}{l_{tt}}, k_n^i\Big) \tag{B.29}$$

Thus in the nonlinear regime near saturation where large electric fields occur the resonance function becomes wider even though the growth rates become smaller. However, as Rolland pointed out [51], this is the regime where the neglected terms in the selected sum become important.

We define a complex resonance function similar to Dupree's[2].

$$R^{rb}(\omega_n, k_n, v, D^{rb}) \equiv \int_0^z \frac{dz'}{v} e^{i(\frac{\omega_n}{v} - k_n(z))(z-z') - \frac{(z-z')^3}{l_{tt}^3}} \tag{B.30}$$

[2]Dupree's version assumed very small growth rates and was therefore real.

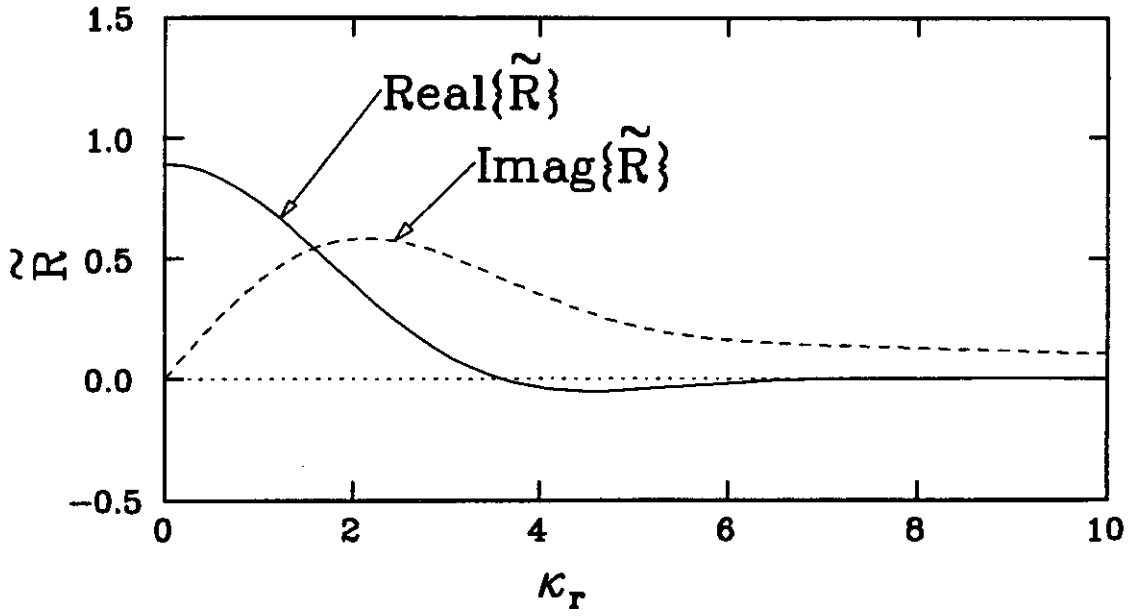

Figure B.1: Plot of the scaled resonance function $\tilde{R} \equiv \int_0^\infty d\zeta e^{i(\kappa^r + i\kappa^i)\zeta - \zeta^3}$ for $\kappa^i = 0$.

and its normalized form for large z

$$\tilde{R}(\kappa^r + i\kappa^i) \equiv \int_0^\infty d\zeta e^{i(\kappa^r + i\kappa^i)\zeta - \zeta^3} \tag{B.31}$$

It is shown in figure B.1 as a function of κ^r for $\kappa^i = 0$. The total area under the curve of the real part is π.

Then the equations that describe the evolution of the wave spectrum and the time-averaged velocity distribution function for the TWT become:

$$\epsilon^h(\omega_n, k_n(z)) = -ik_n \frac{\omega_p^2}{k^2}[1 + H_q(\omega_n)] \int_0^\infty R^{rb}(\omega_n, k_n, v, D^{rb}) \frac{\partial f}{\partial v} \tag{B.32}$$

$$v\frac{\partial f_0}{\partial z} = \frac{\partial}{\partial v} D^{rb}(v, z) \frac{\partial f_0}{\partial v} \tag{B.33}$$

where

$$D^{rb}(v, z) = \frac{e^2}{m^2} \sum_{n>0} \mid 1 + H_q \mid^2 \mid E_n^h \mid^2 R^{rb}(\omega_n, k_n, v, D^{rb}) \tag{B.34}$$

Note that equations (B.33) and (B.33) become the quasilinear equations if the Dupree resonance function R^{rb} is replaced with the quasilinear resonance function R^{ql}.

Appendix C

Four-Wave Coupling Model

In this section we derive the field amplitude expansion to second order of quasilinear theory and resonance-broadening theory that leads to an expression for four-wave coupling following Sagdeev *et al.* [53].

We assume that the velocity distribution function and the electric field can be written as a converging sum of different orders where higher order terms can be neglected with some accuracy. As has been shown in the past, such an expansion does not converge in the nonlinear regime of the weak-warm beam instability when $k^i \leq l_{tt}^{-1}$. However, we only want to obtain a framework in which to discuss the observed mode-coupling and therefore do not claim that this expansion is accurate. Formally we write:

$$f = f_0 + f^{(1)} + f^{(2)} + \ldots \tag{C.1}$$

$$E = E^{(1)} + E^{(2)} + \ldots \tag{C.2}$$

where f_0 is the time-averaged beam velocity distribution, $f^{(1)}$ is the first order perturbation calculated in quasilinear theory and $E^{(1)}$ is the electric field to first order as calculated in quasilinear theory.

Expanding the Vlasov equation to different orders leads to (space-charge

neglected):

$$\frac{\partial f^{(1}}{\partial t} + v\frac{\partial f^{(1)}}{\partial z} - \frac{e}{m}E^{(1)}\frac{\partial f_0}{\partial v} = 0 \tag{C.3}$$

$$\frac{\partial f^{(2}}{\partial t} + v\frac{\partial f^{(2)}}{\partial z} - \frac{e}{m}E^{(1)}\frac{\partial f^{(1)}}{\partial v} = \frac{e}{m}E^{(2)}\frac{\partial f_0}{\partial v} \tag{C.4}$$

$$\frac{\partial f^{(3)}}{\partial t} + v\frac{\partial f^{(3)}}{\partial z} - \frac{e}{m}E^{(1)}\frac{\partial f^{(2)}}{\partial v} - \frac{e}{m}E^{(3)}\frac{\partial f_0}{\partial v} = \frac{e}{m}E^{(2)}\frac{\partial f^{(1)}}{\partial v} \tag{C.5}$$

Because of the dispersion relation of the helix that does not support 3-wave coupling and because of the fact that the beam distribution is small at low velocities, the terms on the r.h.s. of above equations can be neglected. Proceeding in the usual manner we obtain after some algebra:

$$\begin{aligned}
&(k_n^{0\,2} - k_n^{(3)\,2})E_n^{(3)} \\
&= ik_n^{(3)}\frac{e^4 n_0 R_n \omega_n k_n^0}{8m^3}\int_0^\infty dv \sum_{n_1}\sum_{n_2}\sum_{n_3} R(\omega_n, k_{n_3} + k_{-n_1} + k_{n_2}) \\
&\times \frac{\partial}{\partial v}R(\omega_{n_1} - \omega_{n_2}, k_{-n_1} + k_{n_2})\frac{\partial}{\partial v}R(\omega_{n_2}, k_{n_2})\frac{\partial f_0(v,z)}{\partial v} \\
&\times E_{n_3}^{(1)}(z)E_{-n_1}^{(1)}(z)E_{n_2}^{(1)}(z)\delta_{n_3, n-n_2+n_1}
\end{aligned} \tag{C.6}$$

where for the wave-particle resonance function we can either use the quasilinear resonance function R^{ql} or Dupree's resonance function R^{rb}. We write this expression as

$$\begin{aligned}
\frac{dE_n(z)}{dz} &\approx ik_n(z)E_n^{(1)}(z) \\
&+ \sum_{n_1}\sum_{n_2}\sum_{n_3}\Gamma_{n,n_1,n_2,n_3}E_{n_3}^{(1)}(z)E_{-n_1}^{(1)}(z)E_{n_2}^{(1)}(z)\delta_{n_3,n+n_1-n_2}
\end{aligned} \tag{C.7}$$

where

$$\Gamma_{n,n_1,n_2,n_3} \equiv \frac{e^4 n_0 R_n \omega_n k_n^0}{16m^3}(\frac{1}{k_{n_3}} + \frac{1}{k_{-n_1}} + \frac{1}{k_{n_2}})\frac{\partial}{\partial v}R(\omega_{n_1} - \omega_{n_2}, k_{-n_1} + k_{n_2})\frac{\partial}{\partial v}R(\omega_{n_2}, k_{n_2})\frac{\partial f_0(v,z)}{\partial v}$$

Appendix D

Nonlocal Dispersion Relation

The beam velocity distribution used in the experiments on the weak warm beam instability has a large velocity gradient at its upper velocity edge. Therefore waves with phase velocities close to the edge of the beam do not fulfill the phase mixing requirement that led to the simplification of equation (B.15) to obtain the quasilinear dispersion relation. The growth of these waves then is given by the nonlocal expression (B.15) rather than by the local dispersion relation (B.16). In the nonlinear regime, the velocity distribution function starts flattening out. It then is possible that the growth rates of these waves at a certain position are not only due to the local velocity distribution but are also partially determined by the distribution at earlier positions.

In this section we experimentally investigate this effect that is solely an artifact of the shape of the beam used in the traveling wave tube. We find that in regions where the velocity distribution function changes, the growth rate of waves with phase velocities close to the edge of the beam distribution are larger than predicted from the quasilinear and resonance-broadening dispersion relation. This discrepancy can account for some of the discrepancy still observed between the measured ensemble-averaged growth rates and the predictions of theory.

This appendix is organized as follows: In section D.1 we calculate the spatial

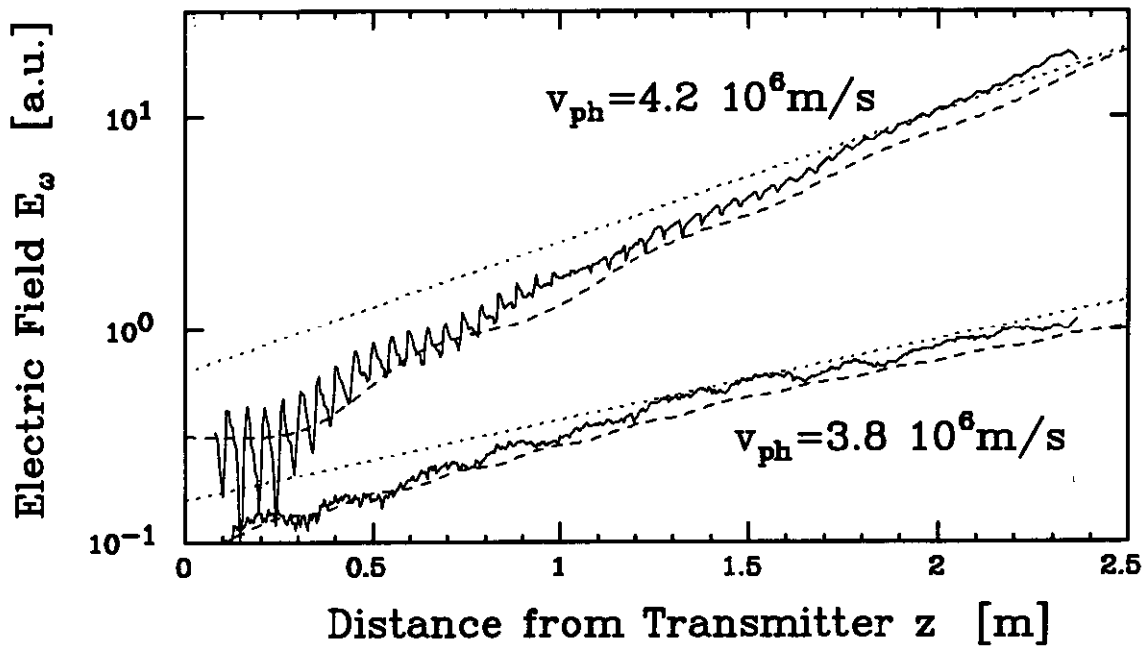

Figure D.1: Spatial evolution of single wave electric field amplitudes on the warm beam 3.3 (solid lines) and comparison with the solution of (D.1) (dashed line) and with the solution of the linear dispersion relation (2.21) (dotted lines) for two different phase velocities.

evolution of waves in the linear regime where the velocity distribution does not change with distance and find good agreement with experiment. The edge of the beam causes beat oscillations that we find in both our calculations and our experiments. In section D.2 we calculate the spatial evolution of waves in the nonlinear regime where the velocity distribution function changes and find that nonlocal contributions are not negligible in (B.15) for waves with phase velocities close to the edge of the beam.

D.1 Linear Nonlocal Dispersion Relation

In this section we numerically solve equation (B.15) for the linear case where the velocity distribution function does not change spatially. We find good agreement with experiment.

Figure D.1 shows the calculated and the measured growth of two single waves launched on the warm beam shown in figure 3.3. They are launched at low amplitudes such that the beam distribution is unchanged. The local wavenumber of the waves $k_n^c(z)$ is calculated from (B.15) by integrating along the distance from the transmitter z

$$((k_n^0)^2 - k_n^{c\,2}(z)) = \frac{ie^2 n_0 R_n \omega_n k_n^0 k_n^c(z)}{m} \frac{\partial f_0(v, z=0)}{\partial v} [1 + H_q] \int_0^\infty dv \int_0^z \frac{dz'}{v} e^{i \int_{z'}^z dz'' \left(\frac{\omega_n}{v} - k_n^c(z'')\right)} \quad \text{(D.1)}$$

where we assume $k_n^c(z=0) = k_n^0$ and use the local values of the helix wavenumbers $k_n^0(z)$. We then obtain the spatial evolution of the electric field amplitude $E_n^c(z)$ from:

$$E_n^c(z) = E_n^c(z=0) e^{i \int_0^z dz' k_n^c(z')}. \quad \text{(D.2)}$$

The intial electric field amplitude $E_n(z=0)$ can be chosen arbitrarily to fit the experimental data.

Close to the transmitter experiment and calculation show wave growth with a superposed beat with a mode associated with the edge of the beam. At higher phase velocity these beat oscillations have a longer wavelength. They diminish with increasing distance from the transmitter such that close to the end of the interaction region the growth rates of the experiment, the solution of equation (D.1) and the solution of the linear dispersion relation (shown as a straight line) approximately agree with one another.

D.2 Nonlinear Nonlocal Dispersion Relation

In this section we numerically solve equation (B.15) for the case where the velocity distribution changes with distance. Since we cannot measure the velocity distribution at other positions than at the end of the interaction region we launch

different waveforms in order to infer it at positions of interest. Since the diffusion process leads to a smoothing of the troublesome edge we consider an intermediate case where the final distribution has not completed flattened yet (A=-8 dB). We find that growth rate enhancement due to nonlocal effects can account for some of the discrepancy between the measured and the quasilinear and resonance-broadened growth rates shown in figure 3.23.

In order to solve (B.15) we must know the velocity distribution as a function of distance. Even though the position of the velocity analyzer is fixed at the end of the interaction region at $z = L$, in an ideal experiment one could take advantage of the translational symmetry and simply move the transmitter by some distance Δz closer to the velocity analyzer. Then the measured velocity distribution would correspond to the distribution at position $L - \Delta z$. By moving the transmitter to different position we could then measure the velocity distribution corresponding to different locations of the evolution. Unfortunately we cannot do this in our experiment since reflected waves and the waves that travel from the transmitter toward the cathode can premodulate the beam and change the initial conditions. However, because the initial growth of the spectrum is linear and we know the linear growth rates and wavenumber shifts we leave our transmitter in place but calculate the launch spectrum required such that once it has grown over the distance Δz it equals the original spectrum at $z = 0$. This corresponds to moving a "virtual transmitter" rather than the real transmitter.

In figure D.2a we compare the ensemble-averaged electric field spectra at the end of the interaction region obtained for different launched spectra with the spectra at different positions of the evolution of interest. The agreement is reasonable for most phase velocities. In figure D.2b we show the corresponding measured velocity distributions. We now can numerically integrate equation (B.15) by interpolating

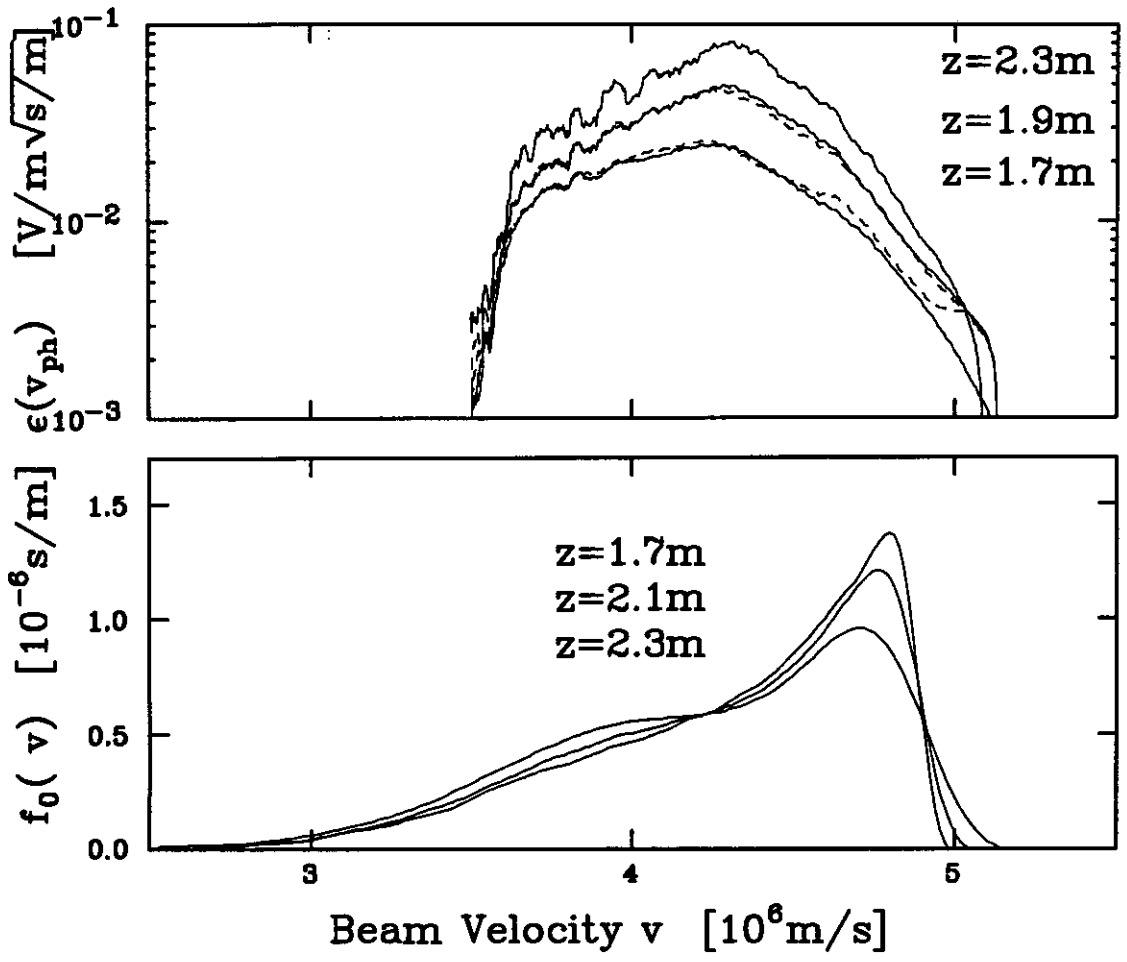

Figure D.2: a) Comparison of the wave spectra measured at different positions (solid) for the case with $A = 8$dB with wave spectra (dashed) measured at $z = L$ for different launch spectra. b) Measured velocity distributions corresponding to the dashed spectra of a).

for velocity distributions at points between measured locations and otherwise in the same manner as before.

$$((k_n^0)^2 - k_n^{c\,2}(z)) = \frac{ie^2 n_0 R_n \omega_n k_n^0 k_n^c(z)}{m}[1 + H_q] \int_0^\infty dv \int_0^z \frac{dz'}{v} e^{i\int_{z'}^z dz''\left(\frac{\omega_n}{v} - k_n^c(z'')\right)} \frac{\partial f_0(v, z')}{\partial v} \quad \text{(D.3)}$$

Resonance-broadening theory makes the same phase-mixing assumption as quasilinear theory. By determining the turbulent trapping length at different positions from the self-consistently calculated resonance-broadening diffusion coefficient

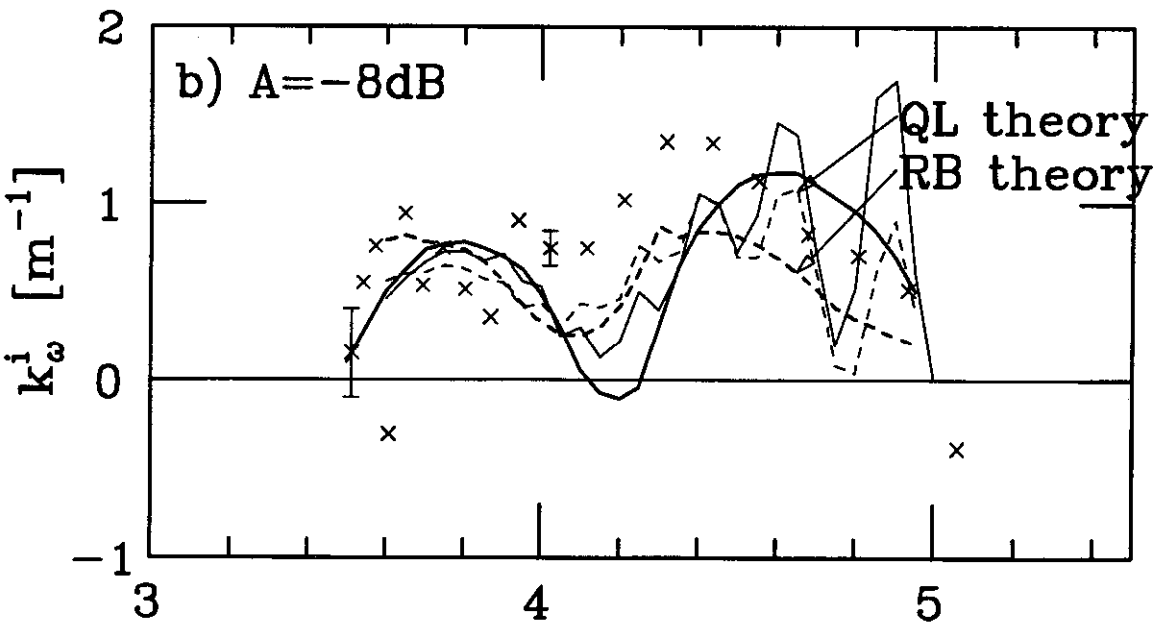

Figure D.3: Comparison of ensemble-averaged growth rates with local dispersion relation of QL and RB theory (solid, dashed thick lines, resp.) and with nonlocal dispersion relation of QL and RB theory (solid, dashed thin lines, resp.) for case shown in previously in figure 3.22.

we can also integrate the equivalent equation:

$$\begin{aligned} & k_n^{0\,2} - k_n^2(z) \\ &= i\frac{e^2 n_0 \omega_n k_n^0 R_n}{m}[1 + H_q] \\ & \quad k_n(z)\int_0^\infty dv \int_0^z dz' e^{i\int_{z'}^{z}(\frac{\omega_n}{v} - k_n(z'') - \frac{3z''^2}{i_{tt}^3(z'')})dz''} \frac{\partial f_0(v,z')}{\partial v} \end{aligned} \tag{D.4}$$

Figure D.3 compares the measured ensemble-averaged growth rates of waves of the case shown in figure 3.22 with the calculated growth rates from the nonlocal dispersion relations according to quasilinear and resonance-broadening theory. We find that starting with intermediate phase velocities the memory effect is non-negligible and close to the edge of the velocity distribution the beat of the wave with the beam edge mode causes large errors if the growth rates are determined by simply fitting a straight line to the amplitudes over a short region.

Appendix E

KDS Theory for TWT

In this section we follow the derivation of Kruer, Dawson and Sudan (KDS) [37] to obtain the sideband dispersion relation for the spatial case of the TWT.

In the macro-particle model the trapped electron distribution of each potential trough of the trapping wave is approximated by a macro-particle of effective charge and mass, whose ratio equals e/m. KDS treat the case where these macro-particles are at the bottom of the wave trough in their equilibrium position and move though the background plasma at the phase velocity of the trapping wave. For our case, we assume that this phase velocity is the asymptotic phase velocity of the dynamic equilibrium, v_T^∞. KDS approximate the sinusoidal potential well of the trapping wave with a harmonic well with bounce frequency ω_B. The trapping wave provides only the potential for the macro-particles, and is not influenced by their motion. For the nth harmonic oscillator the equation of motion of the macro-particle in a perturbing electric field $E(z,t)$ becomes:

$$\ddot{z}_n(t) = -\omega_B^2(z_n - z_n^0 - v_T^\infty t) - \frac{e}{m}E(z_n,t). \qquad \text{(E.1)}$$

z_n^0 is the location of the nth oscillator at t=0; $z_n(t)$ is its location at time t.

In order to solve for the spatial evolution we need to know the time t_n when

the nth macro-particle arrives at the location z. We find:

$$\frac{dt_n^2}{dz^2} = -\frac{1}{\dot{z}_n^3}\Big[-\omega_B^2(z - v_T^\infty t_n^0 - v_T^\infty t_n) - \frac{e}{m}E(z,t_n)\Big]. \tag{E.2}$$

t_n^0 is the time when the nth electron entered the interaction region in the TWT. Approximating $\dot{z}_n$ with v_T^∞ and transforming into the moving frame where $\delta t_n \equiv t_n - \frac{z_n}{v_T^\infty} - \frac{z_n^0}{v_T^\infty}$ and after Fourier analysis we find:

$$\delta t_n(k) = -\frac{e}{m v_T^{\infty 3}}\frac{1}{k^2 - \omega_B^2/v_T^{\infty 2}}\int \frac{d\omega'}{2\pi}E(k + \frac{\omega'}{v_T^\infty}, \omega')e^{i\omega' t_n^0} \tag{E.3}$$

The charge density of the perturbed harmonic oscillator is:

$$\rho_n(z,t) = -e\delta(z - v_T^\infty t - z_n^0 + v_T^\infty \delta t_n(z)) \tag{E.4}$$

After Fourier analysis and assuming small deviations from the straight line particle orbits we obtain:

$$\rho_n(k,\omega) = \frac{e}{v_T^\infty} i\omega e^{i\omega t^0}\delta t_n(k - \frac{\omega}{v_T^\infty}) \tag{E.5}$$

We impose self-consistency by requiring that the perturbing electric fields are generated by the perturbed charge densities of the harmonic oscillators through the transmission line equation (2.9). Combining (2.9), (E.5) and (E.4) we obtain:

$$\epsilon^h(\omega,k)E(k,w) = \frac{\omega_p^2\omega}{k v_T^\infty}\sum_m \frac{e^{im\omega t^0}}{(k v_T^\infty - \omega)^2 - \omega_B^2}E(k + mk_T^\infty, \omega + m\omega_T). \tag{E.6}$$

Note that it is not required that $k_T^\infty = k_\omega^{0r}$ as was in the original derivation.

The strongest coupling can be expected for those waves that approximately fulfill the TWT dispersion relation. This limits the interaction to the waves closest to the trapping wave, the lower and the upper sidebands with frequencies $\omega_T \pm \Delta\omega$ and wavenumbers $k_T^\infty \pm \Delta k$. Possible interaction with the wave of frequency $\Delta\omega$ is discarded in first approximation because $\epsilon(\Delta k, \Delta\omega) \not\approx 0$. The ensuing 2×2 matrix for $E(\omega,k)$ has nontrivial solutions if its determinant vanishes. This leads to the following dispersion relation:

$$\frac{\omega_p^2}{(k v_T^\infty - \omega)^2 - \omega_B^2}\Big[\frac{\omega/k v_T^\infty}{\epsilon(\omega,k)} + \frac{(\omega - 2\omega_T)/(k - 2k_T^\infty)v_T^\infty}{\epsilon(\omega - 2\omega_T^\infty, k - 2k_T^\infty)}\Big] = 1 \tag{E.7}$$

Typically the equation has more than one solution of k for given ω. Each solution determines a particular relationship between the complex amplitude of the upper and the lower sideband through (E.6). We call this combination of the two sidebands a "sideband normal mode". Keeping only the $m = 0$ and $m = -2$ terms of the sum on the right hand side in equation (E.6) we obtain:

$$\frac{E^*(2k_T^\infty - k, 2\omega_T - \omega)}{E(k,\omega)} = \Big[\frac{kv_T^\infty}{\omega_p}\frac{\epsilon^h(\omega,k)}{\omega_p^2}\Big((\omega - kv_T^\infty)^2 - \omega_B^2\Big) - 1\Big] \equiv -\alpha e^{i\theta} \qquad \text{(E.8)}$$

where α is positive and θ is related to the modulational phase.

When we apply the sideband dispersion relation (E.7) to the sidebands in the asymptotic steady state the bounce frequency ω_B must be replaced by ω_B^{dc} to account for the change of the potential well due to the applied dc electric field and the beam plasma frequency ω_p must be replaced by $\sqrt{\sigma}\omega_p$ to account for the fact that only the fraction σ of the beam electrons is trapped.

Appendix F

Nonlinear TWT Equations

As has been pointed out in chapter 1 it can be shown that the equations that describe the weak-cold-beam plasma instability are identical to those that describe the evolution of a cold beam on a TWT. Formally this equivalence is obtained by identifying the smallness parameter in the theory of O'Neil *et al.*, $(\eta/2)^{1/3}$, [47] with the Pierce gain parameter, C, of traveling wave tubes. Both parameters are a measure of the strength of the interaction of the beam with the waves on the support structure. But because the interaction of the beam with the wave on the traveling wave tube is given by a transmission line equation rather than Poisson's equation, above equivalence is true to lowest order in the smallness parameter only. Higher order correction terms are different.

The theory of the interaction of many waves with a cold beam has been given before [54, 62]. Here it is briefly reviewed. We solve the one-dimensional problem of the spatial evolution of three waves on a slow wave structure interacting with a mono-energetic beam of electrons. The next higher order term in C - in a manner given by Tien [60]-, damping of the waves on the support structure and space-charge effects are included. The problem is solved within the framework of the Lagrangian formalism wherein the beam is separated into N_e cylindrical charge blocks that enter the interaction region during the repetition time, T, of the waveform. Their initial

positions are marked by their initial phase, ϕ_0, relative to the phase of the waveform. We identify ω_1 with the angular frequency ω_T of the trapping wave and define the following scaled parameters:

$$y = C_1 \frac{\omega_1}{u_0} z \tag{F.1}$$

$$\phi_n(y,\phi_0) = \frac{\omega_n}{\omega_1}\frac{1}{C_1} y - \omega_n t \tag{F.2}$$

$$\frac{dz}{dt} = u_0(1 + C_1 q(y,\phi_0)) \tag{F.3}$$

$$b_n = \frac{1}{C_n}\left(\frac{k_n^{0r} u_0}{\omega_n} - 1\right) \tag{F.4}$$

$$d_n = \frac{1}{C_n}\frac{k_n^{0i} u_0}{\omega_n} \tag{F.5}$$

$$V(z,t) = 4V_0 C_1^2 \sum_{n=1}^{3} \Big\{ A_n \cos(\phi_n + \theta_n) \tag{F.6}$$
$$+ \frac{C_1}{2}\Big[\Big(\frac{C_n}{C_1}\Big) b_n + \frac{\omega_n}{\omega_1}\frac{d\theta_n}{dy}\Big) A_n \cos(\phi_n + \theta_n) - \frac{\omega_1}{\omega_n}\frac{dA_n}{dy}\sin(\phi_n + \theta_n)\Big]\Big\}$$

With these definitions the inhomogeneous wave equation, (2.9), the charge continuity equation, (2.15), Poisson's equation for the space-charge and Newton's equation, (2.6), can be written in a form suitable for solution on the computer.

$$\frac{\omega_1}{\omega_n}\frac{d\Theta_n}{dy} = -\frac{C_n}{C_1} b_n - \frac{1}{A_n}\Big(\frac{C_n}{C_1}\Big)^3 \int_0^{2\pi l} \frac{d\phi'_0}{2\pi l} \frac{\cos(\phi_n(y,\phi'_0) - \theta_n(y))}{1 + C_1 q(y,\phi'_0)} \tag{F.7}$$

$$\frac{\omega_1}{\omega_n}\frac{dA_n}{dy} = -\frac{C_n}{C_1} d_n A_n + \Big(\frac{C_n}{C_1}\Big)^3 \int_0^{2\pi l} \frac{d\phi'_0}{2\pi l} \frac{\sin(\phi_n(y,\phi'_0) - \theta_n(y))}{1 + C_1 q(y,\phi'_0)} \tag{F.8}$$

$$\frac{\omega_1}{\omega_n}\frac{\partial \phi_n}{\partial y} = \frac{q(y,\phi_0)}{1 + C_1 q(y,\phi_0)} \tag{F.9}$$

$$\Big(1 + C_1 q(y,\phi_0)\Big)\frac{\partial q}{\partial y} = \sum_{n=1}^{3}\Big\{-2A_n \frac{\omega_n}{\omega_1}\sin(\phi_n - \theta_n) \tag{F.10}$$
$$+ C_1\Big[\frac{dA}{dy}\cos(\phi_n - \theta_n) + \Big(\frac{d\theta_n}{dy} - \frac{\omega_n}{\omega_1}\frac{C_n}{C_1} b_n\Big) A_n \sin(\phi_n - \theta_n)\Big]\Big\}$$
$$- \frac{E_{sc}}{E_T} - \frac{E_{dc}}{E_T}$$

where we have included an externally applied dc electric field E_{dc}.

The space-charge term is given by

$$\frac{E_{sc}}{E_T} = 2QC_1[1+\frac{r_b\omega}{u_0\gamma}]\frac{N_e}{l}\sum_{j=1}^{N_e} f\Big(\frac{u_0\gamma}{r_b\omega}(1+C_1Q_j)(\phi_j-\Phi_0)\Big) \qquad \text{(F.11)}$$

where

$$f(x) = \begin{cases} e^{-x}(e^{\Delta x}-e^{-\Delta x})^2 sgn(x) & \text{for } \mid x \mid \geq 2\Delta x \\ [(e^x-e^{2\Delta x})(e^{-x}-e^{-2\Delta x})+e^{-x}(e^{\Delta x}-e^{-\Delta x})^2]sgn(x) & \text{for } \mid x \mid \leq 2\Delta x \end{cases}$$

$$\begin{aligned} \Delta x &= \frac{u_0\gamma}{r_b\omega_1}\frac{l}{N_e} \\ E_T &= 2V_0\frac{\omega_1}{u_0}C_1^2 \end{aligned} \qquad \text{(F.12)}$$

The frequencies of the three waves have to be commensurate for this theory to apply. T is the period of the waveform created by superposition of these three waves; it is l periods of the period T_T of the trapping wave long. We choose N_e such that initially there are at least 100 electrons per period of the trapping wave. γ is obtained from the experimental fit given by equation (2.28).

The equations are integrated numerically with a step size $\Delta y = 0.01$. The accuracy of the calculation is monitored by comparing the two sides of the following expression:

$$\begin{aligned} &\int_0^{2\pi l}\frac{d\Phi_0}{2\pi l}q + \sum_n \frac{C_1}{C_n}^3(1+C_nb_n)A_n^2 \\ &= \int_0^y dy\Big(-\sum_n\Big[2(1+C_nb_n) - C_1(\frac{\omega_1}{\omega_n}\frac{d\theta_n}{dy}+\frac{C_n}{C_1}b_n)\Big]\frac{\omega_n}{\omega_1}d_nA_n^2\Big(\frac{C_1}{C_n}\Big)^2 \\ &+ \int_0^{2\pi l}\frac{d\Phi_0}{2\pi l}\frac{1}{1+C_1q}\frac{E_{SC}+E_{dc}}{E_T}\Big) \end{aligned} \qquad \text{(F.13)}$$

This equation becomes the momentum conservation equation of Tsunoda and Malmberg [63] in the limit where the space-charge can be neglected, where there is no dc electric field, no damping and the Pierce gain parameters, C_i, are small. The discrepancy of the two sides is less than 10^{-5}, where the expressions themselves are of order 1.

Appendix G

Symbols

In this appendix we present a list of often occuring symbols and expressions. We either give their definition or the equation numbers of their definition, figure numbers where they are shown, typical or their exact values. SI units are used throughout the dissertation.

Electron Beam

I_b	$40 - 120\mu$A	electron beam current
r_b	3.2 mm	radius of the electron beam
v	$2.5 - 5.10^6$ m/s	velocity of an electron
u_0		velocity of the cold electron beam
V_c	$50 - 70$ V	cathode voltage
V_0	$V_0 = mu_0^2/2e$	electron beam voltage
V_{s1}	≈ 0 V	voltage on first spreader grid
V_{s2}	≈ 2 kV	voltage on second spreader grid
V_{s3}	≈ -40 V	voltage on third spreader grid
V_{dc}	$50 - 100$ V	externally applied dc voltage on helix
ρ(v,z)	$.25 - 1.10^{-6}$C/m^3	beam charge density
ρ_0	$.25 - 1.10^{-6}$C/m^3	beam charge density of cold beam
n_0	$.5 - 2.10^8$m^{-1}	axial beam density
$f(v,z,t)$		beam velocity distribution
$f_0(v,z)$		time-averaged beam velcoity distribution
$E^{sc}(z,t)$		space-charge electric field
H_q	figure 2.8	space-charge parameter
ω_p	$2\pi(5-20)$ MHz	beam plasma frequency
ω_q	$\sqrt{P_q}\omega_p$	reduced beam plasma frequency
P_q	(2.14)	plasma frequency reduction factor
σ	4.8	trapped particle ratio

Basic Constants

$-e$	$-1.6\,10^{-19}$ C	electron charge
m	$9.1\,10^{-31}$ kg	electron mass
ϵ_0	8.8510^{-12} As/Vm	dielectric constant

Helix

a	10.77 mm	radius of the helix
L	2.35 m	length of the interaction region
k_ω^0	$k_\omega^0 = k_\omega^{r0} - ik_\omega^{i0}$	complex wavenumber of wave on beamless helix
R_ω	fig. 2.4	real wave-beam interaction impedance
v_ω^{ph}	fig. 2.3	phase velocity on beamless helix
v_ω^{gr}	fig. 2.3	group velocity on beamless helix
$\epsilon^h(\omega, k_\omega^0)$	eqn. 2.10	beamless helix dielectric
A	dB	launch amplitude of the spectrum compared to saturation case

Frequencies

ω		angular frequency of waves on helix
f_{hom}	86 MHz	homodyne frequency
f_{clock}	120 MHz	clock frequency
N		total number of points of a waveform
T	N/f_{clock}	period of the waveform sent with the waveform generator
$\delta\omega$	$\delta\omega \equiv 1/T$	angular frequency separation between modes
ω_p	$2\pi(5-20)$ MHz	beam plasma frequency
ω_T		angular trapping wave frequency
$\delta\omega_{sb}$		angular sideband frequency separation
ω_l	$\omega_T - \delta\omega_{sb}$	angular frequency of lower sideband
ω_u	$\omega_T + \delta\omega_{sb}$	angular frequency of upper sideband
ω_d	$\Delta\omega_{sb}$	angular frequency of difference wave
ω_B	eqn. 4.2	angular bounce frequency
ω_B^{dc}	eqn. 4.12	angular bounce frequency modified for E_{dc}
ω_n	$f_{\text{hom}} - \frac{n}{N} f_{\text{clock}}$	angular mode frequency
$\Delta\omega_{tot}$	eqn.3.8	frequency width of the wave spectrum
$\Delta\omega_n$	2π 2.5MHz	frequency width of a physical mode

Wavenumbers

k_ω^0	$k_\omega^0 = k_\omega^{0r} - ik_\omega^{0i}$	complex wavenumber of wave on beamless helix
k_ω^{0r}	figure 2.3	real wavenumber of beamless helix
k_ω^{0i}	figure A.2	damping rate of beamless helix
k_T^∞	eqn. 4.9	asymptotic wavenumber of trapped particle state
k_l		wavenumber of lower sideband
k_u		wavenumber of upper sideband
k_n^r		real wavenumber of Fourier mode with frequency ω_n
k_n^i		growth rate of Fourier mode with frequency ω_n
δk_n		wavenumber shift due to interaction with beam

Phases

$\delta\phi_\omega(z)$		phase shift due to wave-beam interaction
$\Theta(z)$	eqn. 4.16	modulational phase

Electric Fields, Potentials

E_{ω_n}	eqn. B.6	electric field amplitude of Fourier mode ω_n
E_T^∞		electric field amplitude of trapping wave
E_l		electric field amplitude of lower sideband
E_u		electric field amplitude of upper sideband
E_{dc}		externally applied dc electric field
$E^h(z,t)$	eqn. 2.9	helix electric field
$E^{sc}(z,t)$	eqn. 2.12	space-charge electric field
V_ω^h	2.9	wave potential on helix

Symbols used for Weak Warm Beam Instability

D^{ql}	eqn.B.19	quasilinear diffusion coefficient
D^{rb}	eqn.B.34	resonance-broadening diffusion coefficient
l_{ac}	eqn.3.8	spectrum autocorrelation length
l_p	eqn.3.10	periodicity length
l_{tt}	eqn.3.9	turbulent trapping length
S_n	eqn.3.22	scatter component of electric field amplitude E_n
T_n	eqn.3.22	transmitted component of electric field amplitude E_n

References

[1] J.C. Adam, G. Laval, and D. Pesme. Reconsideration of quasilinear theory. *Physical Review Letters*, 43:1671, 1979.

[2] L.M. Al'tshul and V.I. Karpan. The kinetics of waves in a weakly turbulent plasma. *Soviet Physics JETP*, 20:1043, 1965.

[3] I. B. Bernstein, J. M. Greene, and M. D. Kruskal. Exact nonlinear plasma oscillations. *Physical Review*, 108:546, 1957.

[4] D. Biskamp and H. Welter. On the validity of the quasi-linear approximation for turbulent plasmas. *Nucl. Fusion*, 12:89, 1972.

[5] M. Bitter and P. J. Paris. Generation of monochromatic electrostatic waves of large amplitude in a bounded beam-plasma system. *Journal of Plasma Physics*, 14:389, 1975.

[6] G.M. Branch and T.G. Mihran. Plasma frequency reduction factors in electron beams. *IRE Transactions - Electron Devices*, ED-2:3, 1955.

[7] L. Brillouin. The traveling-wave tube (discussion of waves for large amplitudes). *Journal of Applied Physics*, 20:1196, 1949.

[8] A. L. Brinca. Sideband growth in nonlinear landau wave-particle interaction. *Journal of Plasma Physics*, 7:385, 1972.

[9] N. I. Bud'ko, V. I. Karpman, and D. R. Shklyar. Stability of a plasma in the field of a longitudinal monochromatic wave. *Sov. Phys. JETP*, 34:778, 1972.

[10] W. Carr, D. Boyd, H. Liu, G. Schmidt, and M.Seidl. High-order wave mixing in beam-plasma instabilities. *Physical Review Letters*, 28:662, 1972.

[11] J.R. Cary, I. Doxas, D.F. Escande, and A.D. Verga. Enhancement of the velocity diffusion in longitudinal plasma turbulence. *Physics of Fluids B*, 4:2062, 1992.

[12] J. Denavit and W. L. Kruer. Comparison of numerical solutions of the vlasov equation with particle simulations of collisionless plasmas. *Physics of Fluids*, 14:1782, 1971.

[13] P. DeNeef. Test wave coexisting with a large-amplitude electron plasma wave. *Physical Review Letters*, 31:446, 1973.

[14] P. DeNeef. Two waves on a beam-plasma system. *Physics of Fluids*, 18:1209, 1975.

[15] P. DeNeef, J. H. Malmberg, and T. M. O'Neil. Launched waves on a beam-plasma system. *Physical Review Letters*, 30:1032, 1973.

[16] G. Dimonte and J. H. Malmberg. Destruction of trapping oscillations. *Physics of Fluids*, 21:1188, 1978.

[17] W.E. Drummond. Spatially growing electrostatic turbulence. *Physics of Fluids*, 7:816, 1964.

[18] W.E. Drummond and D. Pines. Non-linear stability of plasma oscillations. *Nucl. Fusion, Suppl.*, Part 3:1049, 1962.

[19] C.T. Dum. Simulation studies of plasma waves in the electron foreshock: the generation of langmuir waves by a gentle bump-on-tail electron distribution. *J. Geophys. Res.*, 95:8095, 1990.

[20] T.H. Dupree. A perturbation theory for strong plasma turbulence. *Physics of Fluids*, 9:1773, 1966.

[21] T.H. Dupree. Theory of phase space density granulation in plasma. *Physics of Fluids*, 15:334, 1972.

[22] R. N. Franklin, S. M. Hamberger, H. Ikezi, G. Lampis, and G. J. Smith. Nature of the instability caused by electrons trapped by an electron plasma wave. *Physical Review Letters*, 28:114, 1972.

[23] A.A. Galeev, R.Z. Sagdeev, V.D. Shapiro, and V.I. Shevchenko. Is renormalization necessary in the quasilinear theory of langmuir oscillations. *Sov.Phys. JETP*, 52:1095, 1980.

[24] M. V. Goldman. Theory of stability of large periodic plasma waves. *Physics of Fluids*, 13:1281, 1970.

[25] M. V. Goldman and H. L. Berk. Stability of a trapped particle equilibrium. *Physics of Fluids*, 14:801, 1971.

[26] Y. Higuchi. Temporal subsideband growth due to secondary distortion of trapped particles. *J.Phys.Soc.Jap.Lett.*, 49:1645, 1980.

[27] H. Ikezi, Y. Kiwamoto, K. Nishikawa, and K. Mima. Trapped-ion instabilities in ion-acoustic wave. *Physics of Fluids*, 15:1605, 1971.

[28] G. Jahns and G. Van Hoven. Sideband instability: observations and comparison with theory. *Physical Review Letters*, 31:436, 1973.

[29] H.R. Johnson. Kompfner dip conditions. *Proceedings of the IRE*, 43:874, 1955.

[30] K. Jungwirth, V. Piffl, and J. Ullschmied. Effect of trapped beam electrons on nonlinear beam-plasma interaction. *Plasma Phys.*, 16:283, 1974.

[31] Y. C. Kim, , J. M. Beall, E. J. Powers, and R. W. Miksad. Bispectrum and nonlinear wave coupling. *Physics of Fluids*, 23:258, 1980.

[32] Y. C. Kim and E. J. Powers. Digital bispectral analysis and its applications to nonlinear wave interactions. *IEEE Transactions on Plasma Science*, PS-7:120, 1979.

[33] B. P. Koch and R. W. Leven. The sideband instability and wave-particle interaction. *Physica Scripta*, 27:220, 1982.

[34] R. Kompfner. On the operation of the traveling-wave tube at low level. *Jour. Brit. IRE*, 10:283, 1950.

[35] S.M. Krivoruchko, V.A. Bashko, and A.S. Bakai. Experimental investigations of correlation phenomena in the relaxation of velocity-spread beam in a plasma. *Physics of Fluids*, 23:258, 1980.

[36] W. L. Kruer and J. M. Dawson. Sideband instability. *Physics of Fluids*, 13:2747, 1970.

[37] W. L. Kruer, J. M. Dawson, and R. N. Sudan. Trapped-particle instability. *Physical Review Letters*, 23:838, 1969.

[38] G. Laval and D. Pesme. Breakdown of quasilinear theory for incoherent 1-d langmuir waves. *Physics of Fluids*, 26:52, 1983.

[39] Y.-M. Liang and P.H. Diamond. Weak turbulence theory of langmuir waves: a reconsideration of the validity of quasilinear theory. *Comments Plasma Phys. Controlled Fusion*, 15:139, 1993.

[40] J.H. Malmberg, T.H. Jensen, and T.M. O'Neil. Theory and measurement of the perturbation in the electron velocity distribution function caused by a landau damped wave. *Plasma Physics and Controlled Nuclear Fusion Research*, 1:683, 1966.

[41] Y. Matsuda and F. W. Crawford. Computational study of nonlinear plasma waves: Ii. sideband instability and satellite growth. *Physics of Fluids*, 18:1346, 1975.

[42] K. Mizuno and S. Tanaka. Experimental observation of nonlinear wave-particle interactions in a weak cold beam-plasma system. *Physical Review Letters*, 29:45, 1972.

[43] G. J. Morales. Effect of a dc electric field on the trapping dynamics of a cold electron beam. *Physics of Fluids*, 23:2472, 1980.

[44] L. Muschietti and C.T. Dum. Nonlinear wave scattering and electron beam relaxation. *Physics of Fluids B*, 3:1968, 1991.

[45] T.M. O'Neil. Probability distribution for fourier components of the electric field in weak plasma turbulence. *Physical Review Letters*, 33:73, 1974.

[46] T.M. O'Neil and J.H. Malmberg. Transition of the dispersion roots from the beam-type to the landau-type solutions. *Physics of Fluids*, 11:1754, 1968.

[47] T.M. O'Neil, J.H. Winfrey, and J.H. Malmberg. Nonlinear interaction of a small cold beam and a plasma. *Physics of Fluids*, 14:1204, 1971.

[48] J.R. Pierce. *Traveling-wave tubes.* D. Van Nostrand Company, Inc., 1950.

[49] Ch. P. Ritz, E. J. Powers, and R. D. Bengtson. Experimental measurement of three-wave coupling and energy cascading. *Physics of Fluids B*, 1:153, 1989.

[50] C. Roberson and K.W. Gentle. Experimental test of the quasilinear theory of the gentle bump instability. *Physics of Fluids*, 14:2462, 1971.

[51] P. Rolland. The importance of trapping in strong plasma turbulence. *Journal of Plasma Physics*, 15:57, 1974.

[52] R.Z. Sagdeev and A.A. Galeev. *Nonlinear plasma theory.* W.A. Benjamin, Inc., 1969.

[53] R.Z. Sagdeev, V.D. Shapiro, and V.I. Shevchenko. A note on the validity of quasilinear theory. subm. to Physics of Fluids B.

[54] M. K. Scherba. Characteristics of multisignal and noise-modulated high-power microwave amplifiers. *IEEE Transaction on Electron Devices*, ED-18:11, 1971.

[55] V. D. Shapiro and V. I. Shevchenko. Stability of a monochromatic wave in a plasma. *Sov. Phys. JETP*, 30:1121, 1970.

[56] D. Shiffler, J. D. Ivers, G. S. Kerslick, J. A. Nation, and L. Schachter. Sideband development in a high-power traveling tube amplifiers. *Applied Physics Letters*, 58:899, 1991.

[57] M. M. Shoucri. Computer simulation of the sideband instability. *Physics of Fluids*, 21:1359, 1978.

[58] T. P. Starke and J. H. Malmberg. Experiment on sideband dispersion. *Physics of Fluids*, 21:2242, 1978.

[59] K. Theilhaber, G. Laval, and D. Pesme. Numerical simulations of turbulent trapping in the weak beam-plasma instability. *Physics of Fluids*, 30:3129, 1987.

[60] P. K. Tien. A large signal theory of traveling wave amplifiers. *Bell. Sys. Tech. J.*, 35:349, 1956.

[61] A.W. Trivelpiece and R.W. Gould. Space charge waves in plasmas. *Journal of Applied Physics*, 30:1784, 1959.

[62] S. I. Tsunoda and J. H. Malmberg. Wave enhancement due to a static electric field. *Physics of Fluids*, 27:2557, 1984.

[63] S. I. Tsunoda and J. H. Malmberg. Trapped particle sideband studies. *Physics of Fluids B*, 1:1958, 1989.

[64] S.I. Tsunoda, F. Doveil, and J.H. Malmberg. Experimental test of the quasi-linear theory of the interaction between a weak warm electron beam and a spectrum of waves. *Physical Review Letters*, 58:1112, 1987.

[65] S.I. Tsunoda, F. Doveil, and J.H. Malmberg. Experimental test of the quasilinear theory. *Physics of Fluids B*, 3:2747, 1991.

[66] G. Van Hoven and G. Jahns. Behavior of the sideband instability. *Physics of Fluids*, 18:80, 1975.

[67] A.A. Vedenov, E.P. Velikhov, and R.Z. Sagdeev. *Nucl. Fusion, Suppl.*, Part 2:465, 1962.

[68] R. W. Warren, B. E. Newnam, and J. C. Goldstein. Raman spectra and the los alamos free-electron laser. *IEEE Journal of Quantum Electronics*, QE-21:882, 1985.

[69] C. B. Wharton, J. H. Malmberg, and T. M. O'Neil. Observations of sidebands. *Physics of Fluids*, 11:1761, 1968.